Integrated Goniometry: The Introduction & Implementation of a Novel Goniometry Technique Examining Evolving Mars CO_2 Ice Analogs

Kendall Koga

A Thesis Submitted to the Faculty of Graduate Studies In Partial Fulfillment of the Requirements for the Degree of Master of Science

Graduate Program in Earth & Space Science
York University
Toronto, Ontario

June 2026

© Kendall Koga, 2026

Abstract

A novel photogoniometry technique dubbed *integrated goniometry* is introduced to analyze evolving CO_2 ice grown using the MARs Volatile and Ice evolutioN (MARVIN) chamber at York University [1]. In order to simulate Martian surface samples under Mars polar conditions, CO_2 ices are grown in the chamber under analogous conditions. These samples, that are in an isolated environment and evolve over time, are difficult to examine using traditional goniometry techniques. Integrated goniometry aims to address these difficulties, by utilizing a camera to image a series of reflective surfaces following the curved geometry of a hemisphere that intercept the hemisphere of reflectance coming off an illuminated sample. Utilizing the high-speed data collection capabilities of integrated goniometry, we demonstrate the ability to collect data on time variable phenomena, successfully examining actively evolving Mars-analog CO_2 ice.

Acknowledgments

The author would like to thank Isaac Smith of York University for his valuable support and funding for the completion of this project. Additionally, the support of Will Grundy of Northern Arizona University provided intellectual contributions and funding for this project. The author also thanks the NASA/Arizona Space Grant program, Lowell Observatory, the Solar System Research Virtual Institute (SSERVI), and the ESPRESSO project at the Southwestern Research Institute (SwRI) for providing funding and valuable feedback for this project. Additional thanks are given to the Astrophysical Materials Laboratory at Northern Arizona University for providing a previous development space for this project.

Contents

Page

Abstract ii

Acknowledgments iii

Table of Contents iv

List of Tables vi

List of Figures vii

1 Introduction **1**

1.1 Multiangular Reflectance 1

1.1.1 The Bidirectional Reflectance 2

1.1.2 The Bidirectional Reflectance Distribution Function (BRDF) 4

1.1.3 The Lambertian Model & Reflectance Standards 4

1.1.4 Data Collection & Hapke's Reflectance Factor (REFF) 7

1.2 CO_2 Ice On The Martian Poles 9

1.2.1 Simulated Martian CO_2 Ice Inside the MARVIN Chamber 12

1.2.2 Goniometry on Simulated Martian Ices 14

1.3 Addressing the Limitations of Traditional Goniometry with Integrated Goniometry 17

1.4 Complementary Metal-Oxide Semiconductor (CMOS) Imaging Sensors 21

2 Integrated Goniometry **24**

2.1 Introduction to Integrated Goniometry 24

2.2 Concept 25

2.3 Hardware, Design, & Execution 27

2.4 Code . . . 38
2.5 Standard Deviation . . . 41
2.6 Validation . . . 48
2.6.1 Camera Linearity Testing . . . 48
2.6.2 Reflectance Standard Validation . . . 51
2.6.3 Specular Reflection Testing Using a Mirror . . . 60

3 Evolving CO_2 Ice Experiments Using The MARVIN Chamber 64

3.1 Methods . . . 65
3.2 Results . . . 67
3.2.1 Diffusely Scattering Frosty CO_2 Ice . . . 67
3.2.2 Specular Transparent CO_2 Slab Ice Evolving Into Diffusely Scattering Frosty CO_2 Ice 75
3.3 Discussion . . . 87

4 Conclusion 89

Bibliography 92

List of Tables

2.1 Laser Specifications 31
2.2 Lens Specifications 32
2.3 Camera Specifications 34

List of Figures

1.1 The Bidirectional Reflectance Coordinate System 2
1.2 Foreshortening of a Lambertian Surface 5
1.3 Relative Reflectance Factor of Spectralon 7
1.4 NASA/JPL-Caltech/MSSS Images of The Martian Polar Residual Caps 9
1.5 ESA/DLR/FU Berlin Images of The Martian Polar Residual Caps 10
1.6 The Martian South Polar Region 11
1.7 The MARVIN Chamber 13
1.8 The Isen & Smith Mechanical Goniometer 14
1.9 Isen & Smith 2024 Slab Ice Reflectance 15
1.10 Isen & Smith 2024 Frosty Ice Reflectance 16
1.11 The Integrated Goniometry Development Testing Platform 19
1.12 The Novel Integrated Goniometry System for the MARVIN Chamber 20
1.13 Diagram of a Complementary Metal-Oxide Semiconductor (CMOS) Active Pixel Sensor (APS) Array 21
1.14 Example of a Bayer Filter 22
1.15 Example of a Color Camera Quantum Efficiency (QE) Plot 23

2.1 Integrated Goniometry Secondary Reflector Imaging Concept Diagram 26
2.2 Integrated Goniometry System Layout Diagram 27
2.3 Picture of the Goniometer 29
2.4 Picture of the Goniometer Inside the MARVIN Chamber 30
2.5 Goniometer Laser Pass-Though Schematic 31
2.6 Thorlabs PL203 Laser Stability 33

2.7 REFF Frame Production Visualization . . . 35
2.8 SRS-99-020 vs SRSS-99-020 3D Sample Plot . . . 36
2.9 SRS-99-020 vs SRSS-99-020 Scattering Plane Sample Plot . . . 36
2.10 SRS-99-020 vs SRSS-99-020 Interpolated Half Hemisphere Sample Plot . . . 37
2.11 Sample Image from the Calibration Stream . . . 39
2.12 MARVIN Goniometer Power Control Box . . . 40
2.13 Visualized Camera Noise Using Amplified Background Frames . . . 42
2.14 3D Plot of the Mean During Standard Deviation Testing . . . 44
2.15 3D Plot of the Standard Deviation . . . 45
2.16 Scattering Plane Plot of the Standard Deviation Compared to the Mean . . . 46
2.17 Standard Deviations as Percent of the Mean 3D Plot . . . 47
2.18 Standard Deviations as Percent of the Mean in the Scattering plane . . . 48
2.19 Linearity Testing Setup . . . 49
2.20 5 Second Exposure Linearity Test . . . 50
2.21 10 0.5 Second Exposure Stacking Linearity Test . . . 51
2.22 Goniometer Viewing the SRS-99-020 Spectralon Sample for Gray Spectralon Tests . . . 52
2.23 5 Second Exposure Gray Spectralon Reflectance Results . . . 54
2.24 10 0.5 Second Exposure Frame Stacking Gray Spectralon Reflectance Results . . . 55
2.25 5 Second Exposure Gray Spectralon Raw ADU Count Results . . . 57
2.26 10 0.5 Second Exposure Frame Stacking Gray Spectralon Raw ADU Count Results . . . 58
2.27 Directional Hemispherical Reflectance of Gray Spectralon . . . 60
2.28 Goniometer Viewing a Mirror for Specular Reflection Tests . . . 61
2.29 Specular Reflection ADU Results . . . 62
2.30 Specular Reflection REFF Results . . . 63

3.1 D4 Die Used for Size Scale when Growing Ice . . . 66
3.2 Martian Analog Frosty Ice Grown in the MARVIN Chamber . . . 67
3.3 Plot of Chamber Conditions Throughout Full Frosty Ice Experiment . . . 68
3.4 Chamber Data of Frosty Ice . . . 69
3.5 Scattering plane of Frosty Ice . . . 71

3.6 Interpolated Plot of Frosty Ice at 142 K 73
3.7 Image of the F4 Frosty Ice Morphology 73
3.8 Interpolated Plot of Frosty Ice at 160 K 74
3.9 Image of the F6 Frosty Ice Morphology 75
3.10 Martian Analog Slab Ice Grown in the MARVIN Chamber 76
3.11 Plot of Chamber Conditions Throughout Full Slab to Frosty Ice Experiment 77
3.12 Chamber Data of Slab Ice Evolving Into Frosty Ice 78
3.13 Scattering Plane of Slab Ice Evolving Into Frosty Ice 81
3.14 Interpolated Plot of Slab Ice at 167.3 K and 99.9 mbar 82
3.15 Image of the S2 Slab Ice Morphology 83
3.16 Interpolated Plot of Slab Ice Evolving Into Frosty Ice at 134.9 K and 6.0 mbar 84
3.17 Image of the S3 Transitional Morphology 85
3.18 Interpolated Plot of Frosty Ice Evolved from Slab Ice at 121.6 K and 6.0 mbar 86
3.19 Image of the S5 Frosty Ice Grown on Slab Ice Morphology 87

Chapter 1

Introduction

1.1 Multiangular Reflectance

To interpret the multiangular scattering properties of planetary surface materials, the theoretical framework provided by reflectance modeling enables interpretation of directional radiance measurements of light scattered by surfaces. Commonly utilized in planetary science and remote sensing applications, instruments used to acquire reflectance data work by measuring the radiance emitted by an illuminated surface [2, 1, 3]. The intensity of the measured radiance is dependent on sample composition, in addition to the illumination and observation geometry [4]. Following radiance measurements, the data is used to create reflectance values enabling characterization of surface properties at various illumination and measurement geometries.

One of the most widely adopted radiative transfer models used to characterize the multiple scattering properties of particulate planetary surface materials is the Hapke model [4]. It relates microscopic scattering properties of sample component grains to the macroscopic bidirectional reflectance characteristics of a particulate media. Using multiangular reflectance data, Hapke's photometric model can derive the volume-average single-scattering albedo, the volume-average single scattering function, the porosity coefficient, and the multi-scattering properties due to the surface roughness and porosity through the Ambartsumian–Chandrasekhar H function [4, 5]. Using this model the *bidirectional reflectance distribution function* (BRDF) can be derived to model the multiangular scattering properties of isotropic planetary surface media [4].

1.1.1 The Bidirectional Reflectance

Hapke's *bidirectional reflectance* function $r(i,e,g)$ is dependent on the incidence angle measured from the zenith i, and the emission angle measured from the zenith e. As well as the angular separation between source and detector called the phase angle g, as outlined by equation 1.1.

$$\cos g = \cos i \cos e + \sin i \sin e \cos \psi \tag{1.1}$$

Where ψ is the azimuth angle between the incident light source and the detector in the plane of the sample. A visualization of the bidirectional reflectance coordinate system is shown in figure 1.1 [4].

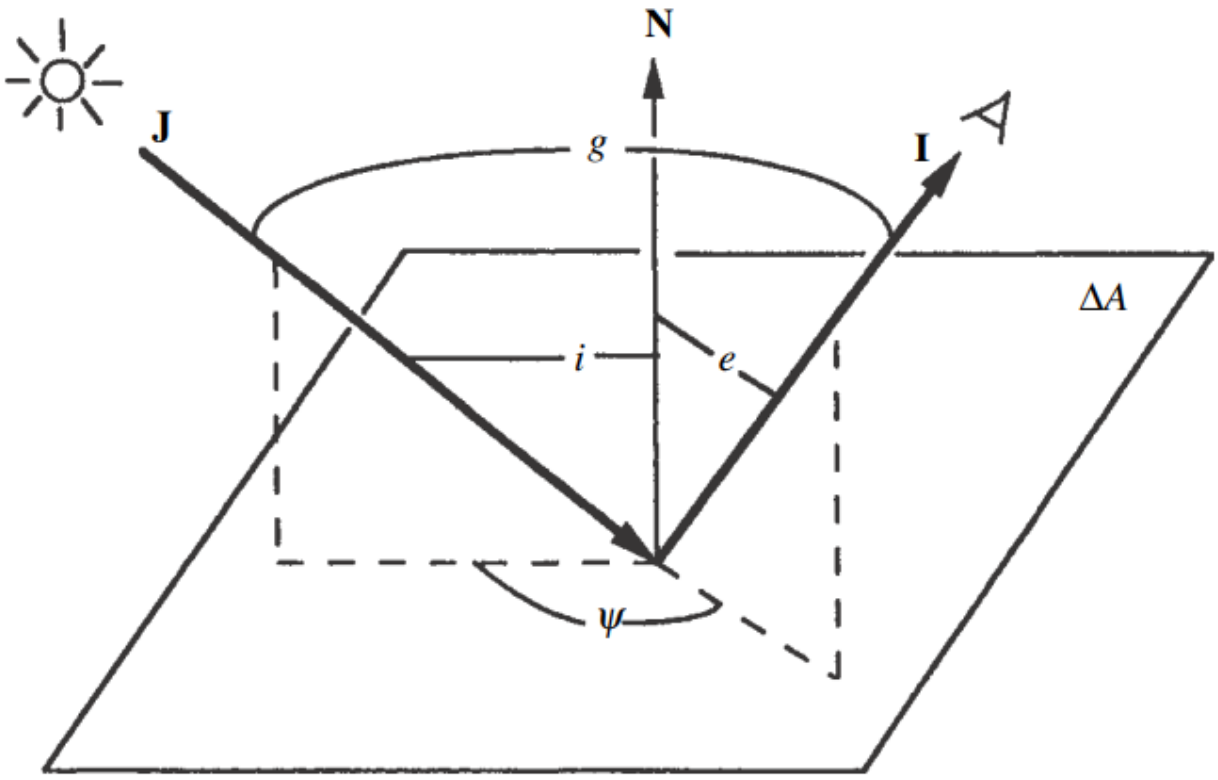

Figure 1.1: *Taken from figure 8.1 of "Theory of Reflectance and Emittance Spectroscopy." The incidence angle i measures the angle between the illumination source* **J** *and zenith of the sample normal* **N** *in the plane of the sample* ΔA*. The emission angle e measures the angle between the detector* **I** *viewing the sample and the zenith. The azimuth* ψ *measures the angular separation between the source and the detector in the plane of the sample. The phase angle g measures the angular separation directly between the source and detector. [4].*

The bidirectional reflectance $r(i,e,g)$ is defined by equation 8.70 in Hapke 2012 outlining the bidirectional reflectance of a semi-infinite isotropic medium [4].

$$r(i,e,g) = K\frac{\omega}{4\pi}\frac{\mu_0}{\mu_0+\mu}\{p(g)+H(\frac{\mu_0}{K})H(\frac{\mu}{K})-1\} \tag{1.2}$$

Where ω and $p(g)$ are the volume-average single scattering albedo, and the volume-average single scattering function, representing values commonly recovered from tuning this model that describe the scattering properties of single particles in a particulate medium. H is the Ambartsumian-Chandrasekhar H function,

$$H(\frac{x}{K}) = \frac{1+2x/K}{1+2\gamma x/K} \tag{1.3}$$

where γ is the albedo factor.

$$\gamma = \sqrt{1-\omega} \tag{1.4}$$

μ is the cosine of the emission angle,

$$\mu = cos(e) \tag{1.5}$$

and μ_0 is the cosine of the incidence angle.

$$\mu_0 = cos(i) \tag{1.6}$$

K is the porosity coefficient,

$$K = \frac{-ln(1-1.209\phi^{2/3})}{1.209\phi^{2/3}} \tag{1.7}$$

where ϕ is the filling factor that describes the volume of the examined material,

$$\phi = \frac{N4\pi a^3}{3} \tag{1.8}$$

N is the number of particles per unit volume, and a is the mean particle radius [4].

The value of r(i, e, g) can be measured directly according to equation 14.1 from section 14.2 of Hapke 2012[4].

$$r(sample) = \frac{I(sample)}{I(standard)}r(standard) \tag{1.9}$$

Where $I(standard)$ is the intensity of the incident beam as scattered off a sample with known scattering properties, measured at i, e, and g close to 0° while outside the opposition surge. With $r(i,e,g)$ measured, the normalized parameter can be inserted into Hapke's bidirectional reflectance distribution function (BRDF)

[4], discussed in section 1.1.2.

1.1.2 The Bidirectional Reflectance Distribution Function (BRDF)

The most fundamental and commonly used radiometric description of surface scattering is the *bidirectional reflectance distribution function* (BRDF). BRDF is defined as the ratio of directionally scattered radiance from the surface of a medium to the collimated power incident on a unit surface area of that medium, and can be calculated directly using the bidirectional reflectance [4].

$$BRDF(i,e,g) = \frac{r(i,e,g)}{\mu_0} \tag{1.10}$$

The BRDF accounts for the foreshortening of incident light on the surface, normalizing the reflected radiance by the cosine of the emission angle μ_0.

BRDF allows for complete characterization of angular scattering properties under collimated illumination conditions, analogous to the nature of incident solar radiation on planetary bodies [6]. Measurements taken in laboratory and remote sensing environments are frequently reported as BRDF, however most instruments do not directly measure BRDF [2, 7, 8, 9, 10, 11]. Highlighting the importance of the relation outlined by equation 1.10 where measurement of $r(i,e,g)$ can be directly related to the BRDF.

1.1.3 The Lambertian Model & Reflectance Standards

As outlined by equation 1.9, directly measuring the bidirectional reflectance requires measuring the intensity of light scattered off a sample with known scattering properties. To most accurately obtain this measurement, a sample of isotropic surface scattering properties, known as a Lambertian scatterer, is required [4].

Assuming a perfect Lambertian surface, incident radiance is scattered uniformly in all directions, resulting in isotropic photon scattering. However, when the illuminated surface is viewed with a detector, the observable intensity of the surface is foreshortened and the measured intensity is not isotropic, as shown in figure 1.2, resulting in the intensity being proportional to the cosine of the incidence angle i.

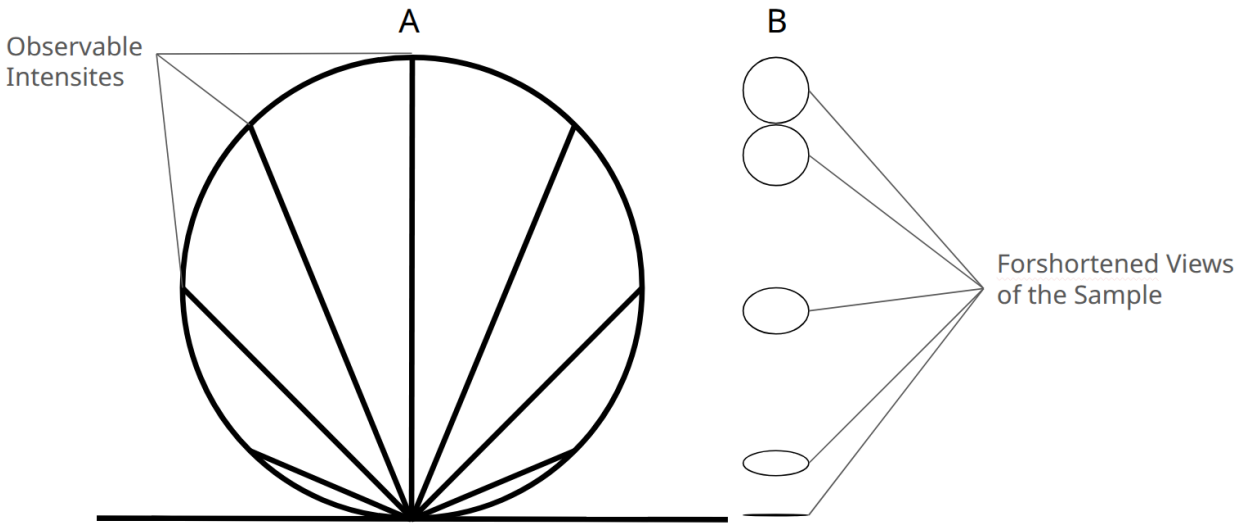

Figure 1.2: *A) the radiation intensity distribution of a foreshortened Lambertian surface. The decrease in intensity emitted as the emission angle increases is due to the foreshortening of the observed circular area of the sample B), effectively 'warping' the observable view [12].*

The equation of the intensity of a Lambertian surface is shown in equation 1.11 [12].

$$I = I_0 \rho cos(i) \tag{1.11}$$

Where I is the measured intensity, I_0 is the incident intensity, and ρ is the albedo. If we assume I is normalized to a Lambertian surface, which is often the case when pursuing bidirectional reflectance values, the value of *rho* can be assumed to be equal to 1, giving equation 1.11 the form.

$$I = I_0 cos(i) \tag{1.12}$$

The Lambertian intensity can be redefined as a function of the emission angle following the reciprocity principle originally formulated by Hermann von Helmholtz [4, 13, 14]. When applied to the bidirectional reflectance, the *principle of reciprocity* states that when a uniform medium illuminated by a collimated source making an incidence angle i with the surface normal is observed with a detector viewing a small section of the illuminated surface at an emission angle e from the surface normal. The observed bidirectional reflectance $r(i,e,g)$ will be equivalent with the bidirectional reflectance observed if the illumination source and detector positions were interchanged, denoted by the equivalent value $r(e,i,g)$. The relation states that

these reflectances must satisfy the reciprocity equation as follows [4, 13].

$$\frac{r(i,e,g)}{cos(i)} = \frac{r(e,i,g)}{cos(e)} \tag{1.13}$$

We can apply equation 1.13 to equation 1.9 if we first assume that the values of $I(sample)$ and $I(standard)$ are equivalent, leaving the value of $r(i,e,g)$ equal to the reflectance of the Lambertian surface $r(standard)$. With this assumption, we can determine that $r(i,e,g)$ and $r(e,i,g)$ are directly proportional to the intensity I of the Lambertian surface.

$$r(i,e,g) = r(e,i,g) \propto I \tag{1.14}$$

Meaning that we can assume $r(i,e,g)$ and $r(e,i,g)$ are equal to the respective forms of I shown in equations 1.15 and 1.16.

$$r(i,e,g) = I = I_0 cos(i) \tag{1.15}$$

$$r(e,i,g) = I = I_0 cos(e) \tag{1.16}$$

Using this proportionality, we can plug the intensity I of the Lambertian surface into the reciprocity relation as follows,

$$\frac{I = I_0 cos(i)}{cos(i)} = \frac{I = I_0 cos(e)}{cos(e)} \tag{1.17}$$

simplifying to get.

$$\frac{I_0 cos(i)}{cos(i)} = \frac{I}{cos(e)} \tag{1.18}$$

Simplifying, we obtain the final expression for the intensity I of radiation emitted by an illuminated Lambertian scatterer as a function of the emission angle e by applying the reciprocity principle.

$$I = I_0 cos(e) \tag{1.19}$$

In the real world, there are no known perfect Lambertian scatterers. This must be considered when experimental bidirectional reflectance observations are made. However, close approximations of Lambertian surfaces, or near-Lambertian surfaces, have been developed for use in calibration of experiments that collect bidirectional reflectance data. The most common near-Lambertian material used for reference measurements and calibration of goniometry systems is called Spectralon™ [7, 8, 9, 10, 4]. This material is composed of

powdered polytetrafluoroethylene (PTFE) that has been heated and compressed using a process that conforms the powdered PTFE into a hardened thermoplastic resin [7, 4]. Spectralon™ closely obeys the behavior of Lambertian scatterers, particularly at illumination angles close to the zenith, and has been manufactured to scatter light at a variety of intensities [15]. Deviations from true Lambertian behavior are observable as the emission angle increases, where the reflectance factor deviates from the foreshortening corrected theoretical value of 1 for all emission angles [7, 8, 9, 10]. The reflectance factor versus viewing angle are shown in figure 1.3 for several incidence angles as reported by Shaw in his 2016 publication [9].

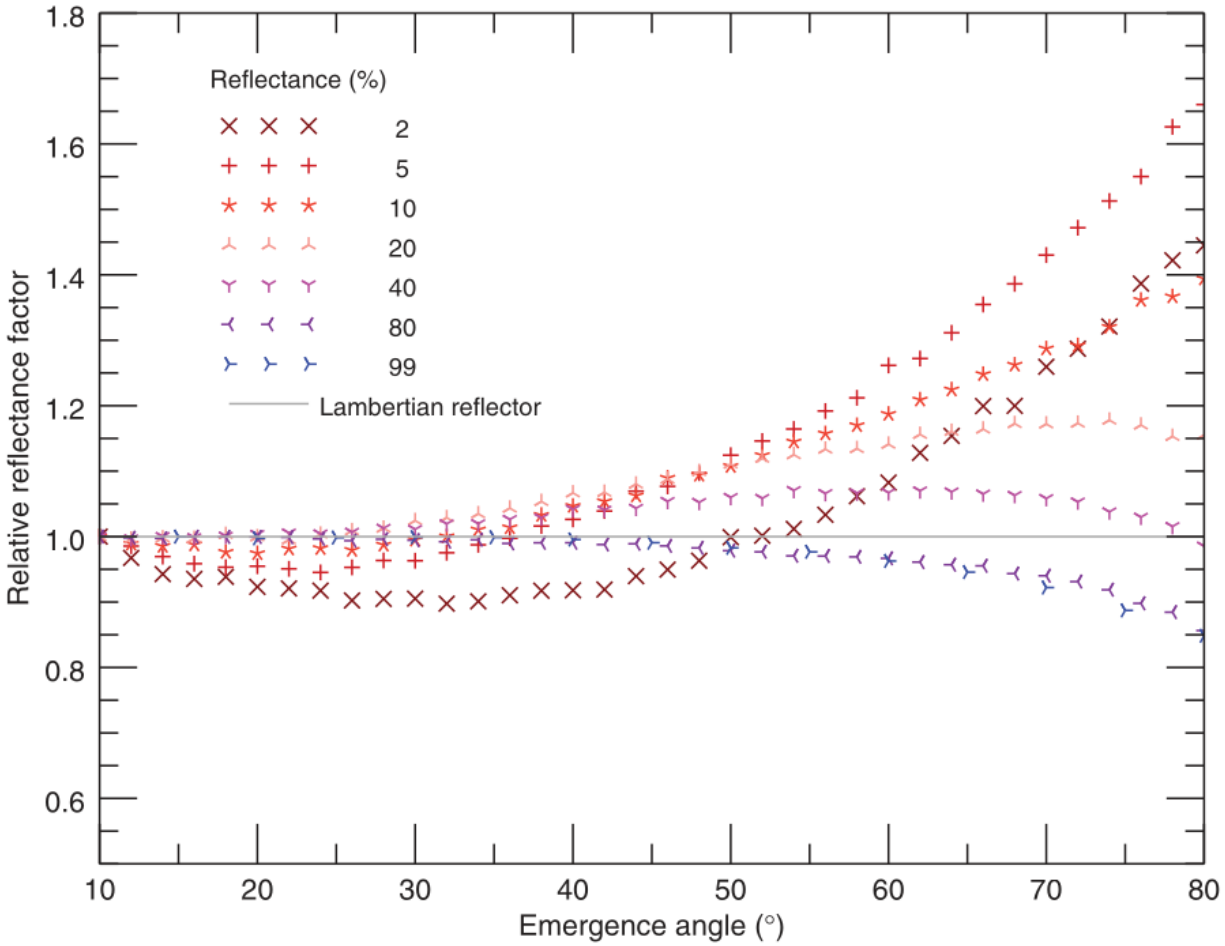

Figure 1.3: *Taken from figure 7 of A. Shaw's 2016 publication "Reflectance properties of grey-scale Spectralon® as a function of viewing angle, wavelength, and polarization." Spectralon reflectance factor measured at 1064 nm measured from a zenith angle of incidence of i = 0°, compared to that of a perfect Lambertian plotted as the gray line [8]*

1.1.4 Data Collection & Hapke's Reflectance Factor (REFF)

When directly measuring the bidirectional reflectance, the intensity of the source can be calibrated by positioning the detector to measure the intensity $I(standard)$ at i, e, and g close to 0° while outside the oppo-

sition surge. This produces a calibrated value normalized to the amount of radiation reflected by the standard sample to satisfy equation 1.9, directly producing the bidirectional reflectance [4]. With this value collected, the sample of interest can be placed within view of the source and the detector, and measurements can be made by dividing the measured reflectance of the sample of interest by the calibrated intensity collected using the Spectralon™ sample.

However, there is another commonly used method for collecting reflectance data, and one that will be the primary data collection method used in this thesis, called Hapke's *reflectance factor* (REFF). Defined as the ratio of the reflectance of a surface to that of a perfectly diffuse Lambertian surface under identical illumination conditions [4, 16, 17]. The REFF is defined by equation 10.3,

$$REFF(i,e,g) = \frac{\pi r(i,e,g)}{\mu_0} \tag{1.20}$$

and equation 8.70 in Hapke 2012 [4].

$$REFF(i,e,g) = K\frac{w}{4}\frac{1}{\mu_0+\mu}\{p(g)+H(\frac{\mu_0}{K})H(\frac{\mu}{K})-1\} \tag{1.21}$$

Combining equations 1.20 and 1.10, we can relate the REFF to the BRDF though a factor of π.

$$BRDF(i,e,g) = \frac{REFF(i,e,g)}{\pi} \tag{1.22}$$

Unlike bidirectional reflectance, REFF is dependent on the directional geometry of the measurements performed, providing a convenient experimental procedure in which the positions of the illumination source and detector can remain the same. REFF can be measured by dividing a measurement of a sample of interest by a measurement of a calibrated standard under the same illumination and observation geometries [4, 16, 17], allowing REFF measurements to be taken by simply interchanging samples of interest. The work presented throughout this thesis is based on this idea, in which the system is designed to operate by interchanging samples within view of the illumination source(s) and the observation system without the need to adjust the geometric properties of the goniometer.

1.2 CO_2 Ice On The Martian Poles

The Martian poles are home to seasonal and year-round H_2O and CO_2 ice deposits, maintaining persistent residual caps of ice shown in figure 1.4. The north polar residual cap is made up of layered H_2O ice, while in the south, the visible CO_2 rich residual cap sits atop the larger southern polar layer deposit made up of H_2O ice and covered with Martian dust [18, 19, 20, 21]. During the Martian winter months, CO_2 from the atmosphere deposits onto the residual caps covering them in sheets of CO_2 ice [19, 22, 2, 1, 18, 23, 24].

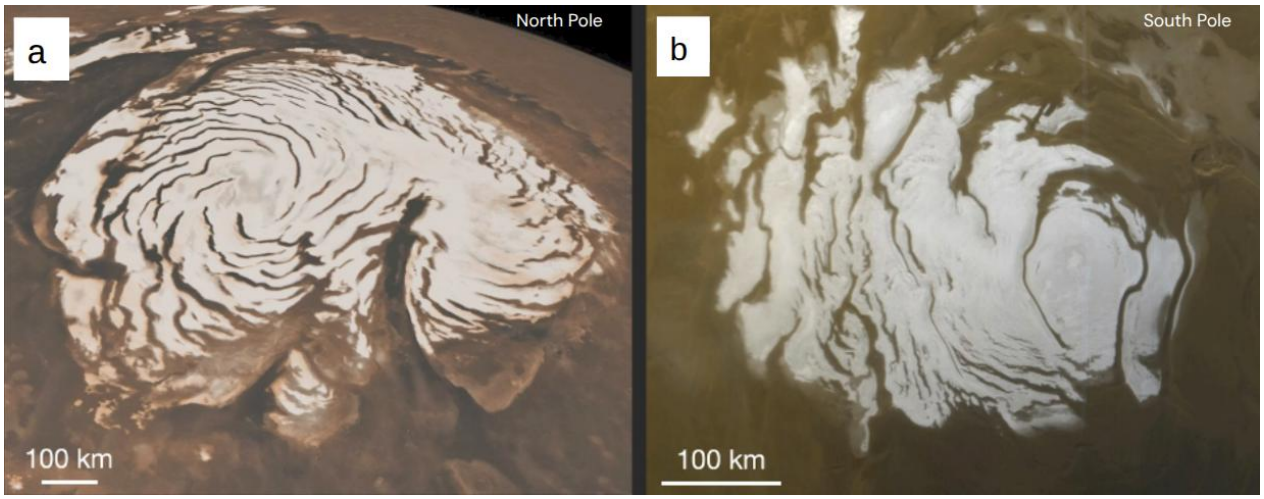

Figure 1.4: *The H_2O northern polar cap (a), and the CO_2 ice rich south polar residual cap (b) [19, 25, 26, 27, 21]. Photos were captured by the NASA Mars Global Surveyor. photo credit: NASA /JPL-Caltech/MSSS*

A defining characteristic of the Martian cryosphere is the abundance of seasonal carbon dioxide (CO_2) ice. The CO_2 dominated atmosphere of Mars coupled with seasonal temperature fluctuations cause atmospheric gas to deposit directly onto the surface as ice, resulting in cycles of seasonal polar CO_2 ice deposition in both hemispheres, forming the large CO_2 ice caps shown in figure 1.5 [19, 22, 2, 1, 18, 23, 24]. These seasonal temperature fluctuations drive the observed variations in polar ice, as illustrated by the comparison of Figures 1.5 and 1.4. Ice deposited during the winter subsequently sublimates, altering the distribution of CO_2 between the polar caps and the atmosphere, leading to atmospheric pressures ranging from approximately 1 to 14 mbar, depending on location and elevation. The Martian poles experience different amounts of seasonal CO_2 ice during their respective winters, with northern ice deposition causing a $\sim$14% drop in pressure from the global mean surface pressure of 5.6 mbar, with deposition on the southern pole causing a $\sim$22% drop [28, 29, 30, 31].

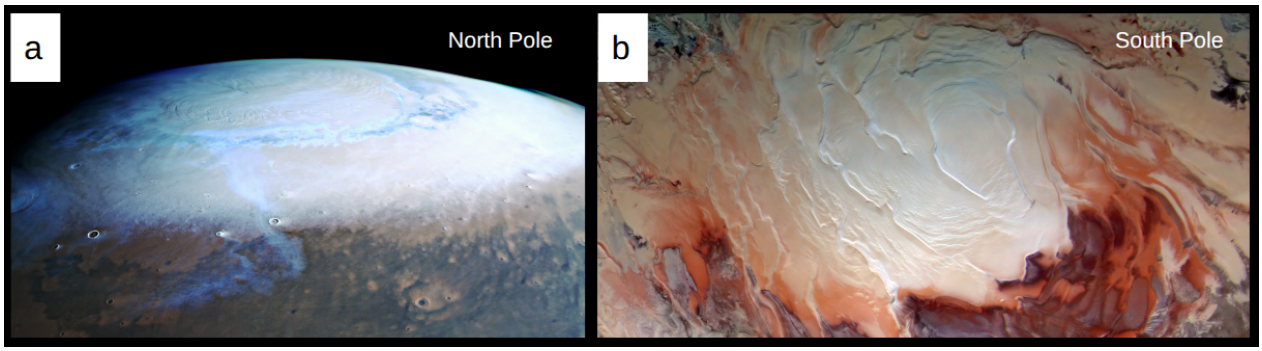

Figure 1.5: *The Martian polar seasonal caps composed of CO_2 ice; (a) is the northern cap, and (b) is the southern cap [21, 30]. Photos were captured by the High Resolution Stereo Camera (HRSC) from Mars EXpress (MEX). photo credit: ESA/DLR/FU Berlin, CC BY-SA 3.0 IGO*

The variable characteristics of Martian polar seasonal ice, mapped in figure 1.6 [32, 33, 2], create a dynamic system of atmospheric, cryospheric, and reflective surface properties. Observations from remote sensing instruments and laboratory simulations indicate that the seasonal CO_2 ice on Mars occurs in several distinct physical forms [23, 24, 2]. Including rough, porous, diffusely scattering or 'frosty' ice morphologies, believed to be found in the low temperature regions of interest seen in figure 1.6, regions 2 and 3. In addition to dense, sintered, smooth 'slab' ice morphologies, believed to be found in warmer, windier regions of interest analogous to the 'cryptic' region in figure 1.6, region 0 [2]. These seasonal ices are indicative of local surface and atmospheric conditions that are often influenced by seasonal cycles, based on their observed optical, mechanical, and thermodynamic properties [2, 34, 35, 25, 19, 36].

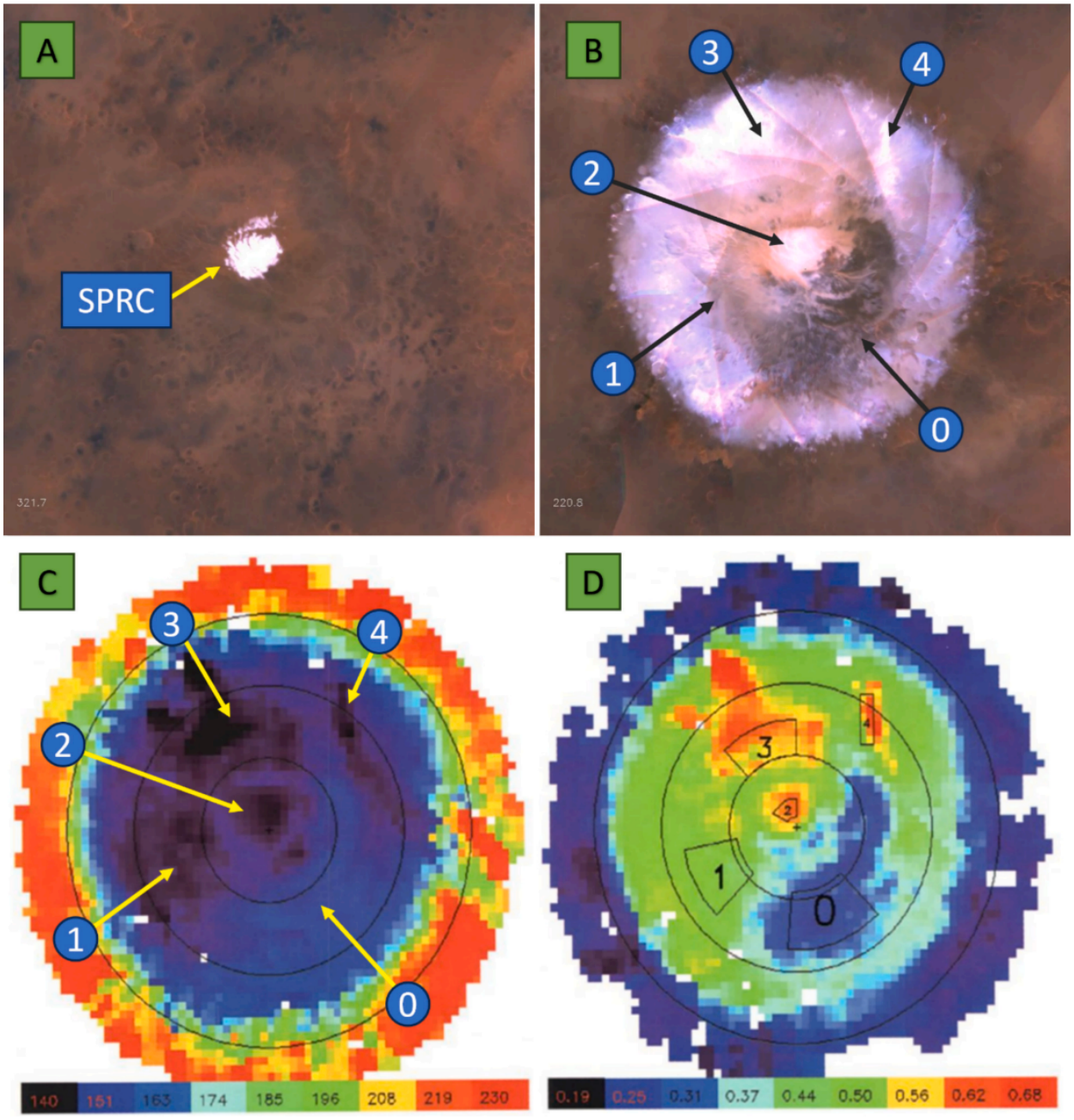

Figure 1.6: *Figure taken from figure 1 of the Isen and Smith 2024 publication "principle-plane BRDF of CO2 ice morphologies in controlled Mars polar conditions." 90° observation of the south polar region of Mars. A) Mars Color Image (MARCI) [33] mosaic viewing the fully defrosted south polar region and the remaining residual cap at solar longitude (Ls) 321°. B) MARCI image mosaic viewing seasonal CO_2 ice at Ls 217°. C) and D) Thermal Emission Spectrometer (TES) Observations of the Mars south seasonal CO_2 ice cap in the spring during Ls 217° to 220° [32]. C) is temperature in Kelvin, and D) is albedo. 0) is a region of interest (ROI) known as the 'cryptic' region, where low albedo CO_2 ice is observed in a locality of warmer temperatures. 1) provides a baseline of albedo and temperature. 2) the perennial frost cap exhibiting high albedo and low temperatures. 3) high albedo, low temperature region of seasonal CO_2 ice. 4) the Mountains of Mitchel observed to have cool temperatures and high albedo [32].*

1.2.1 Simulated Martian CO_2 Ice Inside the MARVIN Chamber

Simulations of Mars polar analog ices are actively performed using the MARs Volatile and Ice evolutioN chamber at York University [37, 1, 2, 22]. The chamber (figure 1.7) features a 48 $\times$ 35 $\times$ 77 cm experimental volume, a 10 $\times$ 15 cm LN_2 cold plate, multiple internal and external sample viewing cameras, a digital microscope, reflectance probe, a mechanical principle plane goniometer, and the novel rapid *integrated goniometry* system outlined later in this thesis. All experimental hardware within the volume is enclosed by an LN_2 cooled shroud painted with a high emissivity blackbody paint; when cooled the shroud minimizes thermal radiation inside the chamber [22, 1, 2]. The cold shroud allows for approximate simulations of the actual radiative environment on Mars. To approximate this environment, Planck's law can be used to approximate the spectral intensity of blackbody radiation emitted by the shroud.

$$E_\lambda(\lambda, T) = \frac{2hc^2}{\lambda^5[e^{hc/\lambda kT} - 1]} \tag{1.23}$$

Where T is the temperature, λ is wavelength, c is the speed of light, k is the Boltzmann constant, and h is the plank constant. Additionally, the Stefan-Boltzmann law can be used to describe the total blackbody emissive power radiated by the shroud, where σ is the Stefan-Boltzmann constant [38, 39].

$$E_b = \sigma T^4 \tag{1.24}$$

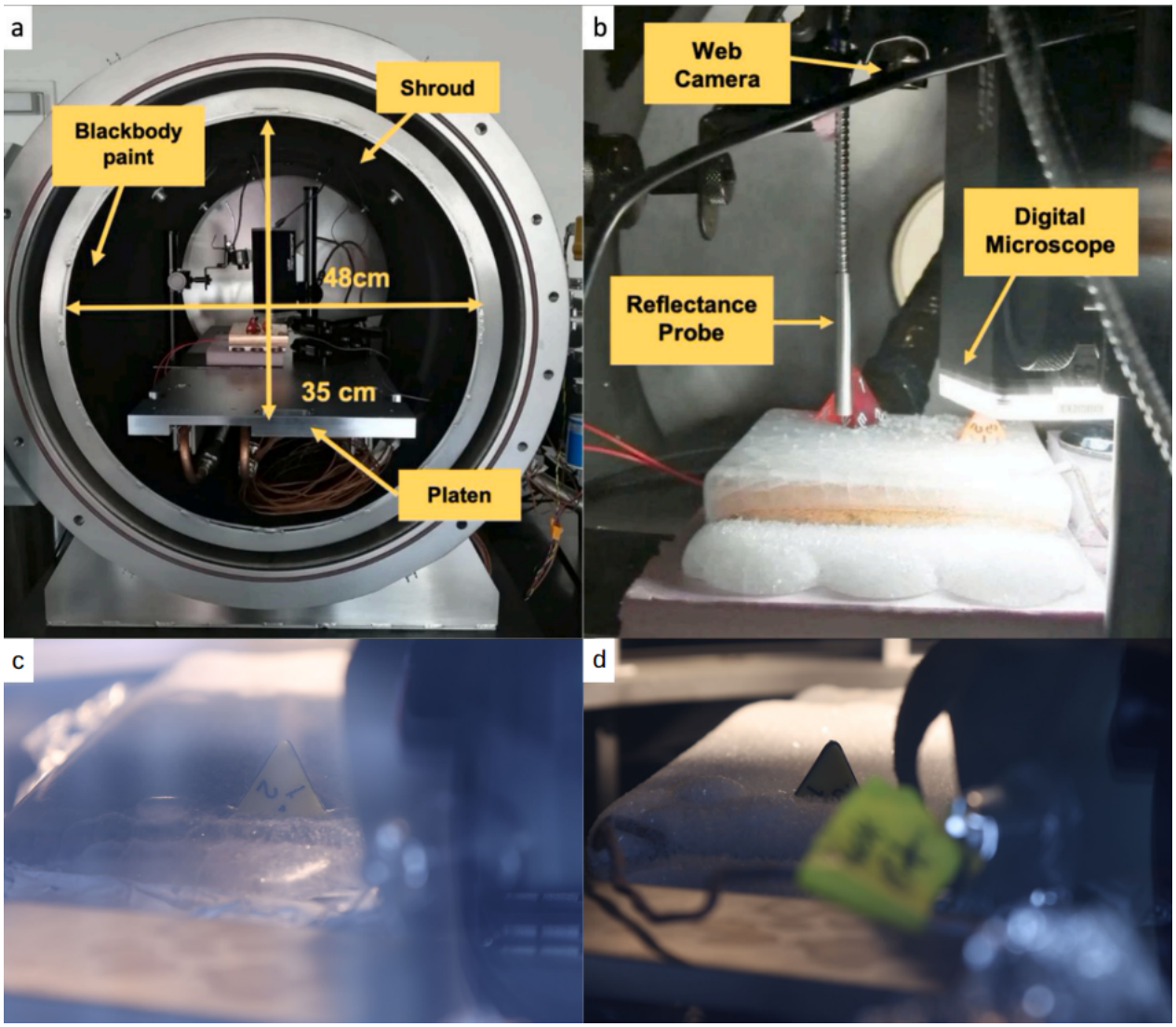

Figure 1.7: *Panels a) and b) are taken from figure 1 of Rushana Karimova's 2025 publication "Deposition of CO2 ice under Martin polar conditions: Textures, NIR reflectance and response to thermal stresses." The MARVIN chamber; a) views the front of the chamber with the door open, and b) is an up close view of the LN_2 cold plate with the internal webcam, reflectance spectrometer probe, and the digital microscope [22]. Panel c) is a sample of translucent 'slab' ice grown in the chamber, and d) is a sample of opaque, crystalline, 'frosty' ice.*

Experiments using the MARVIN chamber have produced both the slab (figure 1.7c) and frosty (figure 1.7d) ice morphologies commonly observed on Mars. Subtle differences in the surface structures of these morphologies have been produced using combinations of seasonal Mars-analog pressure and temperature variations, as well as with the use of the cooled shroud. These morphologies have been examined using the mechanical goniometer outlined in the Isen & Smith 2024 publication, where experimental results revealed that the slab ices were generally shiny and produced predominantly specular reflections, and the frosty ices generally exhibited diffuse scattering behavior with small but strong 'speckles' of scattered light in random

directions [2]. However, a weakness was discovered using the mechanical goniometer. The arms of the goniometer have to move to collect each data point, meaning that in the 12 minutes the device takes to capture a full principle plane of data, the reflective properties of the ice had evolved [2]. More detailed descriptions of the reflective properties of these ices will be discussed in section 1.2.2. These systematic weaknesses are common in traditional goniometers and are discussed in section 1.3.

1.2.2 Goniometry on Simulated Martian Ices

Performing goniometry on Mars analog ices in laboratory environments is a challenging problem covered by limited literature. This is due to the nature of traditional goniometry requiring a mobile illumination source and detector. This challenge is addressed in the Isen & Smith 2024 publication "principle-plane BRDF of CO2 ice morphologies in controlled Mars polar conditions," where a mechanical principle plane goniometer, shown in figure 1.8, was installed inside of the MARVIN chamber [1, 2].

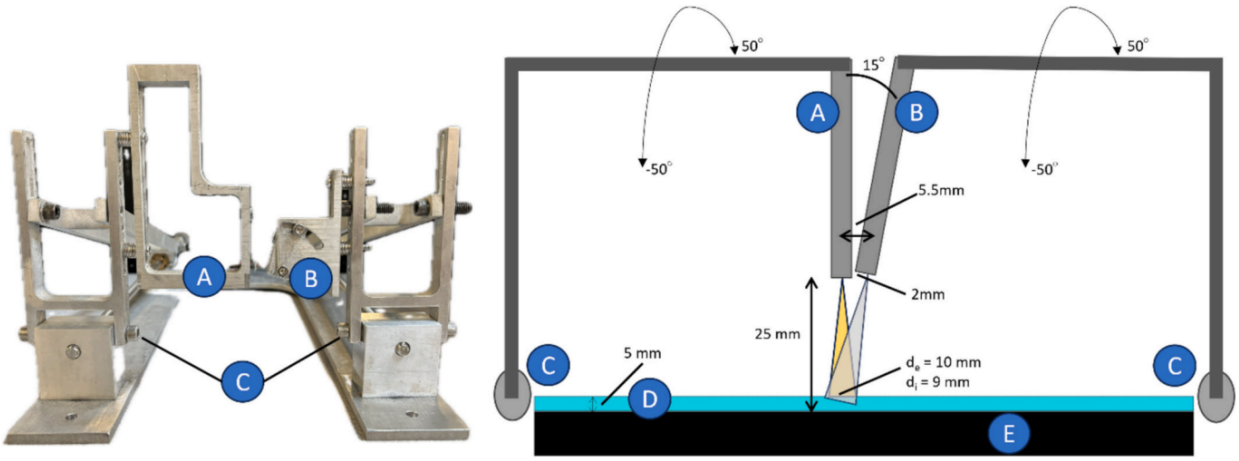

Figure 1.8: *Taken from figure 5 of the Isen & Smith 2024 publication "principle-plane BRDF of CO2 ice morphologies in controlled Mars polar conditions." The mechanical principle plane goniometer built for use inside the MARVIN chamber. A) is the light source positioned 25 mm above the cold plate E), while B) is the probe placed 2 mm above the light source and offset by 15° from the principle plane. C) is the center of rotation of the moving goniometer arms (into and out of page) allowing for ±50° of arm movement, and D) is the thickness of the sample grown on the cold plate [2].*

Experiments on Mars analog ice were run using this system inside the MARVIN chamber. In an experiment on smooth translucent slab ice, the sample was maintained under temperature and pressure conditions of 147-153 K on the cold plate and 194-202 K on the shroud, while the pressure was held around 6 mbar. The reflectance data from the translucent slab ice shown in figure 1.9 exhibited strong specular reflections throughout the course of the approximately 30 minute data collection process [2].

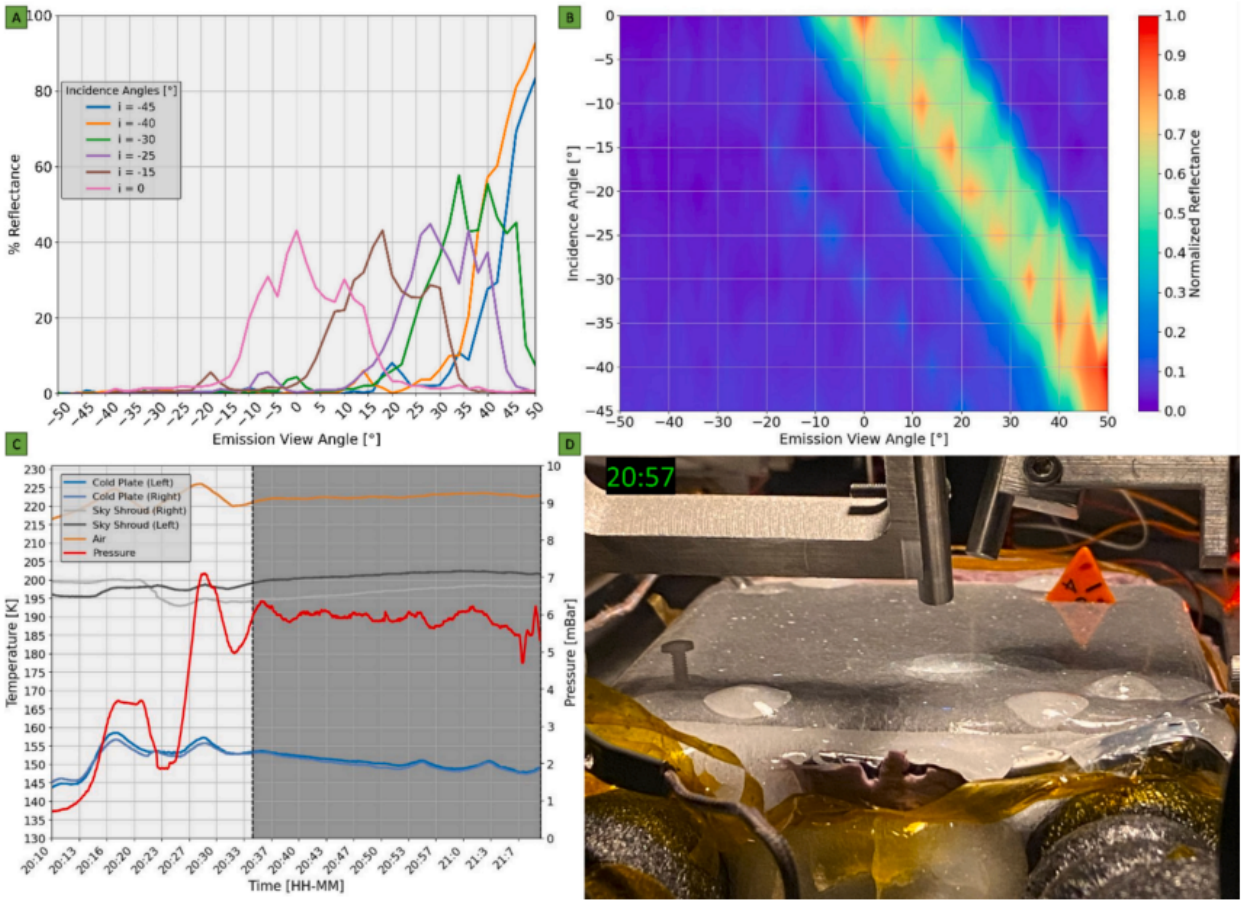

Figure 1.9: *Taken from figure 10 of the Isen & Smith 2024 publication "principle-plane BRDF of CO2 ice morphologies in controlled Mars polar conditions." A) plots the principal plane as emission angle vs percent reflectance depicting specular reflections of increasing strengths as a function of the increasing incidence angle. B) is an interpolated heat map plot of the emission angle vs the incidence angle, reinforcing stronger specular reflections with increasing incidence angle. C) plots the experimental conditions inside the MARVIN chamber as a function of time. The gray shaded area is the time when the goniometer was collecting data, during this time, the environmental conditions maintained cold plate temperatures in the range of 147-153 K, shroud temperatures in the range of 194-202 K, and a pressure of approximately 6 mbar. D) is a direct visual observation of the ice as seen through a window in the front door of the chamber with the orange d4 die acting as a size reference for the thickness of the ice, with the top of the bottom number on the die being equivalent to approximately 0.5 cm from the surface of the cold plate [2].*

In the frosty ice experiment shown in figure 1.10, the cold plate temperature was maintained within a range of 128-135 K with a shroud temperature range of 194-204 K, while maintaining a pressure of 3 mbar. The ice formed a frosty porous surface texture with semi-translucent crystals growing out of the surface of the ice. The results of the reflectance measurements suggest that the frosty ice predominantly exhibits diffuse scattering behavior, with a subtle coupled preference for forward and back scattering at incidence angles greater than 15°. Additionally, some mild forward scattering peaks are observed at incidence angles below 20° [2].

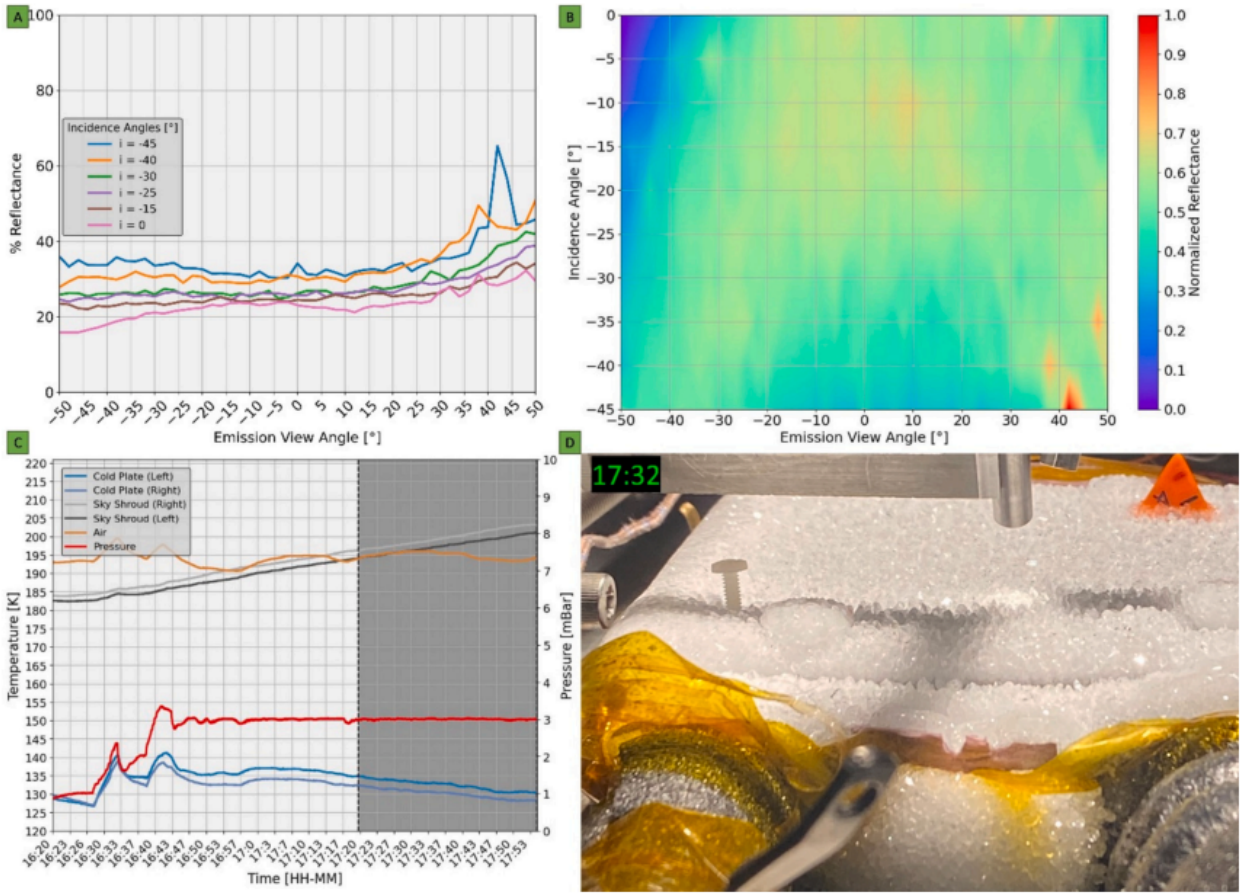

Figure 1.10: *Taken from figure 13 of the Isen & Smith 2024 publication "principle-plane BRDF of CO2 ice morphologies in controlled Mars polar conditions." A) depicts much more diffuse scattering behavior than the slab ice experiments, with slight increases in the percent reflectance at increasing emission angles when the angle of incidence is above 15°, with the heatmap in B) clearly visualizing this scattering behavior. The experimental conditions in C) during the shaded data collection time show stable conditions while the goniometer is collecting data, maintaining cold plate temperatures in the range of 128-135 K, shroud temperatures in the range of 194-204 K, and a stable pressure of 3 mbar. The rough, opaque, crystalline surface of the diffusely scattering ice can be seen in D) at a thickness of approximately 0.5 cm as indicated by the height of the ice relative to the die [2].*

The goniometer used in the Isen & Smith 2024 publication represents an unprecedented ability to perform goniometry inside an environmental chamber, using a unique and creative approach to traditional goniometry. However, this device is not without limitations; the remote, mechanical nature of the device inside the chamber restricts the measurement range to $\pm 50°$ emission and incidence angles within just the principal plane of the illuminated sample. Additionally, the device arms needed to freely move past each other when measuring a full scattering plane of data, requiring the detector to be offset 15° from the principal plane. This device also suffers from the most common limitation of traditional goniometry techniques; the light source and detector must be repositioned to perform each measurement. This limitation is trivial when working with

samples that do not change dramatically with time, such as rock slices. However, in the case of a goniometer designed to examine dynamic ices inside an environment chamber, the long data collection time can mean the morphology of the ice can be different at the start and end of data collection [2]. The novel goniometer described in this thesis aims to address these deficiencies.

1.3 Addressing the Limitations of Traditional Goniometry with Integrated Goniometry

Examining and modeling the light reflected by various materials first debuted in Bouguer's 1760 publication *Traité d'optique* and Lambert's 1760 publication *Photométria* [40]. Acting as the foundations of reflectance modeling used today, goniometry has used modern available technology to evolve into its current state, using calibrated light sources and digital detectors.

Goniometry as a modern technique was developed around the idea of examining the amount of light reflected off an illuminated sample at many different angles. The source of illumination can either be the sun, or a similarly collimated light source, placed at different angular positions. Using the combination of illumination and examination geometry, intuitively, requires a source and a detector that must be repositioned. It is understandable that this is the design of goniometers used in laboratories today [4, 41, 42, 43, 44, 8, 10, 2], often based on the photometric model developed by Hapke, the technology is well established and well tested [4]. However, traditional goniometry suffers from limitations that restrict what types of samples can be examined.

The nature of the requirement of positionable light sources and detectors means that most goniometers must collect data for one combination of source and detector at a time, making the collection of reflectance [4] data a time consuming process. Additionally, most laboratory goniometers are large, heavy, and have many components [41, 42, 43, 44, 8, 10]. Some light weight automated robotic systems do exist, like the goniometer originally designed for use in the MARVIN chamber at York University used in Isen & Smith 2024 [2]. However, even this system takes approximately 12 minutes to collect $\pm 50^\circ$ of reflectance data, and is restricted to just the principle plane, making it challenging to examine dynamic, time-variable samples with changing reflective properties. These limitations have consistently been a challenge when developing and performing goniometry.

In this thesis, a novel technique for performing goniometry called *integrated goniometry* is discussed.

Integrated goniometry aims to solve the limitations of traditional goniometry by using modern camera technology to directly measure Hapke's REFF [4] at hundreds of angles at once. This is done by illuminating a sample using a fixed set of light sources, but instead of using a positionable detector, integrated goniometry uses a series of reflective surfaces called *secondary reflectors* following the geometry of the hemisphere of reflectance. The secondary reflectors intercept the light reflected off the surface, illuminating them with irradiance from the sample. These surfaces are imaged by a Complementary Metal-Oxide Semiconductor (CMOS) camera with a 150° fish-eye lens [45], projecting the half-hemisphere of the secondary reflectors onto the camera sensor, producing an image containing irradiance data. When an image for a sample is divided by an image for a known reflectance standard like Spectralon™ [7, 8, 9, 10, 4], an image containing REFF data is produced. This data can be extracted from the image using the custom image processing software that I wrote to export the data into digestible file formats to use in reflectance modeling.

To test the concept of integrated goniometry, I developed a proof of concept testing platform goniometer for use on the desktop. The testing platform, shown in figure 1.11, features a 3D printed dome with a basement and aperture. The inside of the dome and basement are painted matte black to absorb stray light, and the aperture in the basement restricts the amount of light from the wide beams produced by the modular LED light sources at 0°, 15°, 30°, 45°, 60°, and 75° angles of incidence, all of which are collimated with plano-convex lenses. The white lines in figure 1.11X are the secondary reflectors mounted inside the black dome. This device is designed for testing new parts, camera configurations, software updates, and for diagnosing systematic problems.

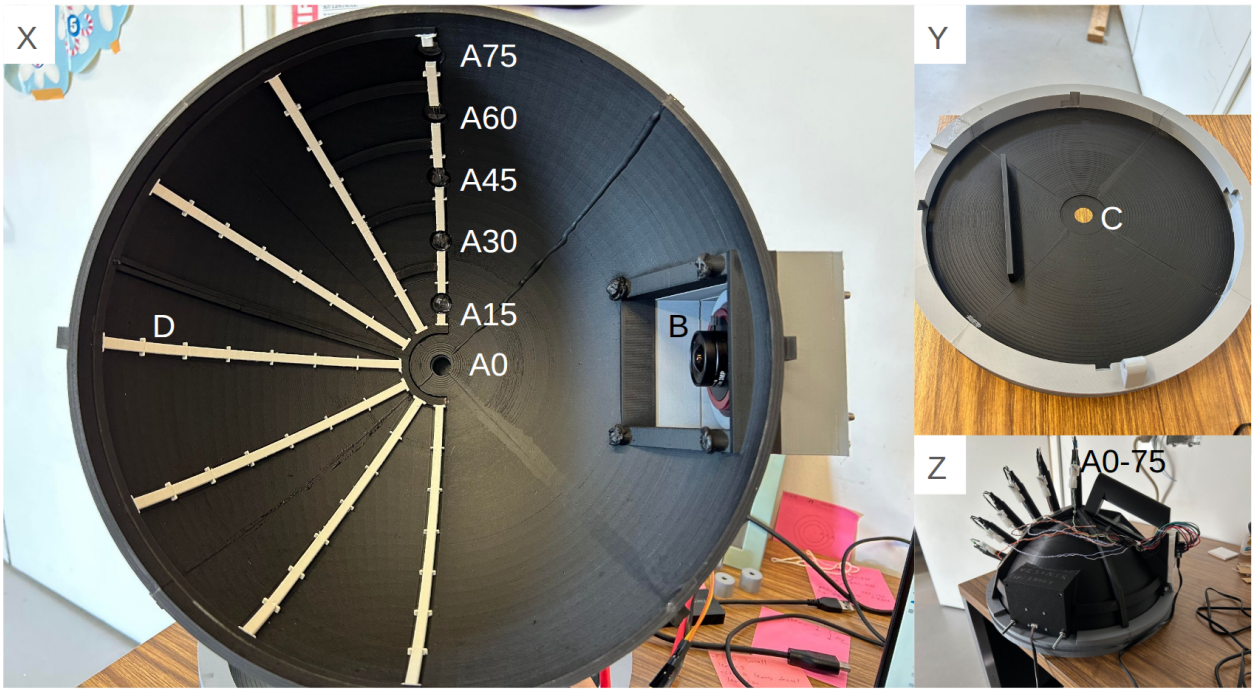

Figure 1.11: *The portable integrated goniometry experimental platform designed for testing device configurations. X) is a view of the inside of the goniometer, Y) is a basement containing an aperture to restrict the amount of light that hits the sample, and Z) is the fully assembled device. A0-75) are the light sources and their apertures based on modular LED sockets with plano-convex collimating lenses. B) is a ZWO ASI662MC CMOS camera mounted to the dome [45]. C) is a narrow aperture to restrict the light hitting the sample, and the white arcs are the secondary reflectors shown by D). The tick marks at 10° increments on the secondary reflectors are for angular position calibration, not for data collection.*

To examine evolving CO_2 ices, I developed and implemented an integrated goniometry system for use in the MARVIN chamber at York University [1], shown in figure 1.12. This variant of the goniometer is constructed out of aluminum and 3D printed components printed using Prusament PC Space Grade Black filament [46]. It is designed as a skeleton device to benefit experiments performed in the MARVIN chamber, allowing the cooled shroud outside the goniometer to absorb radiation coming from the sample [1]. The shroud is painted with light-absorbing, high emissivity black paint, allowing it to absorb stray light inside the chamber, alleviating the need for a black dome enclosing the goniometer [1]. The device captures a series of images for incidence angles of 0°, 15°, 30°, 45°, 60°, and 75°, which generally takes around 5 to 15 seconds to capture a frame for each angle of incidence. This goniometer captures reflectance data over a half hemisphere of reflectance in one measurement for each angle of incidence, accurately collecting goniometry data on evolving time variable samples, while being compact, lightweight, and without the need for any moving parts.

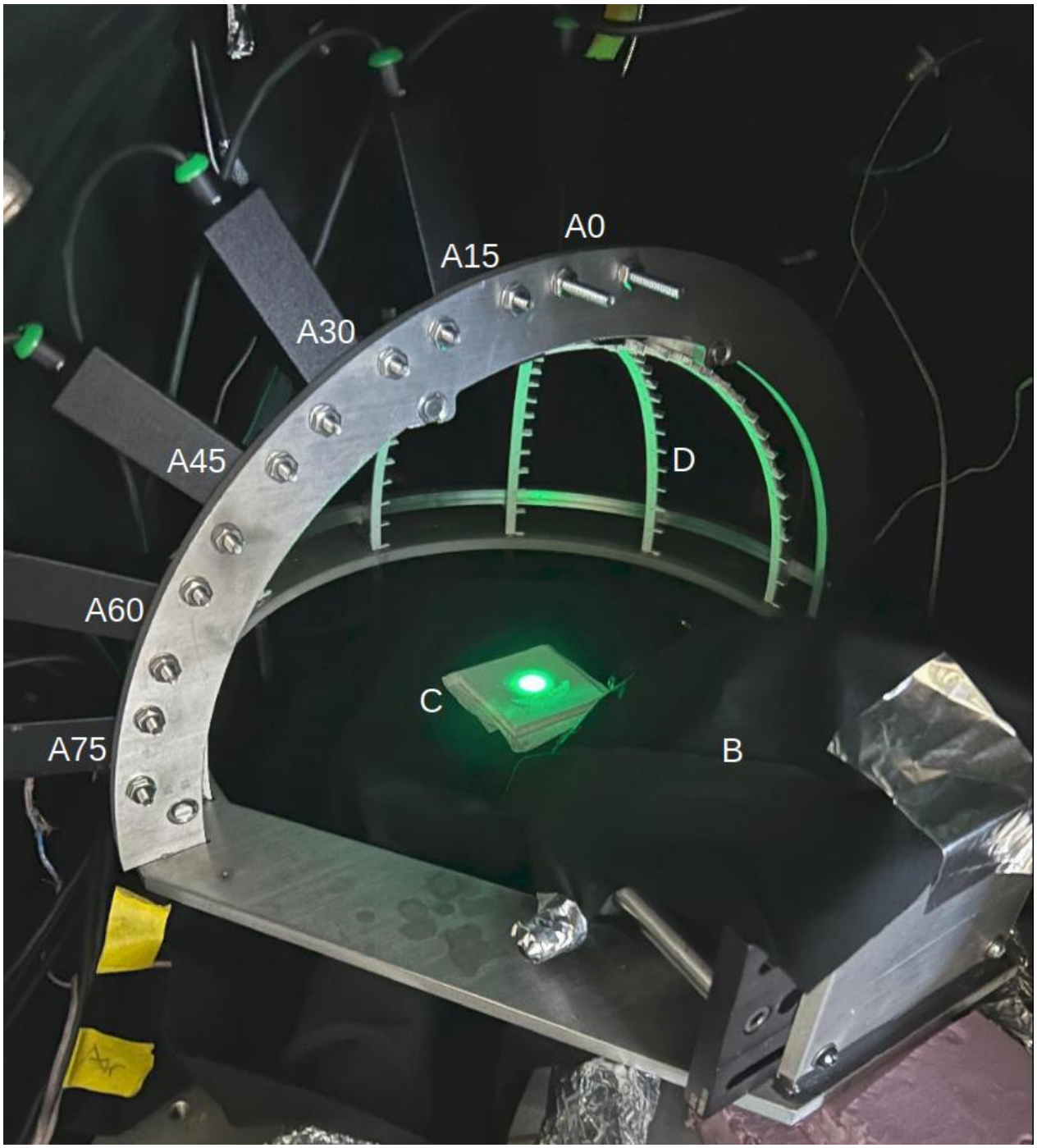

Figure 1.12: *The integrated goniometry system developed for the MARVIN chamber [1]. A0-75) are the light sources based on Thorlabs PL203 520 nm lasers expanded to 10 mm spots [47]. B) is a ZWO ASI662MC CMOS camera covered in black fabric [45]. C) is an illuminated sample of Spectralon™, and D) the white arcs illuminated by green light are the secondary reflectors. The tick marks at 5° increments on the secondary reflectors are for angular position calibration, not for data collection.*

1.4 Complementary Metal-Oxide Semiconductor (CMOS) Imaging Sensors

Complementary Metal-Oxide Semiconductor (CMOS) image sensors have been becoming more and more common in modern applications due to their increasingly strong low noise performance. Early variations often exhibited high read noise and low sensitivity compared to charged-coupled devices (CCD). However, these deficiencies have been minimized significantly through improvements to pixel architecture, signal processing techniques, and improved readout circuitry, leading to improved signal-to-noise ratio (SNR) performance, and high dynamic ranges. Built on a modern pixel design based on the active pixel sensor (APS) architecture shown in figure 1.13, each pixel contains a photodetector and local transistor circuitry that amplifies the signal for readout by a pixel level analog to digital converter (ADC), in addition to a column-level ADC, and a chip-level ADC. This design yields fast image capture times as a direct result of parallel signal extraction across the array [48, 49, 50, 51].

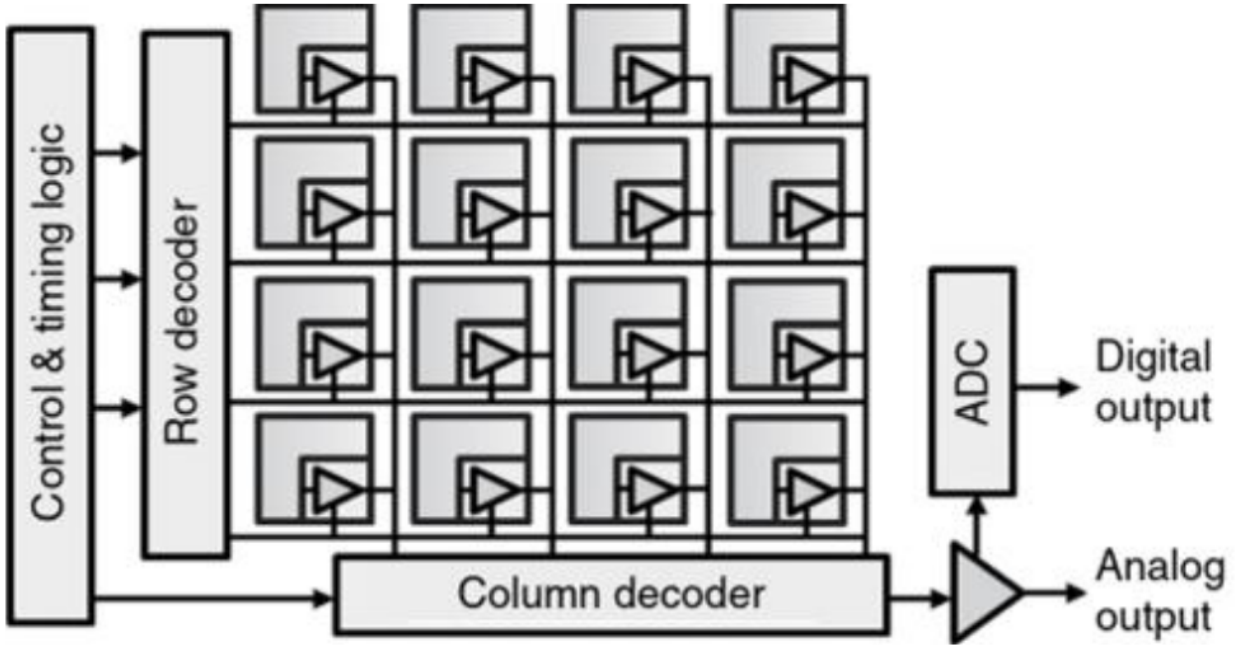

Figure 1.13: *Taken from figure 1 of the J. Lai 2023 publication "The Principle and Design of CMOS Active Pixel Sensor." The layout of a CMOS pixel array using an APS sensor grid. Each square in the grid is a pixel, where the triangles and their attached circuitry are the ADCs for the rest of each photodetecting pixel. The layout of the row and column decoders that read data from each pixel are shown connected to the pixel grid circuitry, connected to the final ADC output system as controlled by control & timing logic. [48]*

This sensor design without alteration will only produce grayscale images since the photodetectors are not wavelength specific. Additionally, a typical CMOS sensor will be constructed out of silicon and is restricted to the detection of photons in a wavelength range of 400 to 1100 nm [52]. When hit by photons, a small

amount of charge will be produced and stored in the electron well of the pixel, producing a small voltage to be read by the pixel ADC [49, 50, 51]. The photon sensitivity of each pixel is limited to the photometric properties of the material the pixel is made out of, producing a curve of pixel photosensitivity as a function of the wavelength. This property is called the quantum efficiency (QE) [53, 54]. Understanding this, if a detector is to produce a color image, it will need to have a Bayer filter applied over the pixel array. A Bayer filter is a per-pixel color filter array that is applied over the pixel array like the one shown in figure 1.14, limiting what wavelengths of light are permissible to the photodetector underneath [55, 56, 57, 58].

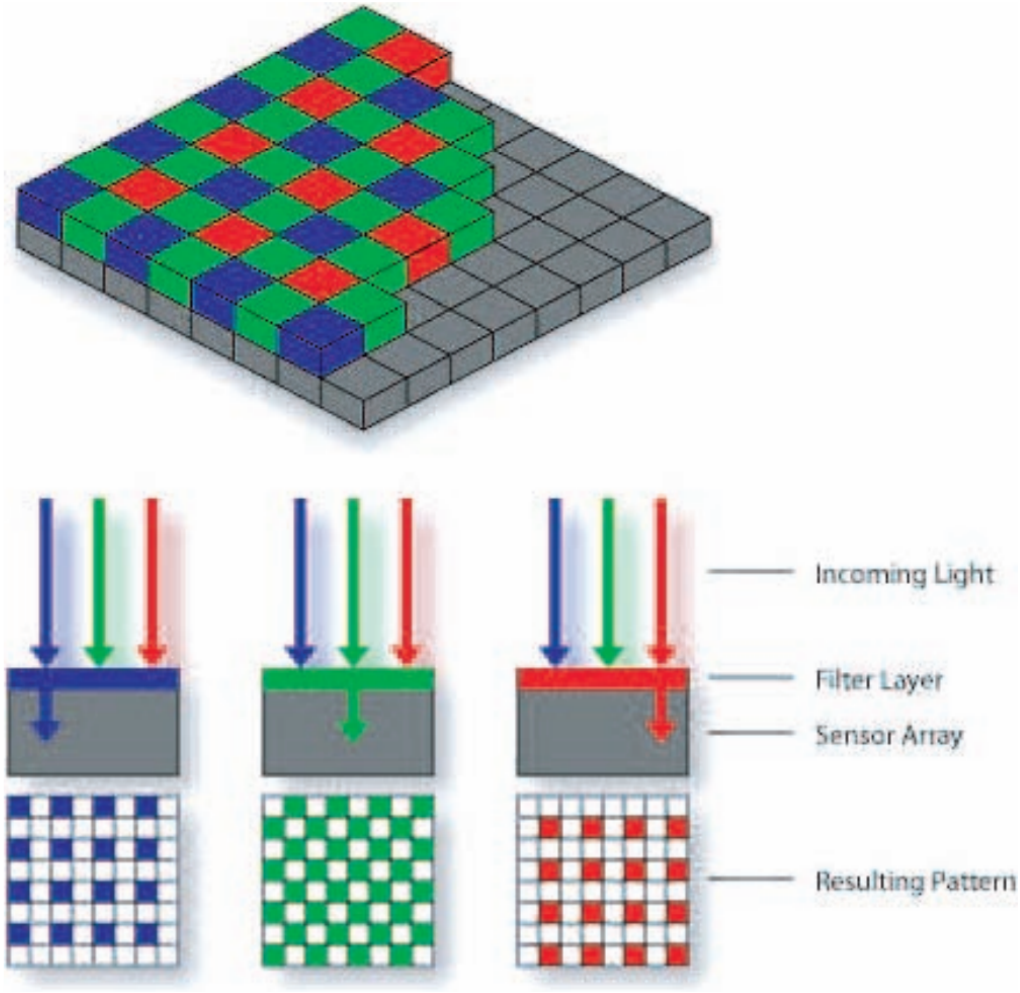

Figure 1.14: *Taken from figure 3.14 of the Paris, Kornprobst, Tumblin, and Durand 2009 publication "Bilateral Filtering: Theory and Applications." Graphic of a Bayer filter showing the checkerboard pattern of the filter over the pixel array, where the different colors represent the red, green, and blue, color filters. [58]*

The image produced by the CMOS calibrated to a Bayer filter will be a grayscale image containing values where the minimum and maximum reported values will be scaled according to the relative intensity of light

that can reach the sensor up to pixel saturation. Using this image, a color image can be recovered using a debayering algorithm that interpolates values between the Bayer filter checkerboard pattern. Producing multiple image layers that when combined, create the full color image [55, 56, 57, 58]. When describing the QE performance of a camera using a Bayer filter, a QE plot for how strongly each pixel responds to light that has passed through the filter as a function of wavelength can be produced like the one shown in figure 1.15 [59, 60, 61]. These QE plots are frequently part of camera sensor marketing material as it is highly suggestive of expected sensor performance.

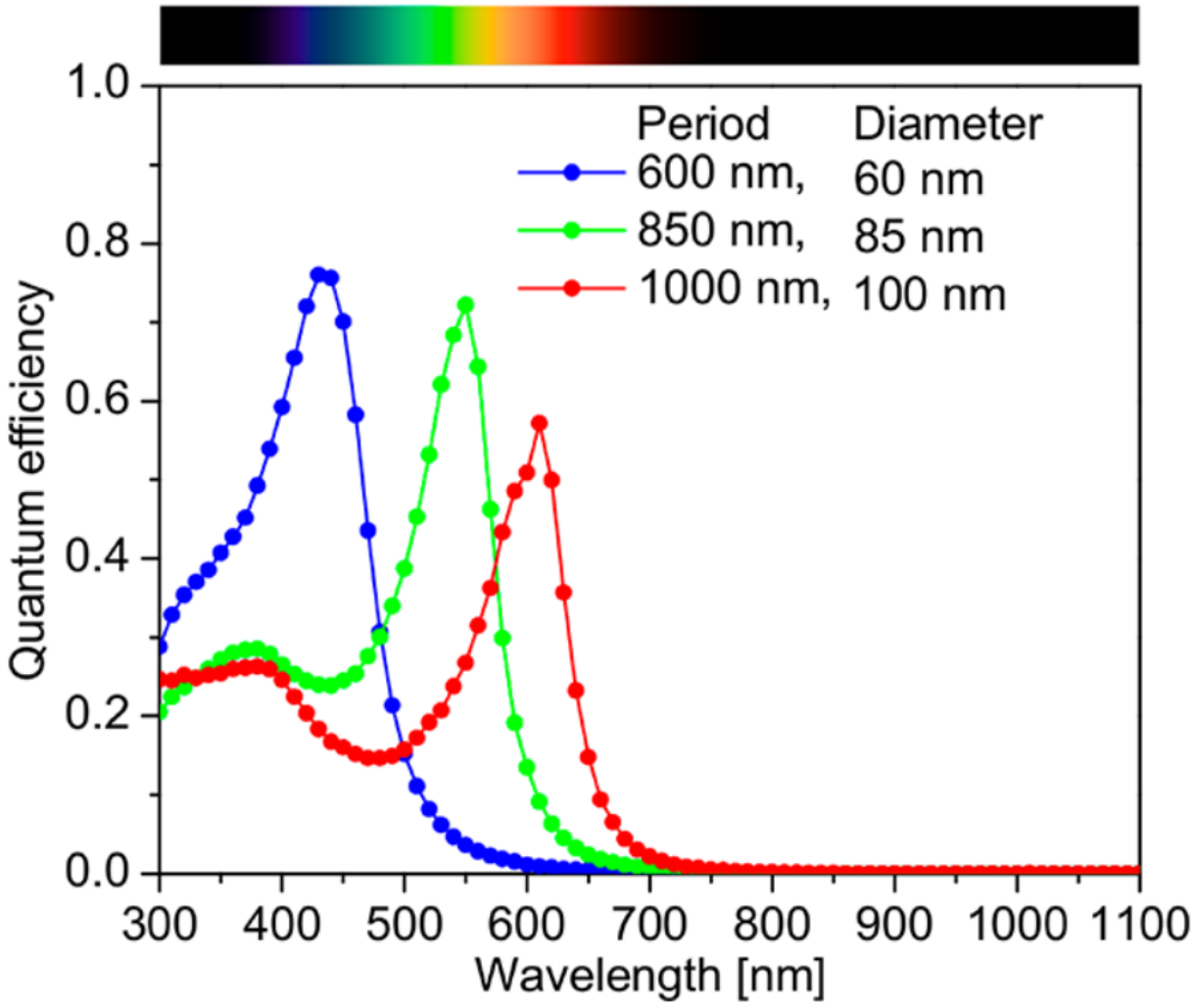

Figure 1.15: *Taken from figure 3 of the Asman Tamang 2019 publication "Color Sensing by Optical Antennas: Approaching the Quantum Efficiency Limit." Example of a quantum efficiency (QE) plot for a color camera using a Bayer filter where the colored lines correspond to the camera response as a function of the incident wavelength of light [60].*

Chapter 2

Integrated Goniometry

2.1 Introduction to Integrated Goniometry

I refer to this novel technique as *integrated goniometry*; this term accurately characterizes the technique for two reasons, the first being that the design relies on using reflective surfaces referred to as *secondary reflectors*. Photons scattered by the illuminated sample reflect off of these a second time before entering a camera; which when analyzed by image processing software, effectively simulates a mathematical integral using physical hardware to gather reflectance data off of a continuous reflective surface. The term is additionally fitting because the nature of using secondary reflectors before photons can enter the detector allows the system to be integrated into a multitude of different systems. For example, an experimental chamber with an exposed sample can be fitted with a board, dome, or hemispherical scaffolding containing secondary reflectors in such a way that they intercept the hemisphere of reflectance coming off an illuminated sample. With the addition of a means of obtaining reference standard measurements, and the inclusion of a camera that can image the secondary reflectors, users can perform goniometry.

Integrated goniometry enables photogoniometry to be performed without a cumbersome apparatus by use of direct imaging hardware like a complementary metal-oxide semiconductor (CMOS) or charge-coupled device (CCD) camera to analyze reflectance data for different materials. Compared to a traditional goniometry setup, which requires a large, heavy, application specific apparatus with many moving parts, this method enables the construction of lightweight, portable, compact, and easy to install devices, that can be taken to the field or installed into experimental apparatuses connected to a computer to collect data rapidly. During operation, users take a background measurement used for noise reduction [62], a reference measurement of

a white near-Lambertian sample, and measurements of samples of interest [4], while only requiring the user to exchange the sample being measured.

In the goniometry system described in this thesis, the configuration of the standard test system computer consists of an AMD Ryzen AI 5 340 6-core CPU with 16 GB of LPDDR5X memory, running Fedora Linux. During operation, the system typically produces data in roughly 1 to 2 minutes depending on the device configuration. The data gathering process involves two major steps, (1) gathering data using a CMOS camera and (2) extracting reflectance data from the images into data points. Step 1 for the first of two configurations, takes approximately 30 seconds to gather frames at 5 second exposures for each of the six angles of incidence, and approximately 1 minute for the second configuration that stacks 10 0.5 second frames for each of the six angles of incidence. Both configurations save the frames as python numpy array files [63]. Step 2, the computer takes approximately 60 seconds to convert the captured data frame into data points using a data extraction and data averaging function from my Python 3 library.

2.2 Concept

When performing integrated goniometry, the camera views the secondary reflectors on a pixel grid, which effectively allows each pixel in the grid to act as a tiny detector. This gives secondary reflectors the ability to view an array of emission and azimuth angles simultaneously, rather than having to position the detector at each angle individually. However, secondary reflectors need to be optimized to reduce light bounced from one secondary reflector to another [64]. If the scattering plane is to be preserved, this effect cannot be completely eliminated; however, it can be mitigated by configuring the secondary reflectors to occupy narrow data ranges. In the goniometer discussed, the reflectors are 5 mm wide with a 150 mm radius from the center of the measurement hemisphere, occupying a 1.9° azimuthal arc length 'width' when measured from the 90° emission angle. In this configuration, the angular coverage projected onto the pixel array corresponds to emission and azimuth angle resolutions of approximately 0.2° to 0.3° per pixel.

When the software collects reflectance data for a position along the secondary reflector, that position corresponds to an angular range centered at any position along the secondary reflectors. The collected data is dependent on the angular area of the hemisphere that each pixel is viewing. Figure 2.1 shows a diagram of how the pixels in the detector view a secondary reflector.

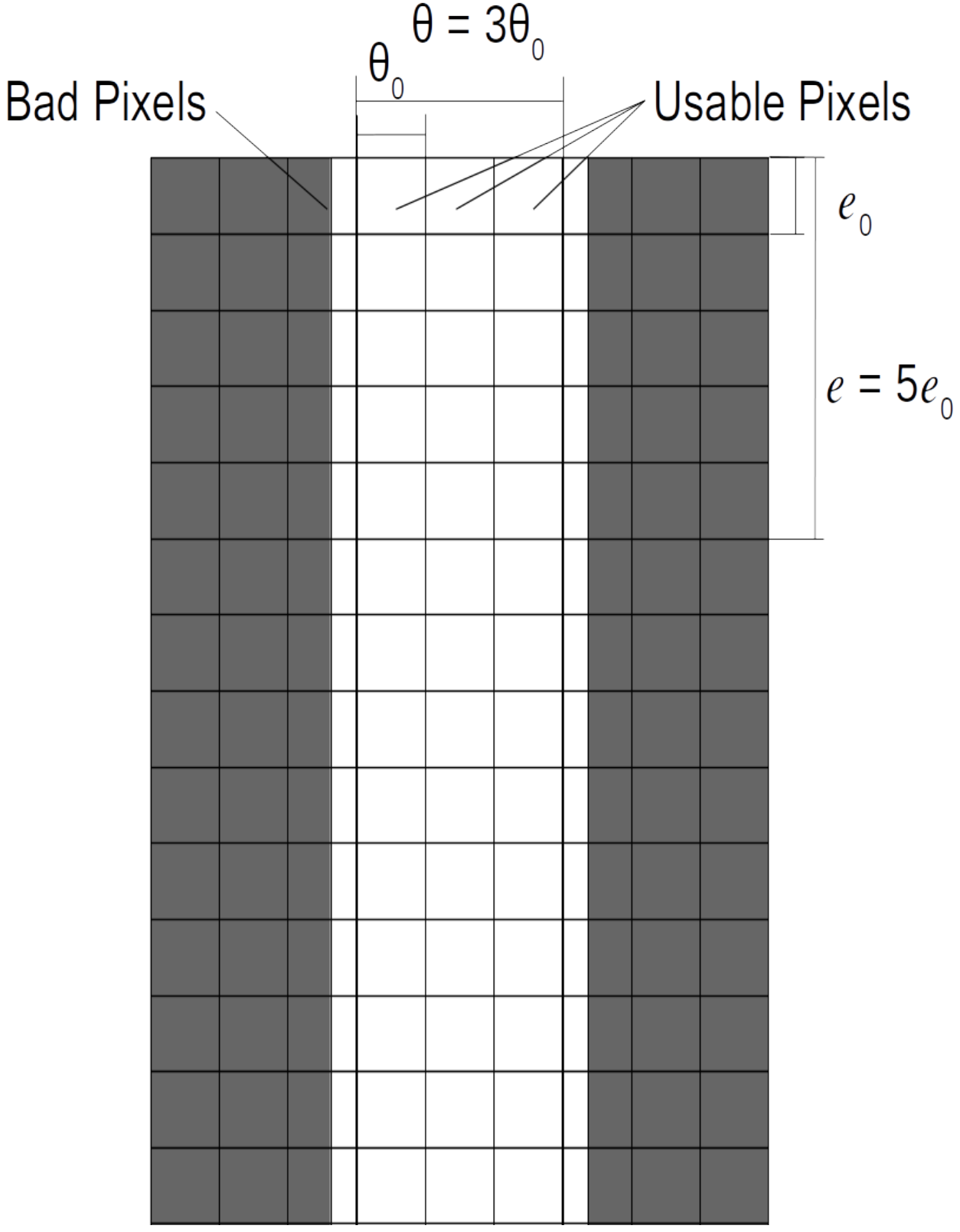

Figure 2.1: *An illustration of one of the secondary reflectors in white with the background in dark gray, with the pixel grid from the detector shown as the grid lines overtop the image. When the device is performing image analysis it adds up the values of horizontal lines of pixels before adding these lines together for a given range of vertical pixels that are determined using an angular positioning calibration algorithm for emission and azimuthally aligned pixels.*

Figure 2.2 shows the positional configuration of the secondary reflectors at 30°separations. In this device configuration, light starts at the illumination source, scatters off the sample, scatters again off the secondary reflectors, and into the camera. This is the core design characteristic of integrated goniometry.

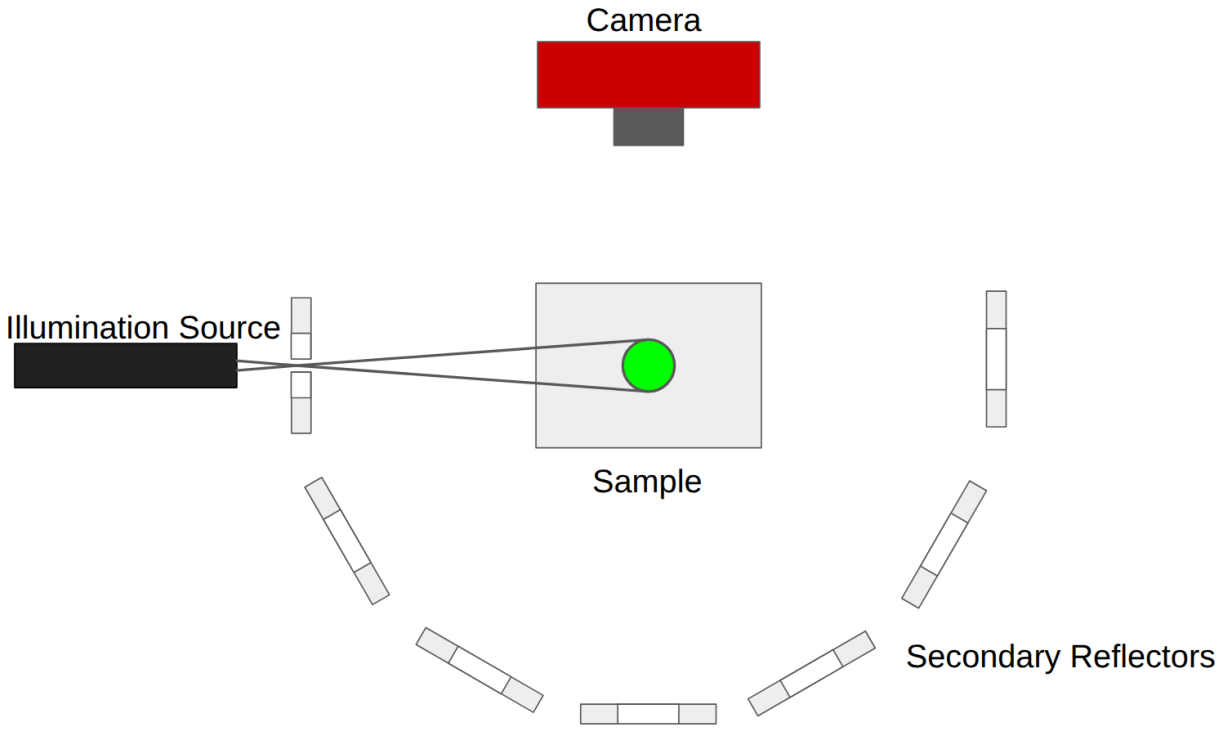

Figure 2.2: *A schematic of the integrated goniometry system showing the relative positions of the secondary reflectors around the illuminated sample with the camera positioned to image the secondary reflectors. Note the beam from the illumination source is designed to pass through a small gap in the secondary reflector in the path of the beam.*

2.3 Hardware, Design, & Execution

Conceptually, implementing an integrated goniometry system involves intercepting reflected light from multiple known positions at once, introducing surfaces that re-scatter the light so a single detector can observe reflectance at multiple positions simultaneously. When a detector output frame is compared to that of a known near-Lambertian scatterer, a numpy array frame containing REFF data is generated [4, 63].

The physical design of our goniometer intercepts reflectance from the sample by using machined aluminum secondary reflectors mounted to an aluminum structure that houses the camera and light sources. The secondary reflectors are mounted 150 mm from the point of illumination on the sample. When the device is placed in the MARVIN chamber [1], the light absorbing shroud enclosing the device and sample platter prevents excess light rays from scattering back into the camera or onto the secondary reflectors. The

goniometer (figure 2.3) as installed inside the MARVIN [1] is shown in figure 2.4. The tick marks along the secondary reflectors are at known angular increments of 5° starting at 5° from the zenith, to 90° from the zenith. These tick marks are not used for data collection; instead, they are used to calibrate my python code so that REFF data extracted from data frames is correlated to accurate angular positions.

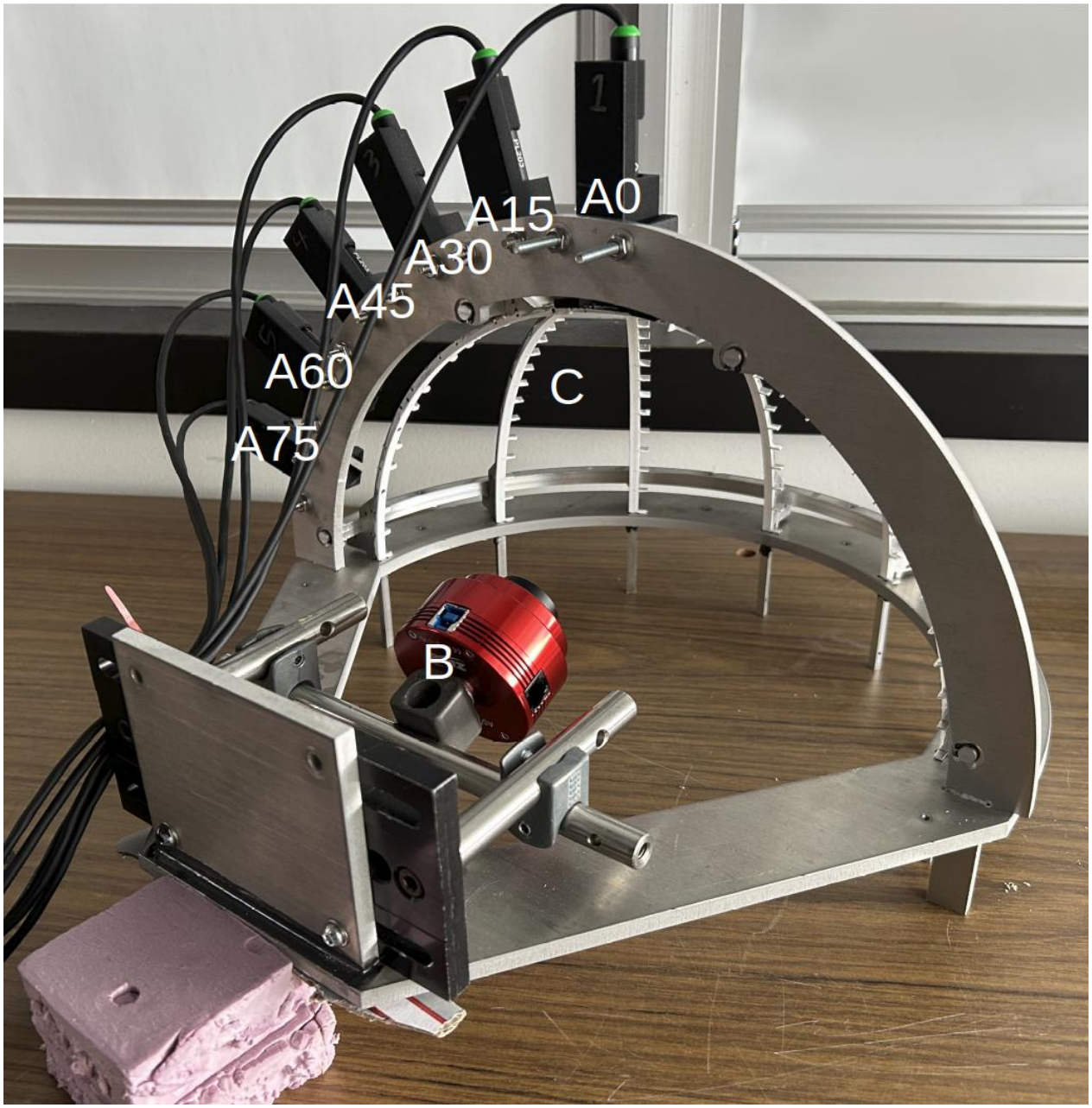

Figure 2.3: *The fully assembled goniometer outside of an operational environment. A0-A75) are the light sources following the design laid out in figure 2.5. B) is the ZWO ASI662MC camera, with a blue USB type B port visible, mounted to an adjustable mount fashioned out of optics bench parts. The arcs shown in C) are the secondary reflectors painted white at 30° azimuthal separations. The tick marks along the secondary reflectors are positioned in 5° increments, these are used to calibrate the data extraction algorithm as a means of identifying known angular positions along the secondary reflectors and are not part of data collection. The system is propped up on a chunk of pink insulation foam for the purpose of the picture as the system is designed to rest on top of the LN_2 input lines of the cold plate in the MARVIN chamber [1].*

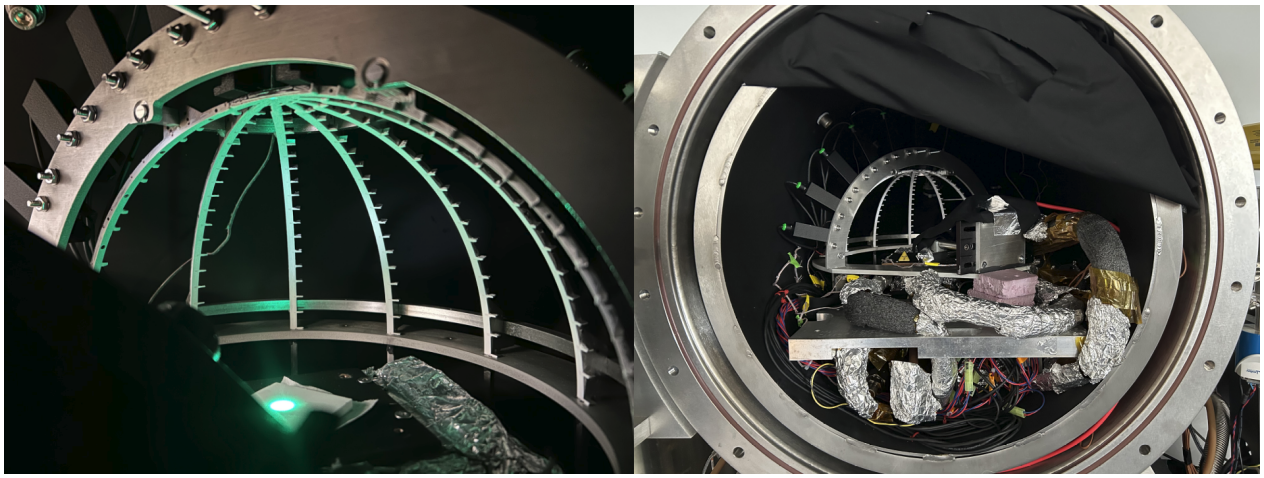

Figure 2.4: *On the left is a view of the goniometer inside the MARVIN chamber [1] viewing the secondary reflectors while a sample of Spectralon™ is illuminated. On the right is a view looking into MARVIN [1] with the door of the chamber open with the goniometer inside overtop the chamber cold plate, with the LN_2 lines running under the base of the goniometer (right).*

When ice samples are grown to a thickness of 0.5 cm, the measurement planes of both the ice and the goniometer are aligned flush with each other. To illuminate the sample, a set of Thorlabs PL203 520 nm 0.9 mW lasers (table 2.1) with 45° oriented polarization planes from the plane of incidence and are expanded by using 15 mm diameter, 45 mm focal length, plano convex lenses (table 2.2), expanding the beam to 10 mm when illuminated from the zenith. This beam is fired through the secondary reflectors by firing the laser beam through the lens, and passing the focal point of the beam through a 3 mm hole in the secondary reflectors at 0°, 15°, 30°, 45°, 60°, and 75° illumination angles measured from the zenith. The configuration of this laser pass-through technique is illustrated in figure 2.5.

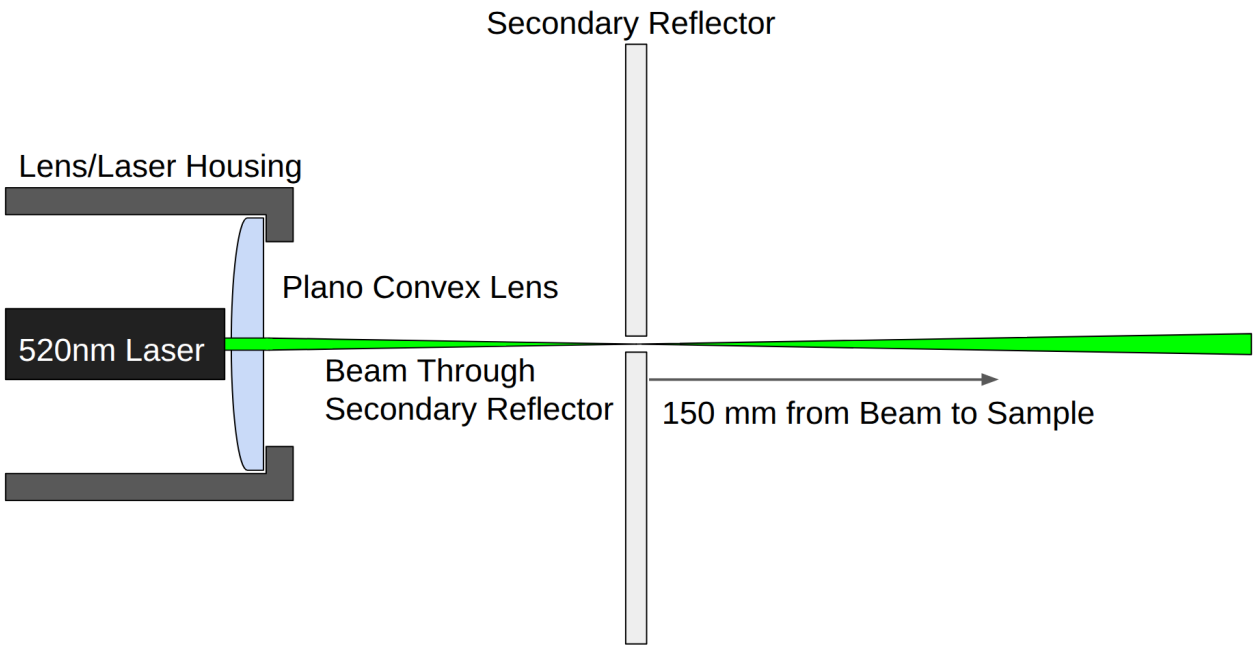

Figure 2.5: *Schematic of the incident beam passing though the secondary reflector in the direction of illumination. The Thorlabs PL203 520 nm 0.9mW laser is passed through the secondary reflector and expanded to a 10 mm spot size by converging the beam through a Edmund Optics 45.0 mm Effective Focal Length (EFL) plano-convex lens. The hole in the secondary reflector is placed at the focal length of the lens, allowing the beam to pass through unaffected, and expand to a 10 mm spot over the 150 mm travel distance to the sample. The laser and lens are held in a 3D printed housing printed with Prusament PC Space Grade Black filament [46].*

Specification	Min	Typical	Max
Wavelength	510 nm	520 nm	530 nm
Output Power	0.8 mW	0.9 mW	$<$1.0 mW
Polarization Extinction Ratio		20 dB	
Power Stability (8 Hours)			1%
Power Stability (1 Minute)			0.2%
Axis Deviation			5 mrad
Beam Diameter		3.0 mm	
Beam Divergence		-0.6 mrad	
Operating Voltage	4.9 V		5.2 V
Operating Current		70 mA	90 mA

Table 2.1: Specifications of the Thorlabs PL203 520 nm 0.9 mW lasers used to illuminate samples [47].

Optical Properties		Physical & Mechanical Properties	
Effective Focal Length EFL (mm)	45.00 @ 587.6nm	Diameter (mm):	15.00 +0.0/-0.025
Back Focal Length BFL (mm):	43.35	Centering (arcmin):	<1
Coating:	Uncoated	Center Thickness CT (mm):	2.50 ±0.10
Surface Quality:	40-20	Edge Thickness ET (mm):	1.26
Power (P-V) @ 632.8nm:	1.5λ	Clear Aperture CA (mm):	14
Irregularity (P-V) @ 632.8nm:	$\lambda/4$	Bevel:	Protective as needed
Focal Length Tolerance (%):	±1		
Radius R_1 (mm)	23.26		
f/#:	3		
Numerical Aperture NA:	0.17		
Wavelength Range (nm):	350 - 2200		

Table 2.2: Specifications of the Edmund Optics plano-convex lenses used to expand the beam of the lasers [65].

To verify stable power output from the Thorlabs PL203 lasers [47], the beam from a laser was directed onto a model 818-SL photodiode connected to a Newport 1830-C optical power meter [66, 67]. The results shown in figure 2.6 demonstrate rapid stabilization and consistent output power upon startup from a cold state. The laser reached a stable operating power immediately, exhibiting no appreciable warm-up period and maintaining steady output throughout the measurement.

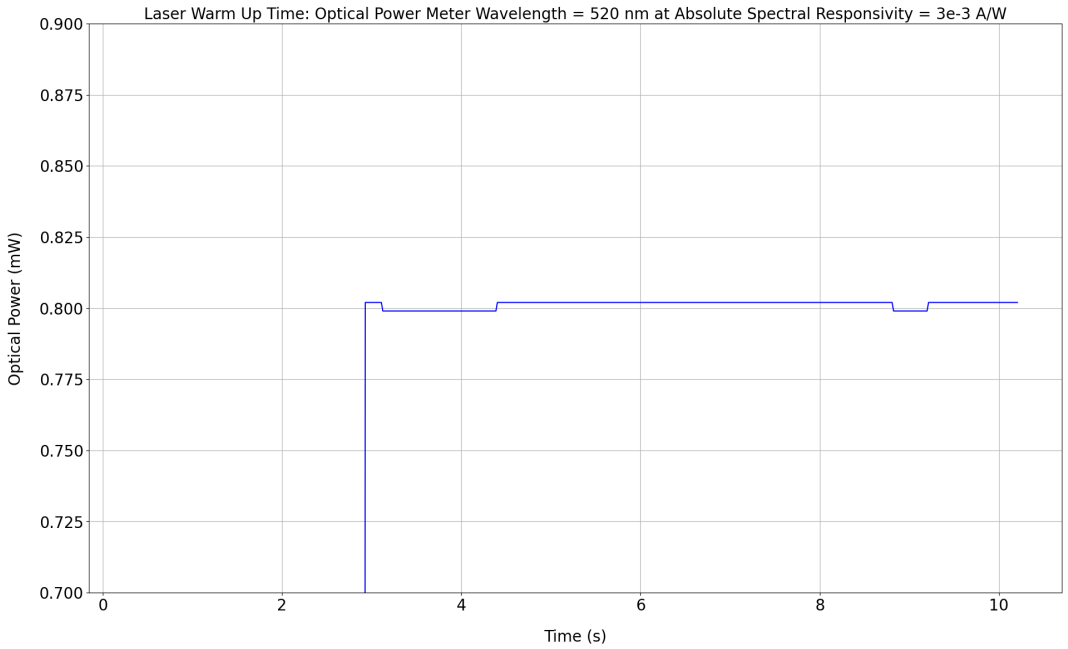

Figure 2.6: *Optical power output of the Thorlabs PL203 520 nm laser [47] measured with a model 818-SL photodiode connected to a Newport 1830-C optical power meter [66, 67] set to 520 nm with an absolute spectral responsivity of 3e-3 A/W. The laser shows no appreciable warm up time and maintains stable power output at 0.8 mW.*

The camera used is a ZWO ASI662MC 1920x1080 astrophotography camera [45] with specifications shown in table 2.3. The camera is controlled with a python wrapper for the manufacturer provided ZWO ASI Linux command API. When called by my python code the camera images the secondary reflectors, capturing either a single 5 second exposure frame, or stacking 10 0.5 second exposures into a single frame.

Specification:	Value:	Specification:	Value:
Sensor:	Sony-IMX662	QE Peak:	91%
Type:	Color/Mono	Full Well Capacity:	38.2Ke
Sensor Format:	1 / 2.8”	ADC:	12bit
Diagonal:	6.45mm	USB Interface:	USB 3.0/2.0 Type-B
Resolution:	2.07MP 1920 x 1080	Adapter:	1.25”/2”/M42 x 0.75
Pixel Size:	2.0μm	Protect Window:	φ21-1.1 AR
Sensor Size:	5.568mm x 3.132mm	Dimension:	62mm
Fast Frame Rate:	107.6fps	Weight:	126g
Shutter:	Rolling Shutter	Back Focus Distance:	12.5mm
Exposure Range:	32μs 2000s	Supported OS:	WIN7/8/10 32&64 bit, Linux, Mac
Read Noise:	0.8-6.9 e(1.22e@19db gain)		

Table 2.3: Specifications of the ZWO ASI662MC camera used to image the secondary reflectors [45].

My custom Python library processes camera frame data using calibrated configuration files that define the pixel regions of interest within each frame, following the secondary reflectors. Pixel values are extracted over a specified width (typically 5 to 9 pixels) and exported to .csv and .xls formats for further analysis. The typical processing pipeline for collecting REFF proceeds as follows:

1. A background subtracted frame for an illuminated sample of interest is divided by a background-subtracted frame of a known reference sample, usually Spectralon™ [15], producing a frame containing REFF data [62, 4].

2. Pixel data is extracted from the configured regions along the secondary reflectors inside the REFF frame.

3. The extracted values are grouped according to a defined latitudinal bin size.

4. For each bin, the software sums the pixel values while tracking the number of contributing pixels.

5. The summed values are normalized by the number of pixels in each bin to compute their average REFF values.

6. REFF data is exported to .xls and .csv files for analysis.

Step one of the processing pipeline is visualized in figure 2.7, showing how data frames are background subtracted and divided to produce the REFF frame used for data extraction.

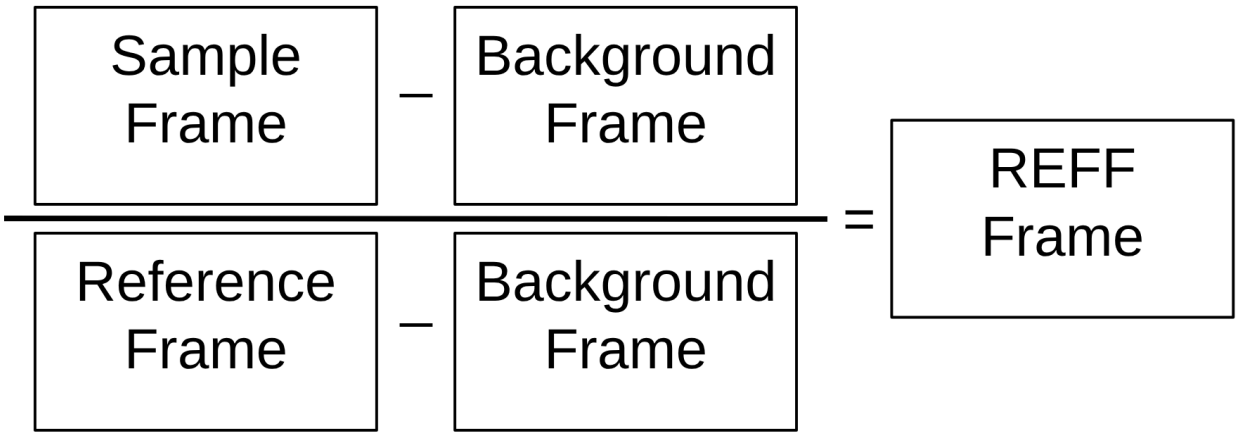

Figure 2.7: *Visualization of the frame division process implemented to produce frames containing REFF data. The background frame is subtracted from both the sample and the reference frame, then the resulting background subtracted frames are divided by each other, producing the REFF frame that data is extracted from.*

The processed data can then be visualized using various techniques, including three-dimensional plots (figure 2.8), scattering plane plots (figure 2.9), and interpolated heat maps (figure 2.10). The data in figures 2.8, 2.9, and 2.10 is presented as REFF to demonstrate the data format output directly from the device. The data interpolation used in figure 2.10 and throughout this thesis is performed by feeding reflectance data into a SciPy nearest neighbor interpolation routine, with this first interpolation output fed into a SciPy minimum curvature interpolation routine to produce the final interpolated data [68]. This combined interpolation system is designed to smooth the data while minimizing smearing effects around localized spikes in reflectance; however, the process is not perfect, and some degree of smearing remains unavoidable in extreme, localized cases.

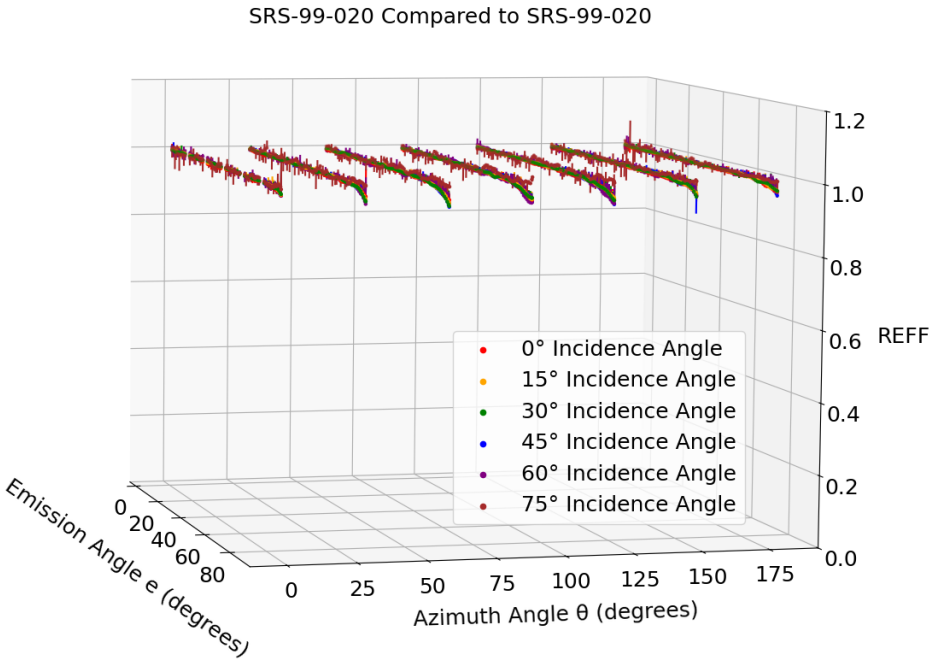

Figure 2.8: *The REFF values of SRS-99-020 compared to itself. Data points are plotted in 3D with the emission angle and azimuth plotted on the x and y axies, and REFF with associated error-bars plotted on the z-axis. REFF values near 1 reveal that the system is collecting stable data, suggesting that the data frames captured by the camera and divided by each other are producing consistently equivalent values.*

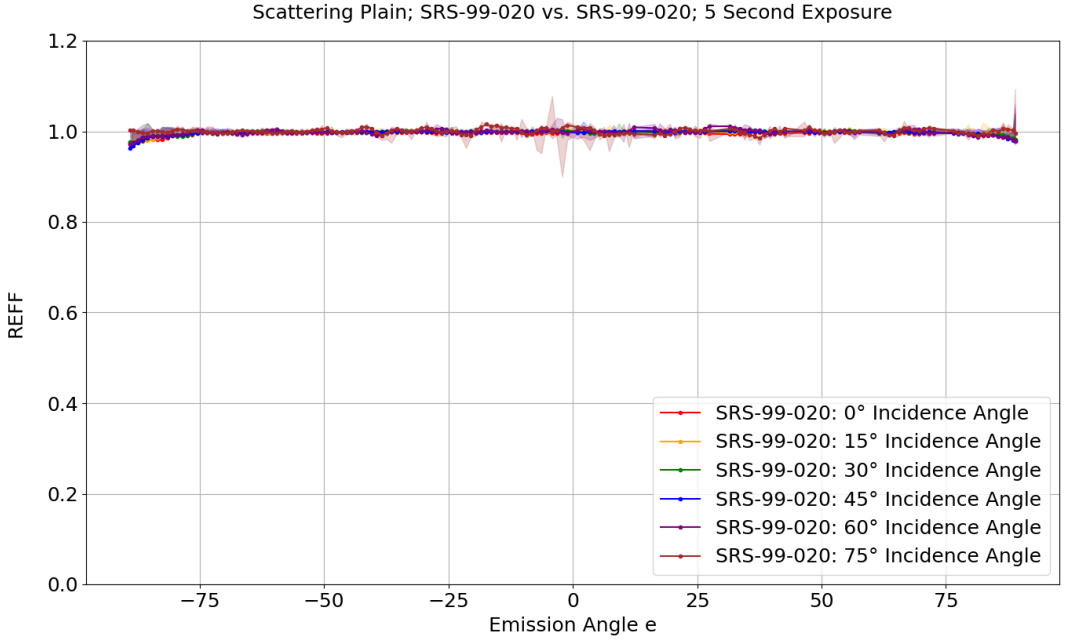

Figure 2.9: *The scattering plane of SRS-99-020 compared to itself. REFF values near 1 suggest stable data collection reporting expected results when comparing the reflectance standard to itself. Error is shown as shaded regions on the plot in the same color as the main data line the shaded area is representing.*

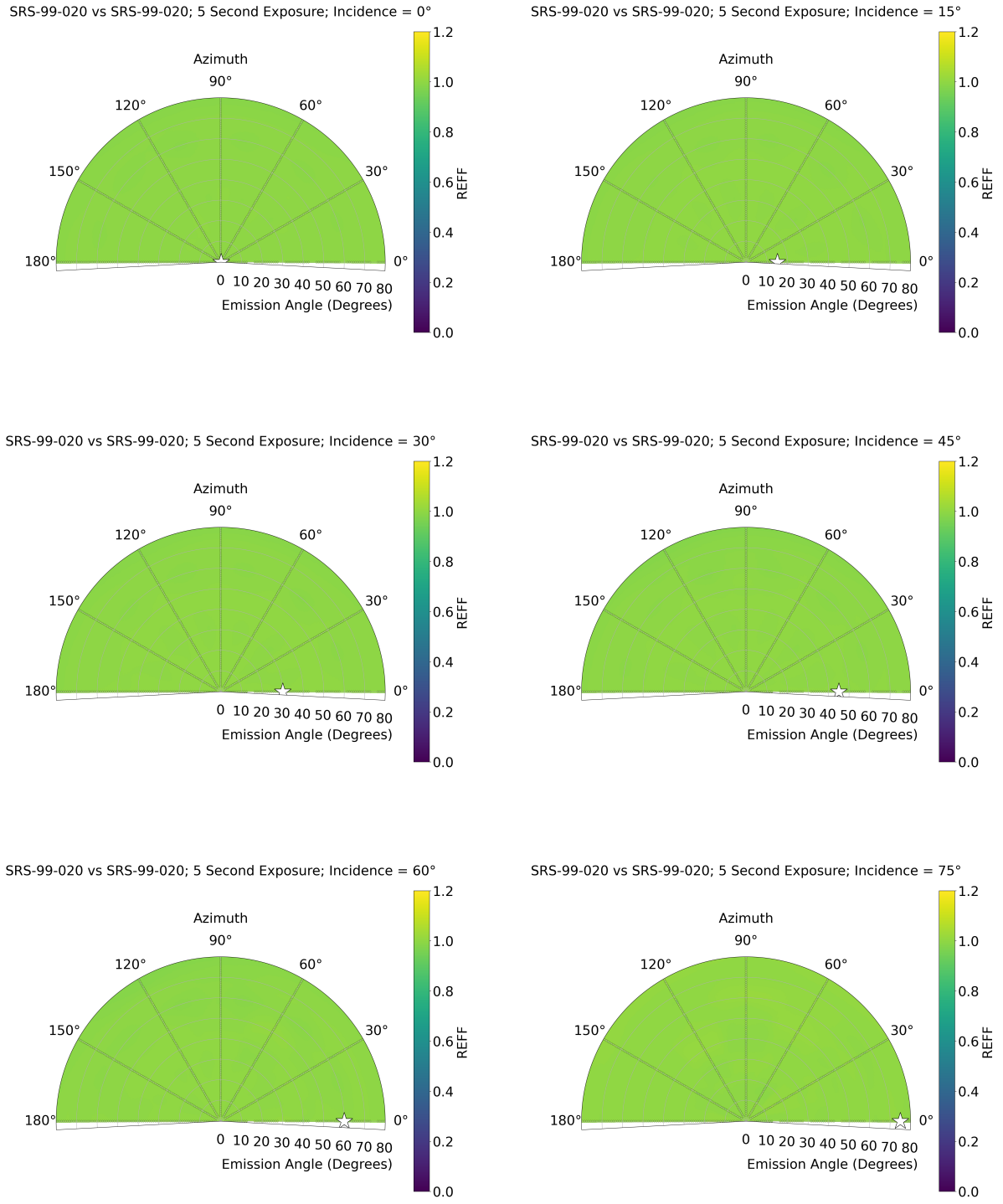

Figure 2.10: *The interpolated heatmap of SRS-99-020 compared to itself shows a constant reflectance across all plots with no visible interpolation artifacts. The star on each plot represents the position of the incident light, and the lines at 30° azimuthal separations are the positions of the secondary reflectors where data points are taken directly from the goniometer before interpolation. Data is interpolated by feeding reflectance data into a SciPy nearest neighbor interpolation routine, this output is then fed into a SciPy minimum curvature interpolation routine [68].*

2.4 Code

Fundamentally, the code implemented operates as a photometry library, analogous to the ones used to analyze telescope or spacecraft images, where data is gathered by adding up the values of pixels in the image. However, where it differs is the ability to add up a continuous line of pixels following the secondary reflectors. This process requires some additional calibration steps to ensure that the data correctly represents the reflectance values for different angles.

To collect data from the goniometer, the code needs to know where to look in the image to extract reflectance data and know what position pixels along the secondary reflectors correspond to. To accomplish this, the device uses a calibrated data extraction algorithm. The algorithm is calibrated with a function that turns on the laser at the zenith, lowers the exposure to 0.5 seconds, raises the camera gain to 400 out of the maximum value of 600, and starts an interactive video stream. The exposure and gain settings during this stream are different from the data collection settings since the goal is for the stream to make the secondary reflectors easy for the user to see, while preserving a usable frame rate. During the stream, the user selects a set of points in the image at known emission angles and azimuths. The positions of known altitudes and azimuths are marked by white tick-marks along the secondary reflectors at 5° emission angle separations starting at an emission angle of 0° and ending at an emission angle of 90°. When these positions are selected, the code associates the coordinate data at these points with an internal library of their known azimuth and emission angle positions. This data is used to generate a pixel map lookup table with azimuth and emission angles corresponding to pixel coordinates anywhere along the secondary reflectors. The calibration table is exported as a numpy array file containing interpolated pixel coordinate data corresponding to the positions of each secondary reflector in the data frames [63]. Emission and azimuth angle data is saved to the lookup table file that, when loaded into the python code, receives coordinate data of pixels along the secondary reflectors, and returns the azimuth and altitude position of queried pixels. These files are used throughout the data extraction process as lookup tables for determining the angular positions of pixels along the secondary reflectors. Figure 2.11 is an image saved at the end of the calibration stream visualizing the selected pixel coordinates and their values as calculated by the lookup table. It is critical to note that if the position of the camera relative to the secondary reflectors changes, the calibration will be misaligned and must be corrected, typically by re-running the calibration process.



Figure 2.11: *Image produced by the goniometer calibration function for verifying the quality of the data extraction algorithm calibration. White crosshairs are placed where the user selects the calibration points. The interpolated azimuth and emission angle values output from the lookup table are printed next to each crosshair so the user can verify the accuracy of the interpolated angular positioning calibration. Black lines following the secondary reflectors are placed in the image where data is to be extracted from, with a thin white line in the center of the black line placed at the center-point of the black line.*

Upon code execution, Python connects to an Arduino™ that is connected to six MOSFETs in a control box (figure 2.12) that allows power to be sequentially passed to the six lasers. Toggled digitally by the digital output pins on the Arduino™, it starts by turning on the first laser at the zenith of the goniometer to illuminate the sample, then uses the camera control API to connect to the CMOS camera and start collecting image data to be saved as numpy array frames [63]. The frames are then background subtracted, and divided by the reference frame collected using the same methodology [62, 4]. Once the frame for the zenith illumination angle of incidence is saved, the laser is toggled off and the next laser at 15° from the zenith is toggled on and performs the same frame collection and processing steps, sequentially repeating the process until each of the lasers has illuminated the sample and the respective frames have been saved. Upon completion, the code moves onto data processing to extract data from the frames.

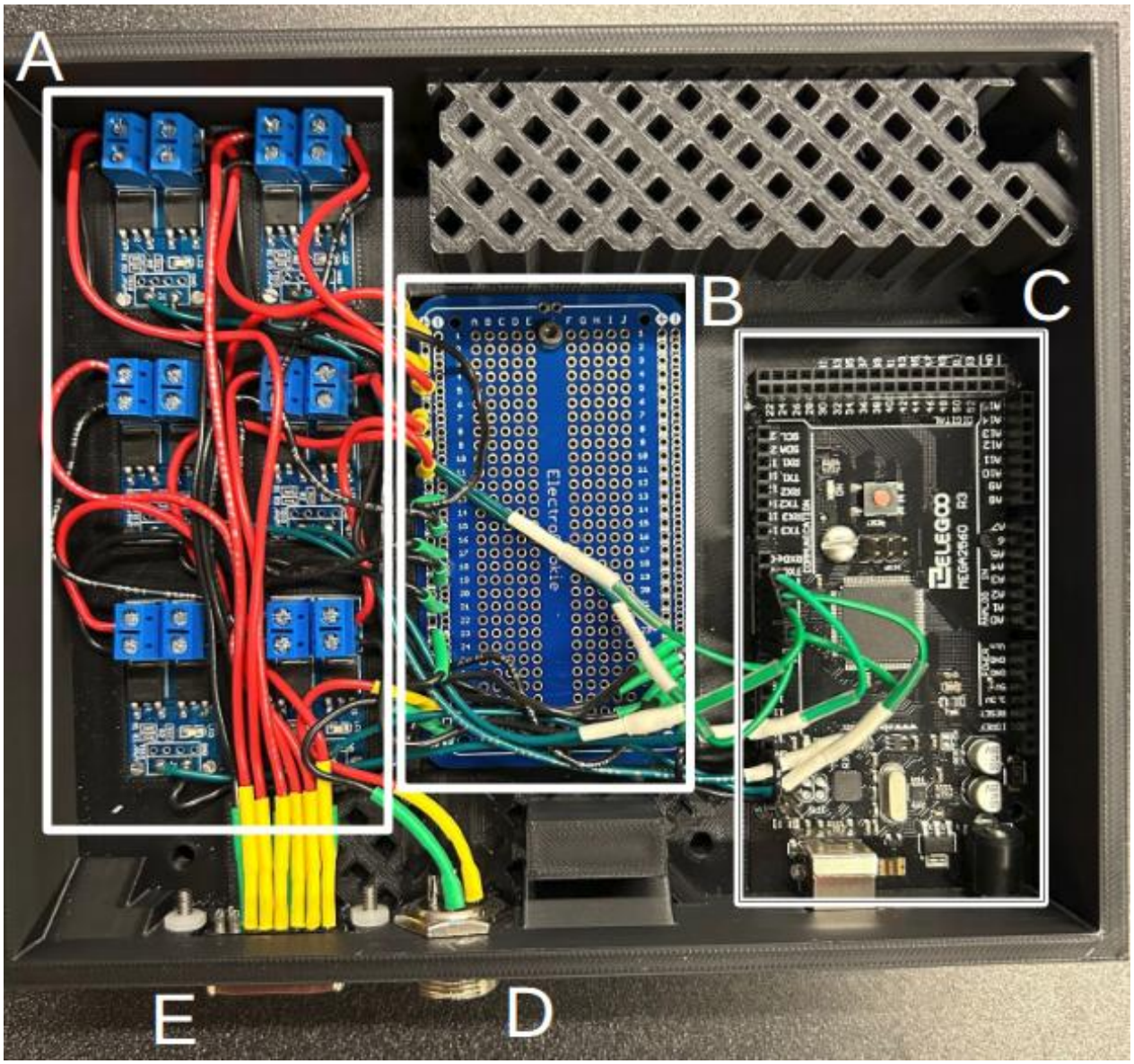

Figure 2.12: *The goniometer power control box. A) is the digital MOSFET array. B) is the power distribution board. C) is the Arduino™ connecting digital output pins to the digital inputs on the MOSFETs. D) is the main power-in plug, and E) is the main power-out plug.*

To extract data from the frames, python loads the known pixel coordinate data range files for the secondary reflectors, and loads the pixel azimuth and emission angle coordinate lookup table. The code begins at the pixel coordinates on the secondary reflector corresponding to the zenith of the secondary reflector at azimuth 0°, defined relative to the azimuth of the illumination sources. Next, it iterates through every vertical pixel position in the range given by the collection ranges, storing the average value of that pixel and the number of horizontally adjacent pixels configured by the user, 4 additional pixels on either side by default, into a .xls and .csv file. This process is repeated sequentially at each iteration starting at an altitude angle of

90° until the pixel position corresponding to an altitude angle of 0° from the device 'horizon' plane of measurement is reached. This process is repeated for each secondary reflector at every azimuth starting with the azimuth of the illumination sources, and repeating for every angle of incidence, until a set of output files for each illumination angle of incidence is generated. Each file contains all the raw data extracted from each secondary reflector for a given illumination angle of incidence for a given azimuthal pixel width with their respective altitude angles. An averaging function then procedurally opens every file in order of angle of incidence and averages together the cell values for a user specified altitude angle range. For example, if the user specified an angular 'height' range of 1° altitude, and the azimuthal 'width' for each pixel in a row of pixels was 0.2° with 9 horizontal pixels averaged, the averaging function will compile and average 4 pixel-averaged data points at 0.25° altitude per data point together into one point representing a "box" of data. This box would cover an area with an altitude angular width of 1° and an azimuthal width of 1.8°. For the final data output, the altitude angle is converted to emission angle by $90 - altitude$, and is output to a single final data .xls and .csv file.

2.5 Standard Deviation

To quantify the stability of measurements taken with the goniometer, the standard deviation inside the aggregated pixel boxes was calculated using 100 data frames. To collect the data, a sample of Spectralon™ was placed in the aperture of the device, the sample was illuminated from the zenith, and 100 data frames were collected and saved. To reduce noise from the camera, another 100 frames were collected with the lens cap over the camera aperture and saved as background frames to be used for background subtraction when characterizing the standard deviation. With the required data collected, the background frames were averaged into a single master background frame, and was subtracted off of all 100 frames for the illuminated sample. The averaged background frames for the two configurations implemented are shown in figure 2.13, where the pixel values in the frame are amplified by a factor of 100 to clearly visualize the noise characteristics of the camera sensor [62].



Figure 2.13: *Two amplified background frames taken with the ZWO ASI662MC camera [45]. In both frames, some bright spots are seen that are likely small dust grains from when the camera was assembled. The 5 second exposure frame shows an even distribution of background noise, showing few of the fine-detail noise sources due to the high exposure time allowing charge to build up to due to electrical noise to spill into neighboring pixels. The 10 0.5 second exposures stacked show bright and dark vertical lines, these fine noise sources are visible because the short exposure time reduces the amount of charge due to noise that spills over into neighboring pixels [62].*

The data extraction and data averaging functions were run on all 100 of the background subtracted frames

producing 100 .xls and .csv files for each frame containing averaged Analog-to-Digital Unit (ADU) values for each one of the aggregated pixels boxes. To calculate the standard deviation, the data from these files was loaded and the numpy standard deviation and mean functions were applied to produce .xls files, one file containing the standard deviation, and one file containing the mean, for each pixel box across all 100 frames. The equation for the standard deviation used by the numpy function with the relevant variables applied is described by equation 2.1 [63].

$$\sigma_{pixel\ box} = \sqrt{\frac{\Sigma_i |I_{i,\ pixel\ box} - \bar{I}_{pixel\ box}|^2}{N}} \tag{2.1}$$

Where I is the intensity of the signal of the averaged aggregate pixel box reported in ADU, and N is the number of frames. The standard deviation was measured for two device configurations, one collecting single 5 second camera exposure data frames, and one where each data frame is collected by stacking 10 0.5 second exposures together. The mean and standard deviation results for each secondary reflector are plotted separately in figures 2.14 and 2.15. The standard deviation and mean results for the scattering plane are plotted alongside each other in figure 2.16.

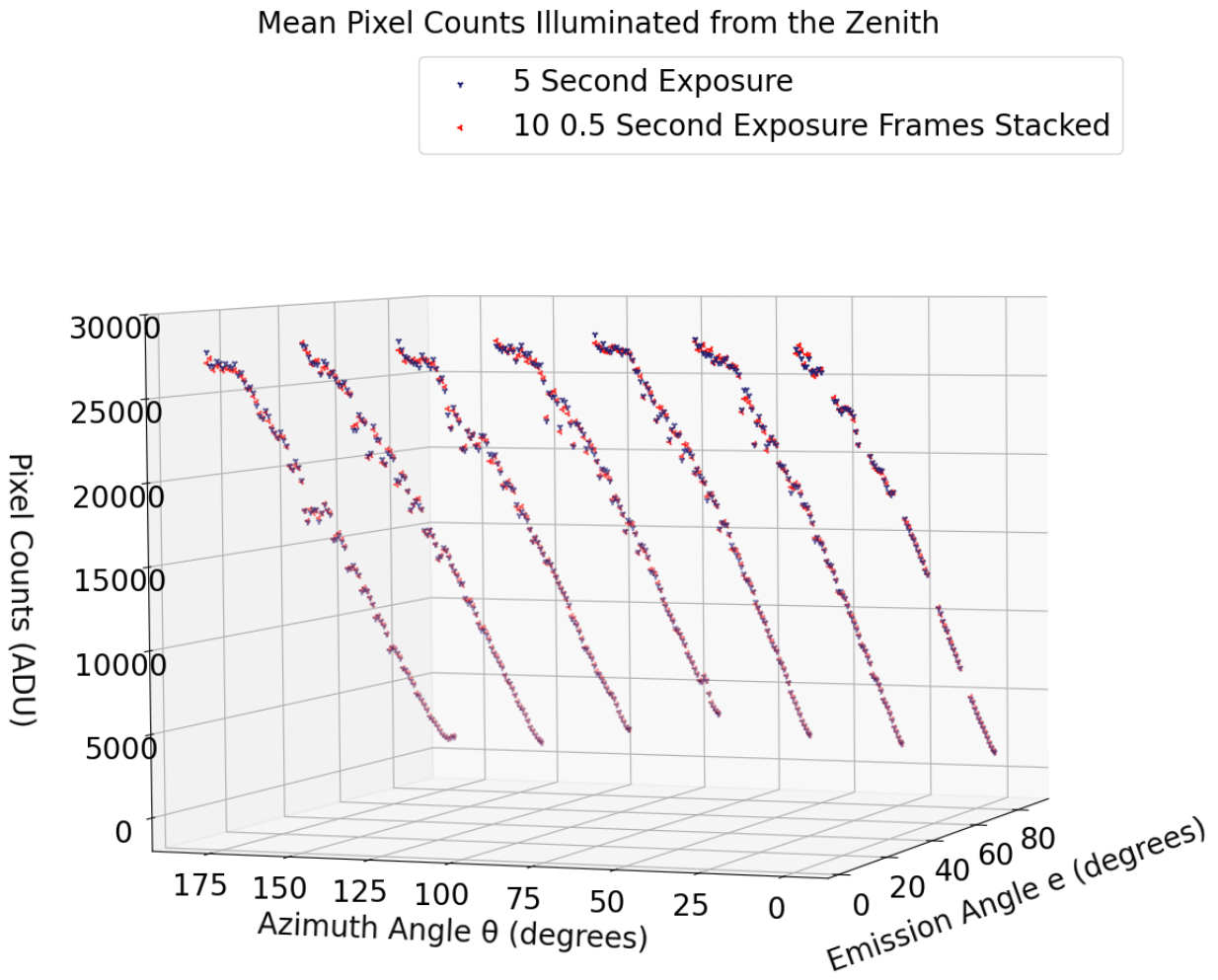

Figure 2.14: *3D plot of the mean from 100 data frames captured for each configuration tested, the single 5 second exposure frame and 10 0.5 second exposure frames stacked configurations. The emission angle and azimuth are on the x and y axis, and the average ADU value for the pixel box is on the z axis. The mean at each azimuth is clearly visible, with consistent results across each secondary reflector.*

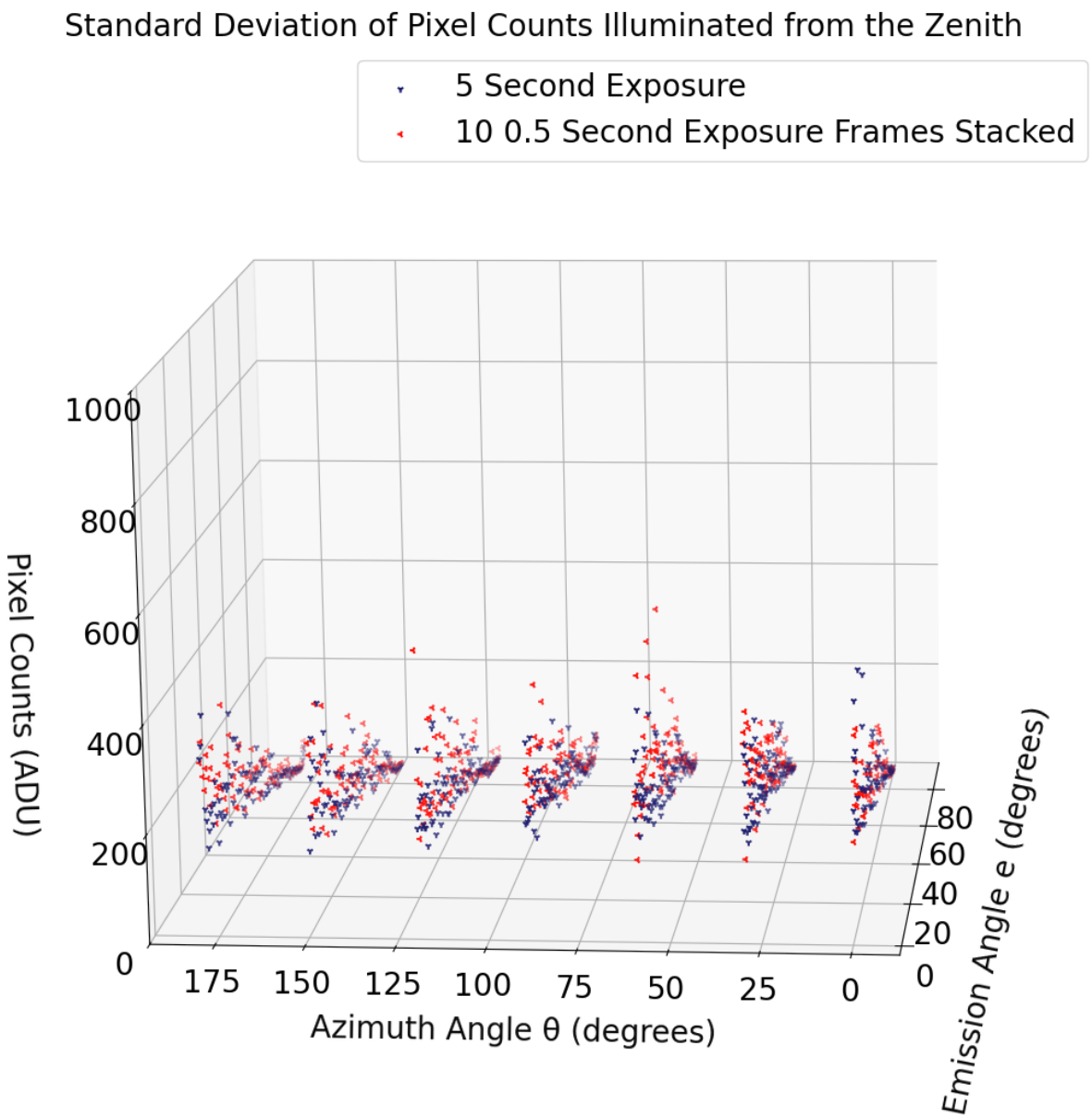

Figure 2.15: *3D plot of the standard deviation from 100 data frames captured for each configuration tested, the single 5 second exposure frame and 10 0.5 second exposure frames stacked configurations. The emission angle and azimuth are on the x and y axis, and the standard deviation of the average ADU value for the pixel box is on the z axis. The standard deviation at each azimuth shows similar results across all secondary reflectors.*

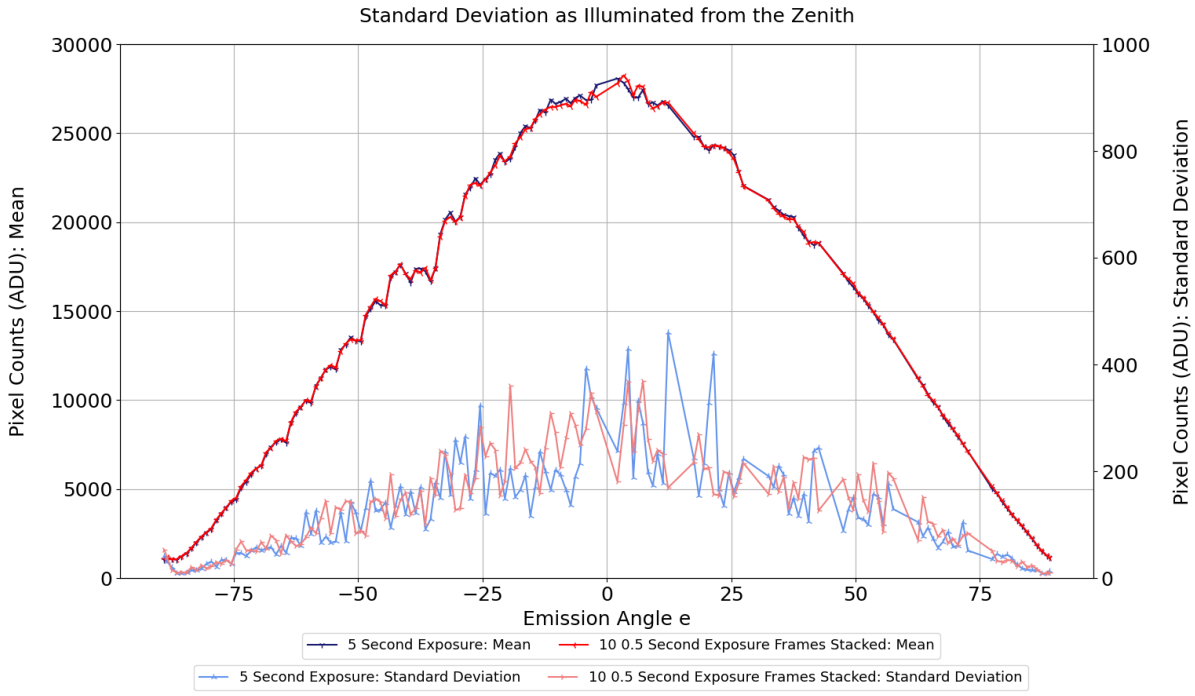

Figure 2.16: *The standard deviation compared to the mean of the two secondary reflectors corresponding to the scattering plane of the goniometer using both the single 5 second camera exposure and 10 0.5 second exposure frames stacked configurations. The left y axis on the twin y axis plot represents the plot of the mean, and the right y axis represents the standard deviation. The jagged sections of the plot are due to slight variations in the surface of the paint on the secondary reflectors, these are not visible in reflectance plots because they divide out when images are divided for REFF calculation.*

Results show standard deviation values in the range of ~ 9 ADU to ~ 520ADU with mean values in the range of ~ 854 ADU to ~ 28449 ADU for the 5 second single frame exposure configuration. For the 10 stacked 0.5 second frames configuration, the standard deviation and mean ranges are ~ 7 ADU to ~ 459 ADU, and ~ 845 ADU to ~ 28843 ADU respectively. The "jagged" variations in the mean pixel count values arise from small surface irregularities in the paint coating applied to the secondary reflectors. These variations ultimately divide out during the REFF calculation process when the image frames are normalized through division.

The results discussed represent standard deviations around 1-2% of the respective mean for each data point, with outliers around 2-5% when data is collected near 90° emission angles, particularly when examining the standard deviation opposite the direction of incidence. This is supported with figures 2.17 and 2.18 where the standard deviation is represented as a percent of the mean.

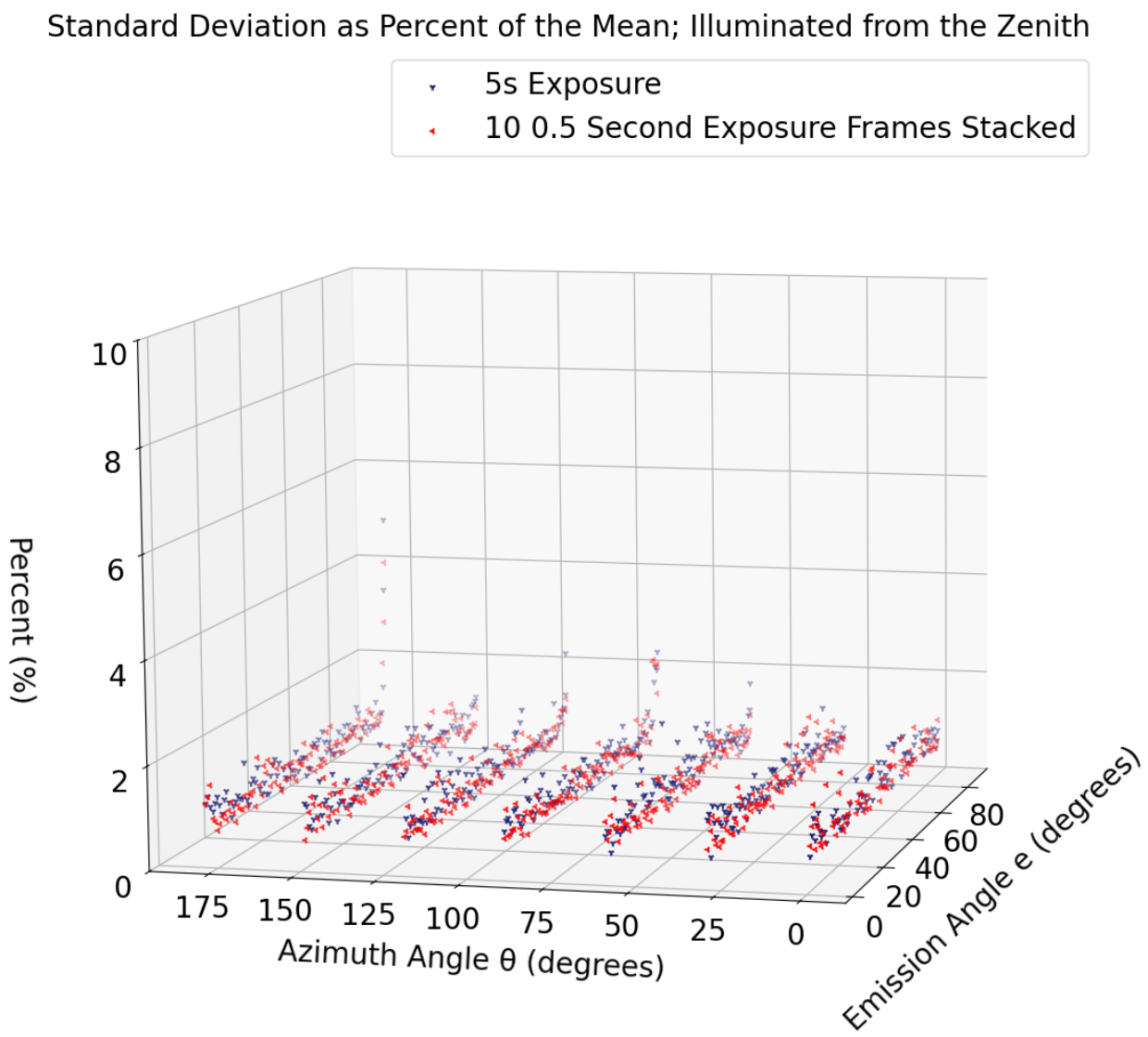

Figure 2.17: *The standard deviation for each pixel box represented as a percent of the mean for each secondary reflector. Results show that the standard deviation is consistently around 1-2% with occasional outliers at high emission angles in the 2-5% range.*

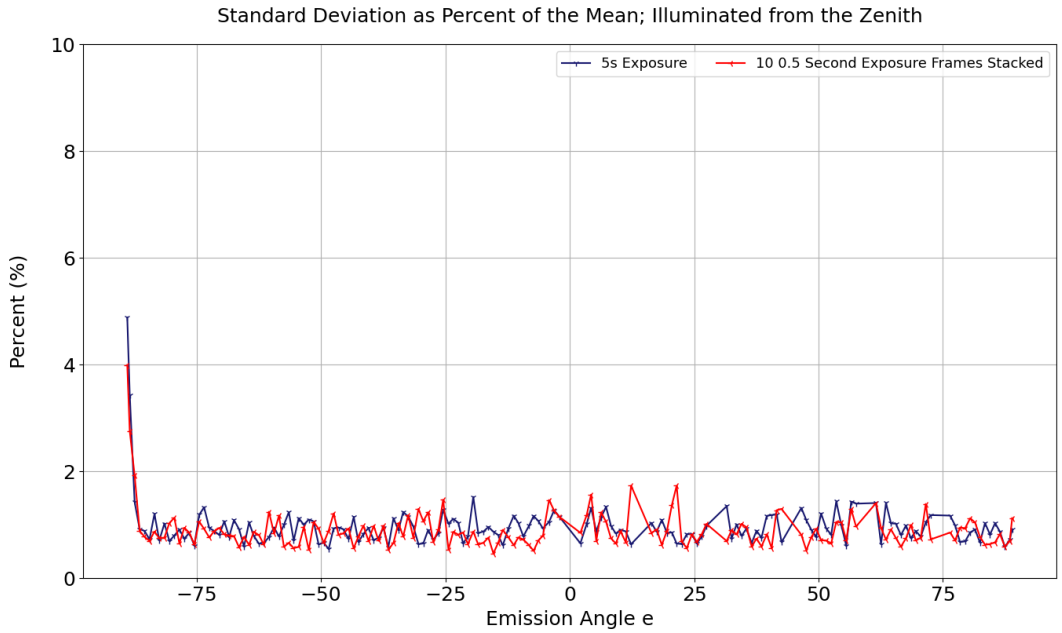

Figure 2.18: *The standard deviation for each pixel box represented as a percent of the mean in the scattering plane of the device. Results show that the standard deviation is consistently around 1-2% with outliers in the 2-5% range at high emission angles opposite the direction of incident radiation.*

The standard deviation results for both the single 5 second exposure and the stacked configuration of 10 0.5 s exposures show consistently low values, on the order of 1–2%, supported by figures 2.17 and 2.18. Figures 2.15 and 2.16 demonstrate consistent standard deviations across all secondary reflectors. Together, these results indicate that the goniometer is operating reliably and produces low-noise measurements.

2.6 Validation

2.6.1 Camera Linearity Testing

To ensure accurate device performance, the camera must provide a linearly proportional pixel response to changing light levels incident on the camera sensor [69, 70]. A camera sensor of linear response will report pixel counts representing an intensity directly proportional to the intensity of the source as described by equation 2.2.

$$I_{pixel} \propto I_{source} \tag{2.2}$$

The camera response linearity was tested directly by slowly increasing the output of a Marktech Optoelectronics MTE5270N 527nm LED [71] through a 60 mm, 115 mm back focal length plano-convex lens at a distance of 190 mm. The beam from the lens was directed toward a glass beam splitter at a distance of 190 mm, splitting off into a model 818-SL photodiode connected to a Newport 1830-C optical power meter [66, 67], and onto a paper diffuser viewed by the ZWO ASI662MC camera [45]. The photodiode connected to the optical power meter exhibits an absolute spectral responsivity of 3 mA/W [67]. The testing setup is shown in figure 2.19, the testing results are shown in figures 2.20 and 2.21.

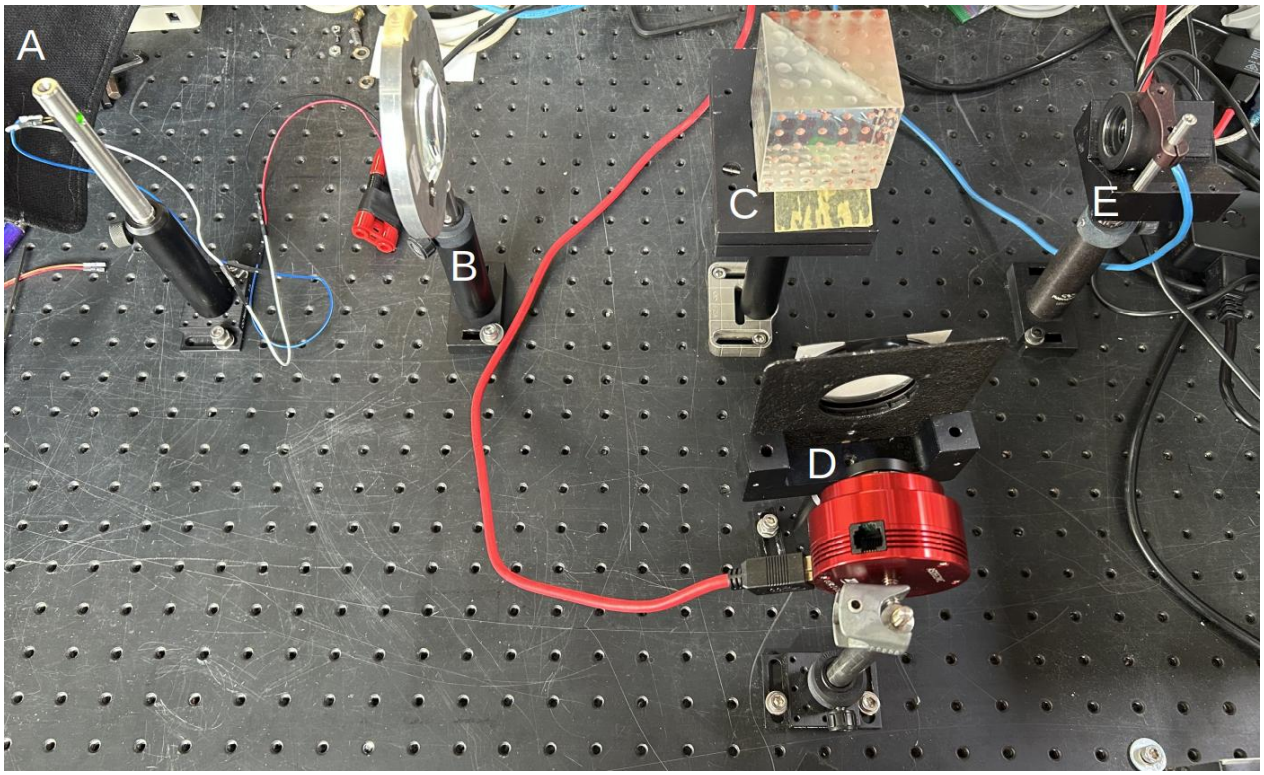

Figure 2.19: *The optics bench setup used when testing the camera linearity. A) is a Marktech Optoelectronics MTE5270N 527nm LED [71] mounted inside a hole in optics bench hardware. B) is a 60 mm, 115 mm back focal length plano-convex lens. C) is a beam splitter used to split the beam from the LED though the lens. D) is a ZWO ASI662MC camera [45] and a paper light diffuser. E) is the model 818-SL photodiode feeding into a Newport 1830-C optical power meter [66, 67]. The distance from A) to B) is 190 mm, from B) to the center of the beam splitter C) is 190 mm, and the distance from the center of C) to E) and D) is 150 mm.*

Figure 2.20 shows excellent linearity performance for the 5 second single exposure configuration, with an optical power range of 0.1 μW to 3.6 μW directly proportional to an ADU count of 1500 up to the pixel

saturation value of 65535 ADU. A minor deviation from a near perfect 1:1 ratio is seen around an optical power 0.6 μW and pixel values of 11000 ADU. When comparing the output voltage to the LED to the optical power and the camera ADU counts directly, the twin y-axis plots almost perfectly superimpose each other with a minor deviation around 2.27 V, showing a linear relation between power output from the LED and pixel response.

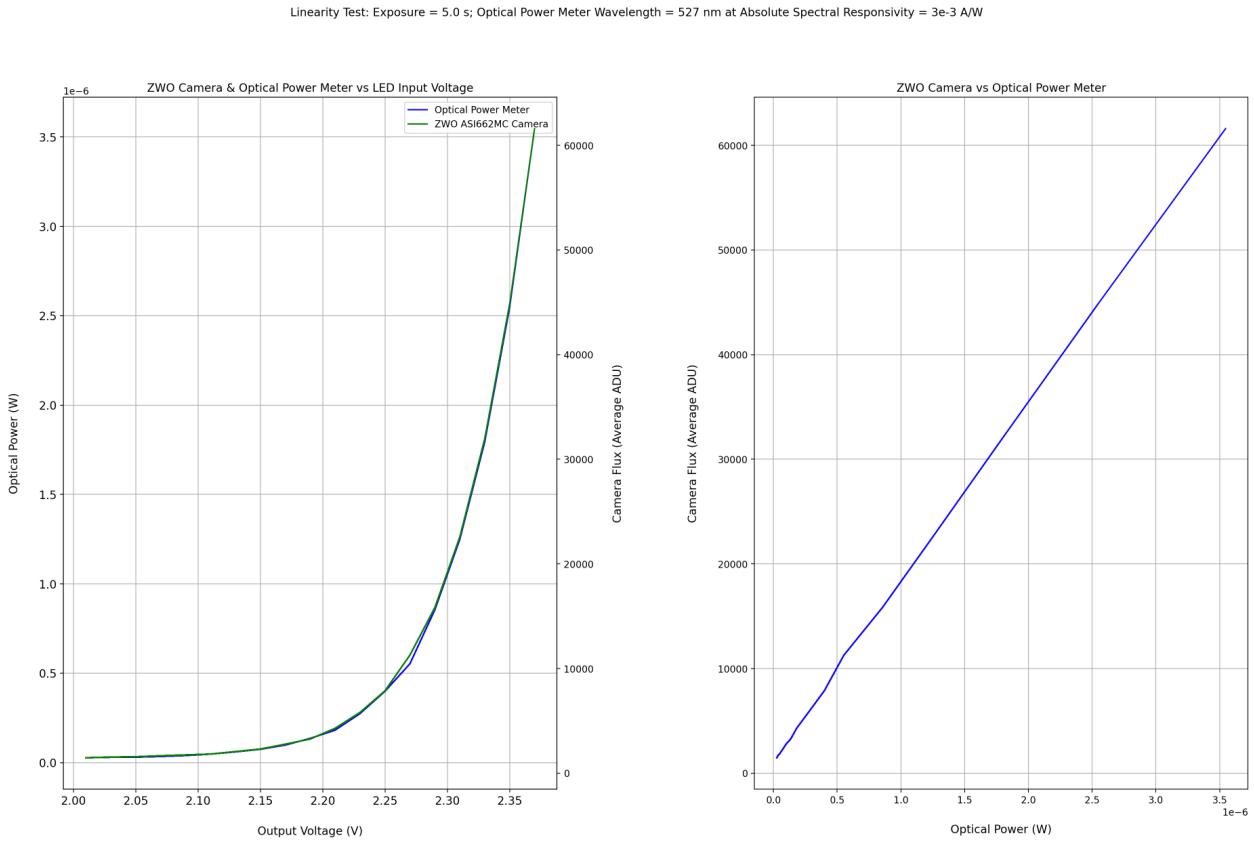

Figure 2.20: *The linearity results (right) for the 5 second single exposure linearity test showed highly linear results with very minor fluctuations from a perfect 1:1 proportionality. The dual y-axis plot (left) comparing the output voltage to the LED to both the optical power and the camera response show nearly superimposed results, supporting the linear performance of the camera.*

Figure 2.21 shows the linearity of the camera configuration stacking 10 0.5 second exposure frames. The improvement over figure 2.20 is clearly visible, showing a near-perfect linear response, capable of a linear response for higher optical power values up to 25 μW at an LED voltage of 2.8 V. When comparing the output voltage to the optical power and the pixel ADU, the two plots almost perfectly superimpose each other throughout the duration of the entire test.

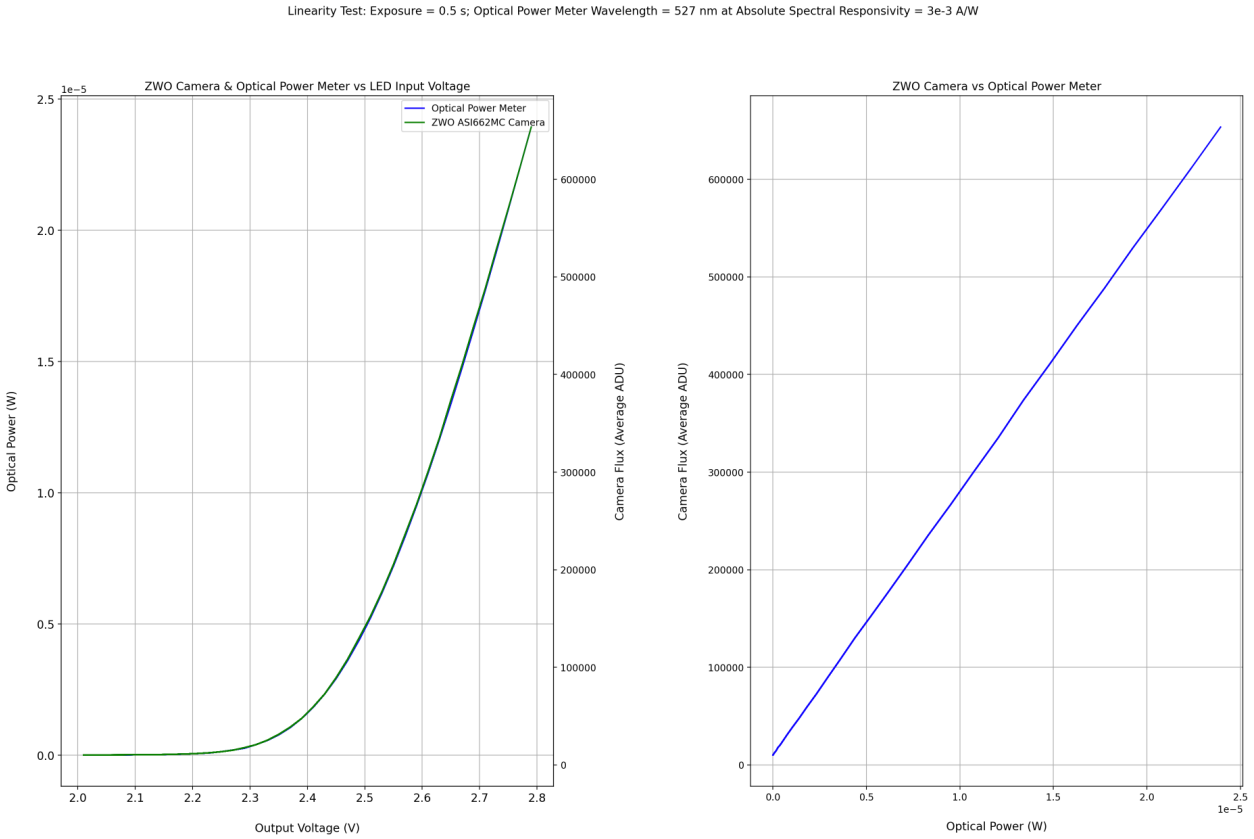

Figure 2.21: *The linearity results (right) for the 10 0.5 second exposure stacking show a near perfect 1:1 proportionality. Further supported by the dual y-axis plot (left) comparing LED output voltage to the optical power and camera response, the camera in the image stacking configuration responds proportionally identically to the changing light level.*

These results show excellent camera response linearity over almost the entire range of pixel values output from the 12-bit ADC of the camera mapped to a 16-bit output [45]. A minor gap in the pixel response is observed in the range of 0 to 1500 ADU, representing just the bottom 2.3% of the camera response range. The camera exhibits excellent linear response for all but the lowest light conditions.

2.6.2 Reflectance Standard Validation

To validate the performance of the goniometer, the device was set up to examine a Labsphere® Certified Reflectance Standards RSS-08-020 gray scale Spectralon™ kit. The eight Spectralon™ samples in the kit act as near-Lambertian scatterers covering known REFF values of 99%, 80%, 60%, 40%, 20%, 10%, 5%, and 2%, these standard samples are used to ensure accurate reflectance response from 0.99 REFF to 0.02 REFF. The results of this test, shown in figures 2.23 and 2.24, are reported as REFF for direct comparison with the expected values of the gray Spectralon™ kit. To perform the test, the goniometer was set up on

an optics bench, elevating the Spectralon™ sample into the aperture of the goniometer. With the sample in place, a large box with the interior painted black was placed over the goniometer to eliminate external light. After the box is placed overtop, data is collected, the box is removed, and the sample is exchanged procedurally decreasing in brightness with every step until the full set of 8 samples are examined. The setup used without the black box is shown in figure 2.22 with the zenith laser turned on to ensure the sample is correctly centered in the device aperture.

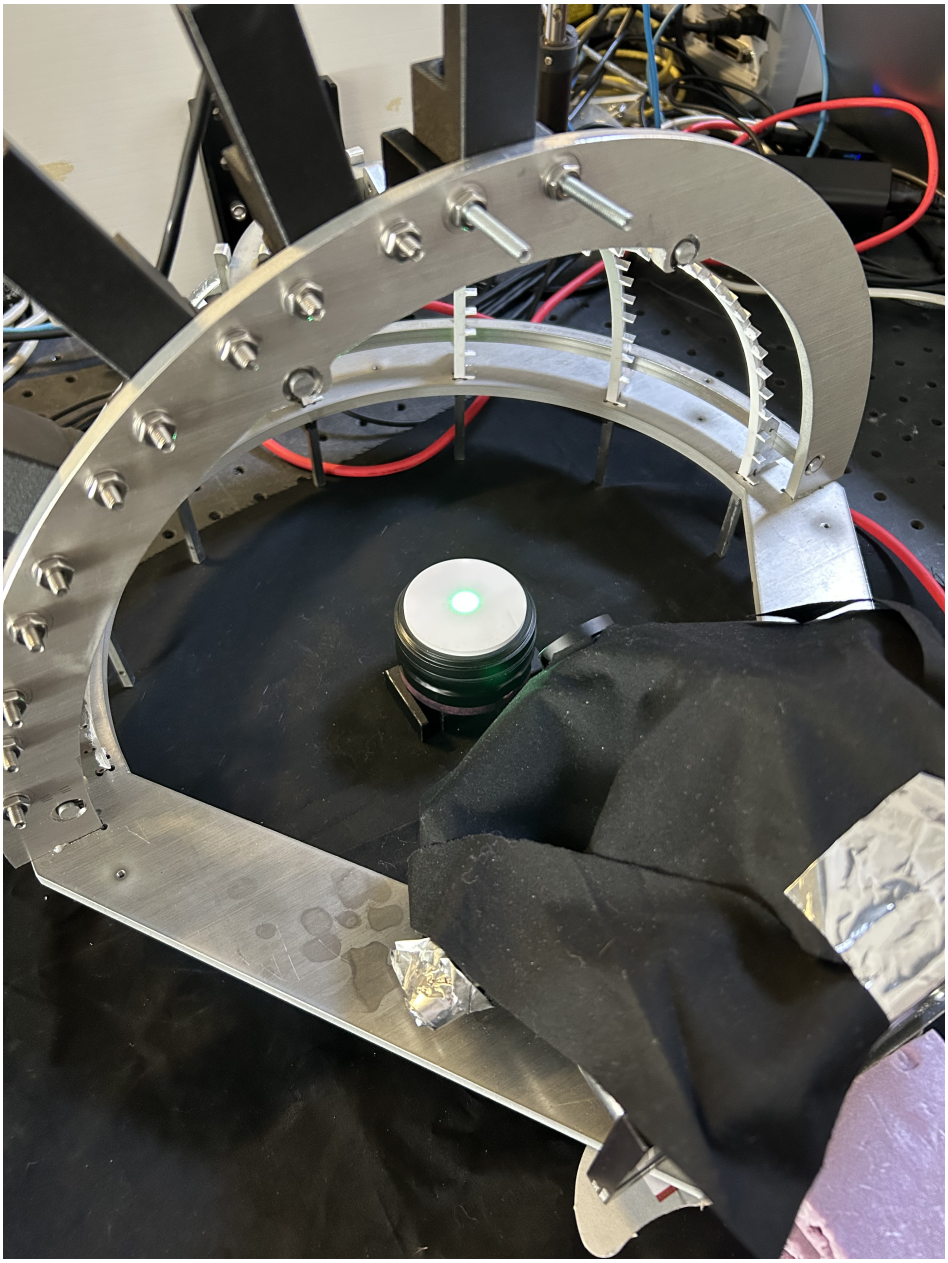

Figure 2.22: *The Goniometer viewing an SRS-99-020 sample during testing against gray Spectralon samples. Gray Spectralon is used as a calibration sample to ensure the reported reflectance values are within expected ranges [10, 8, 15].*

Examining figures 2.23 and 2.24, the diffuse reflectance standard testing results are very similar between the single 5 second exposure frame and the 10 stacked 0.5 second exposure frames. The results from the two configurations show some reflectance deviation from perfectly Lambertian scattering behavior. This behavior is expected with these samples, and is supported by the increase in reflectance at high emission angles in the standards with less than 99% expected REFF [11, 10, 9, 8, 7]. As the angle of incidence increases the emergence of forward scattering behavior is observed. An artifact due to high forward scattering seen at the 75° incidence angle is seen as dips in REFF opposite the incident beam. This is due to higher forward scattering in the SRS-99-020 sample than the SRS-80-020, SRS-60-020, SRS-40-020, SRS-30-020, and SRS-10-020 samples when illuminated at a high angle of incidence. When the gray samples are compared to SRS-99-020, their lower forward scattering values show up as dips in the REFF. At emission angles approaching 90°, a sharp drop in reflectance is observed. This is believed to be a result of the poor pixel response at extremely low light levels seen in the linearity results in section 2.6.1. The decreasing reflectance, approximately following equation 1.19 [12], results in low observable light levels at these high emission angles. This effect is more significant in the 10 stacked 0.5 second exposure frame configuration shown in figure 2.24, correlated to lower ADU values as a result of shorter exposure time.

To denoise the data, a gaussian blur filter is applied using the SciPy python library [68] to reduce noise in the data frame files. The data is then extracted using the data extraction algorithm, and the final data output has a moving average applied to it using the pandas python library [72]. This denoised data is compared to the data extracted from images without a gaussian blur filter or a moving average. The difference between the denoised data and the raw data is plotted as residuals shown as the shaded error as part of the reflectance plots in figures 2.23 and 2.24.

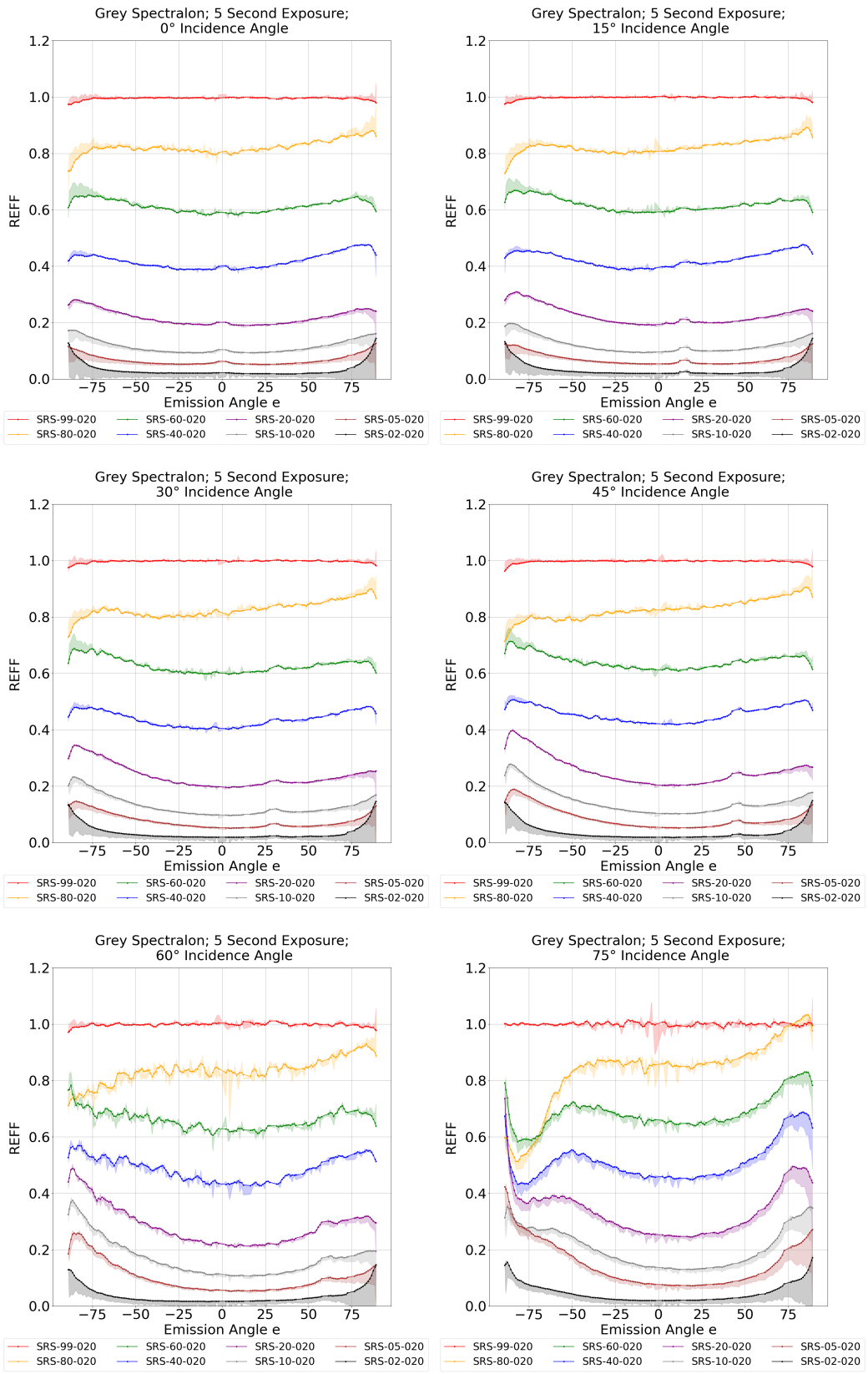

Figure 2.23: *The range of Spectralon diffuse reflectance standards tested using single 5 second exposure frames. The results align with expected results based on their data sheet [15].*

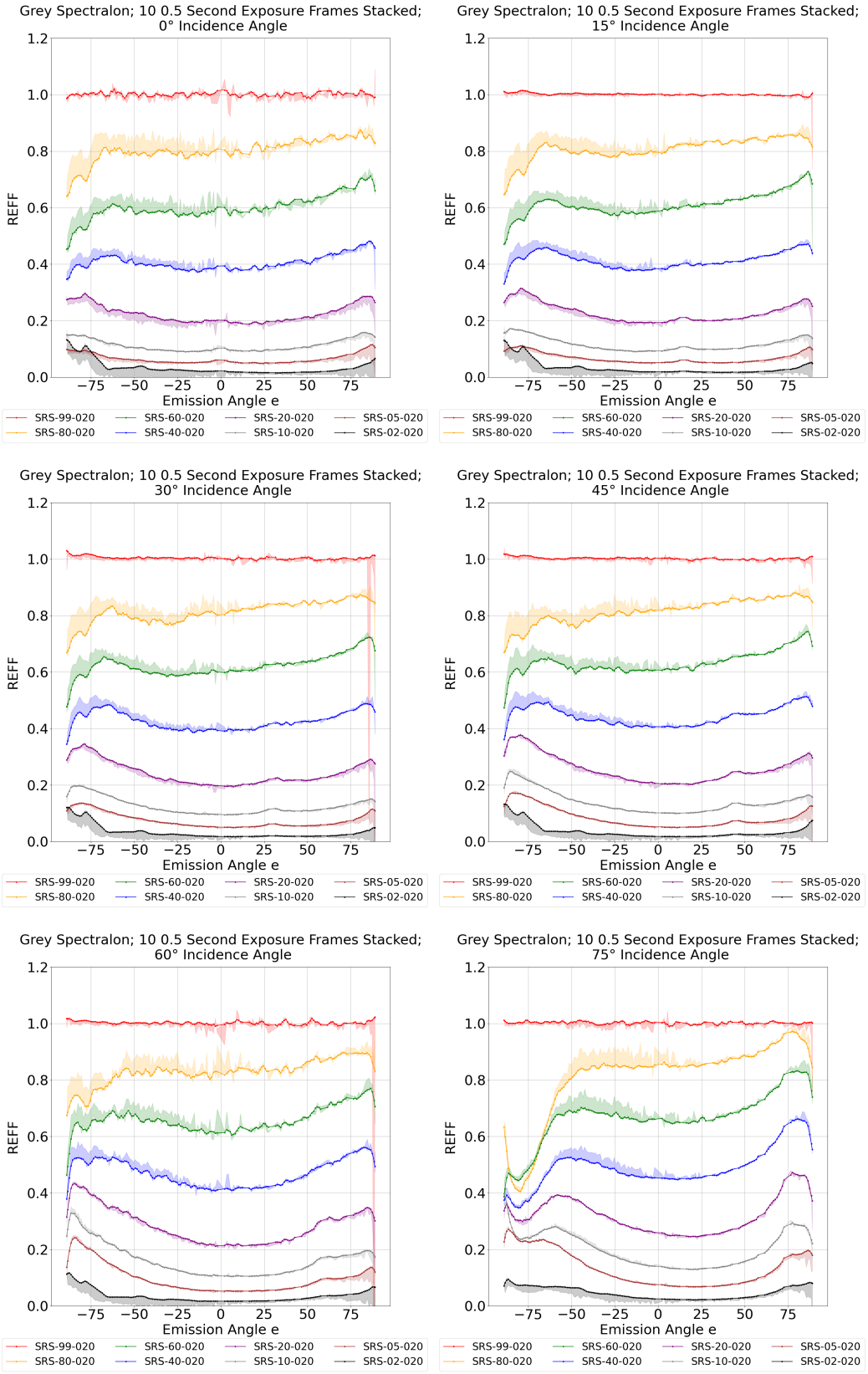

Figure 2.24: *The range of Spectralon diffuse reflectance standards tested stacking 10 0.5 second exposure frames. The results agree with the expected values from their data sheet [15].*

The raw ADU counts extracted from data frames before dividing by the 99% reflectance sample are shown in figures 2.25 and 2.26. The "jagged" variations in the pixel count values are from surface irregularities in the paint applied to the secondary reflectors that divide out during REFF calculation. The measured intensity represented as ADU follows the expected behavior of a near-Lambertian scatterer across the full range of reflectance standard samples [12]. As the incidence angle increases, slight asymmetries in the intensity distributions are observed as forward scattering emerges as a result of the imperfect Lambertian scattering properties of Spectralon™ [11, 10, 9, 8, 7]. Evolving into clear forward scattering lobes at the 75° incidence angle, with the strongest forward scattering lobe observed in the 75° incidence angle, causing the dips observable in the 75° angle of incidence reflectance plots in figures 2.23 and 2.24.

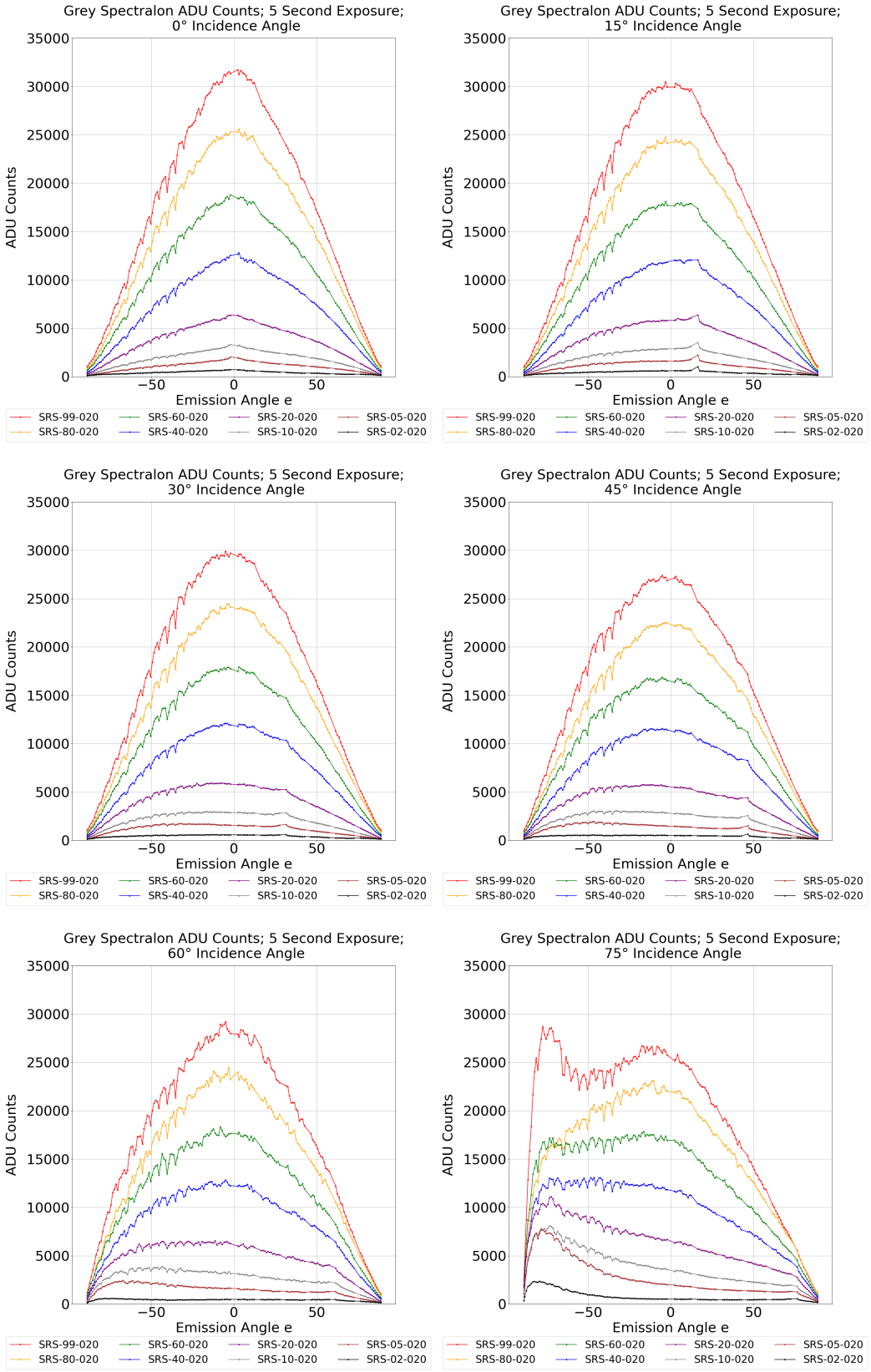

Figure 2.25: *Raw ADU count results of the Spectralon diffuse reflectance standards using single 5 second exposure frames. The 'jagged' variations in the data are due to slight irregularities in the surface of the paint on the secondary reflectors that divide out during REFF calculation.*

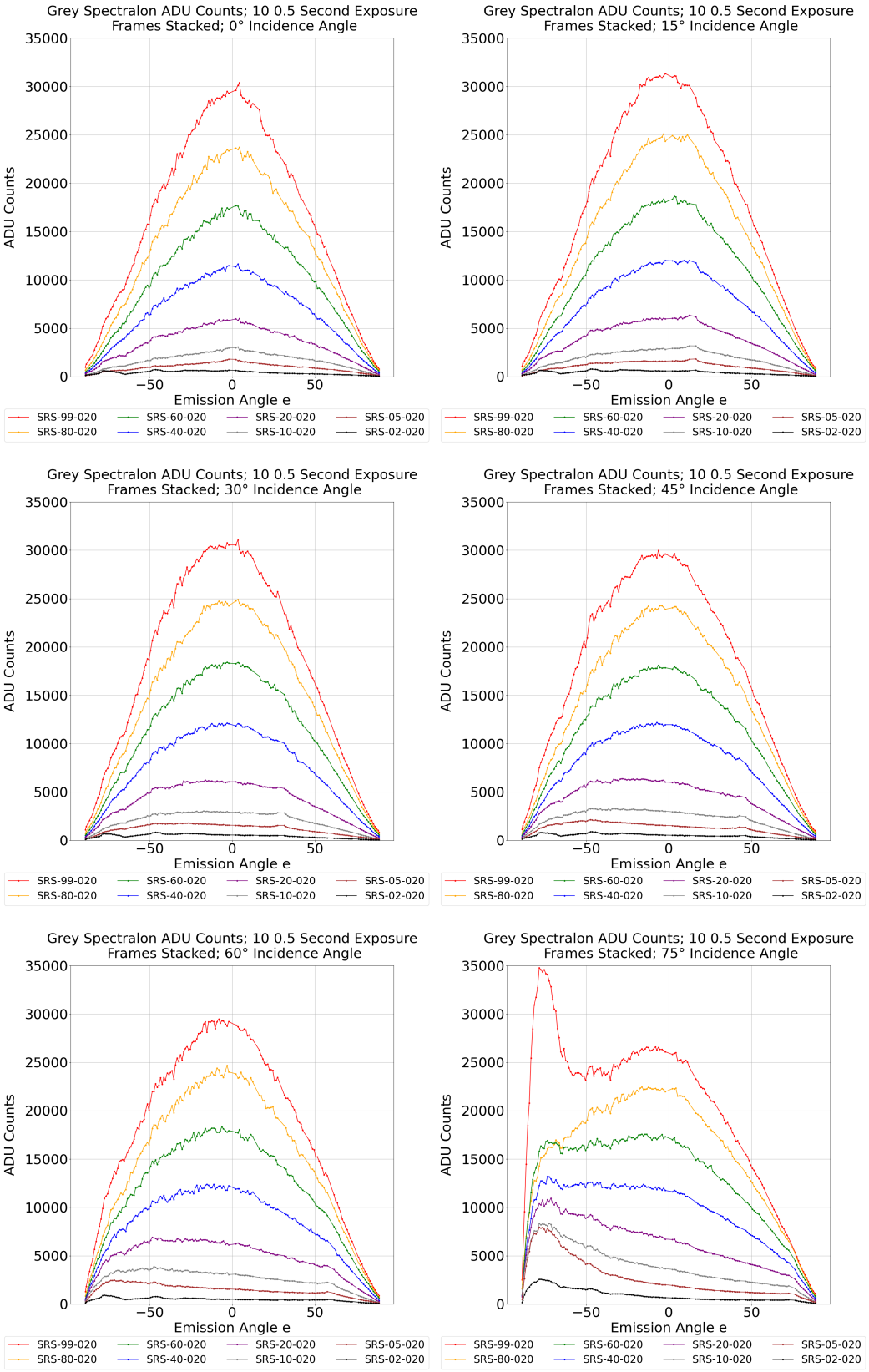

Figure 2.26: *Raw ADU count results of the Spectralon diffuse reflectance standards stacking 10 0.5 second exposure frames. The 'jagged' variations in the data are due to slight irregularities in the surface of the paint on the secondary reflectors that divide out during REFF calculation.*

To further validate the performance of the device using the gray Spectralon™ kit, the collected data was used to approximate the directional-hemispherical reflectance [38]. To do this, the data discussed in figure 2.24 from the 10 0.5 second frame stacking configuration was used to approximate a full hemisphere of REFF data. It is assumed that the REFF values of the diffuse near-Lambertian gray Spectralon™ samples at azimuth values of 210°, 240°, 270°, 300°, and 330°, are equivalent to the REFF values at azimuths of 150°, 120°, 90°, 60°, and 30° [12, 15, 10, 8]. This assumption was used to interpolate a full hemisphere of data with a resolution of 90 by 360 points on the emission and azimuth angle axes, respectively. The interpolation was performed by feeding the REFF data into a nearest neighbor interpolation algorithm, which was then fed into a minimum curvature interpolation algorithm [68]. Data at each point from the interpolation was associated with a projected solid angle on the hemisphere and summed to obtain the total directional-hemispherical reflectance $\rho_{hemisphere}$ for each data point k following the summation form of the directional-hemispherical reflectance equation [38, 4].

$$\rho_{hemisphere} = \sum_{k} \frac{REFF_k}{\pi} cos(e_k) sin(e_k) de_k d\psi_k \tag{2.3}$$

The results for each gray Spectralon™ sample at every incidence angle following equation 2.3 are shown in figure 2.27.

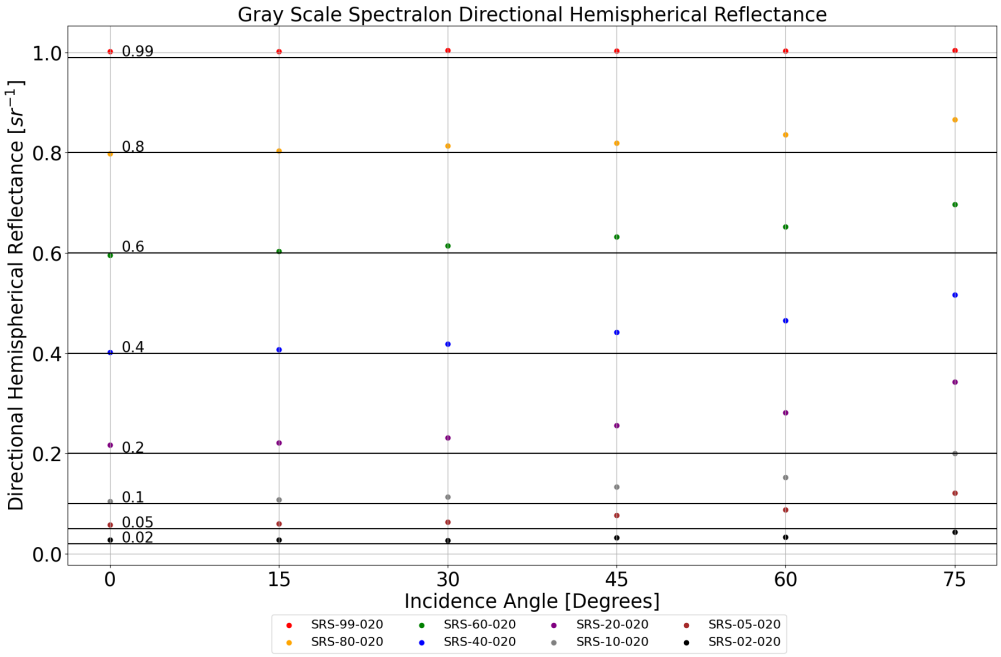

Figure 2.27: *Directional-hemispherical reflectance of Labsphere® Certified Reflectance Standards RSS-08-020 at all angles of incidence. At small angles of incidence in the range of 0° to 30°, reflectance values deviate from their expected values by approximately 0.5% to 3.5%, with larger deviations at angles of incidence above 30°.*

The Labsphere® Certified Reflectance Standards from the RSS-08-020 gray scale Spectralon™ kit produced expected reflectance results. Testing yielded typical values aligning with the expected REFF and $\rho_{hemisphere}$ values for each sample [15], with expected deviations from perfect Lambertian scattering behavior [11, 10, 9, 8, 7, 12].

2.6.3 Specular Reflection Testing Using a Mirror

To verify the specular performance of the goniometer, a mirror was placed in the device aperture as shown in figure 2.28. The mirror used is a small polished aluminum mirror found in the lab, elevated into the goniometer aperture using optics table parts. As with the gray scale Spectralon™ test, the goniometer was set up on the optics table, and covered with a box that had the interior painted black to prevent external light sources from affecting the results.

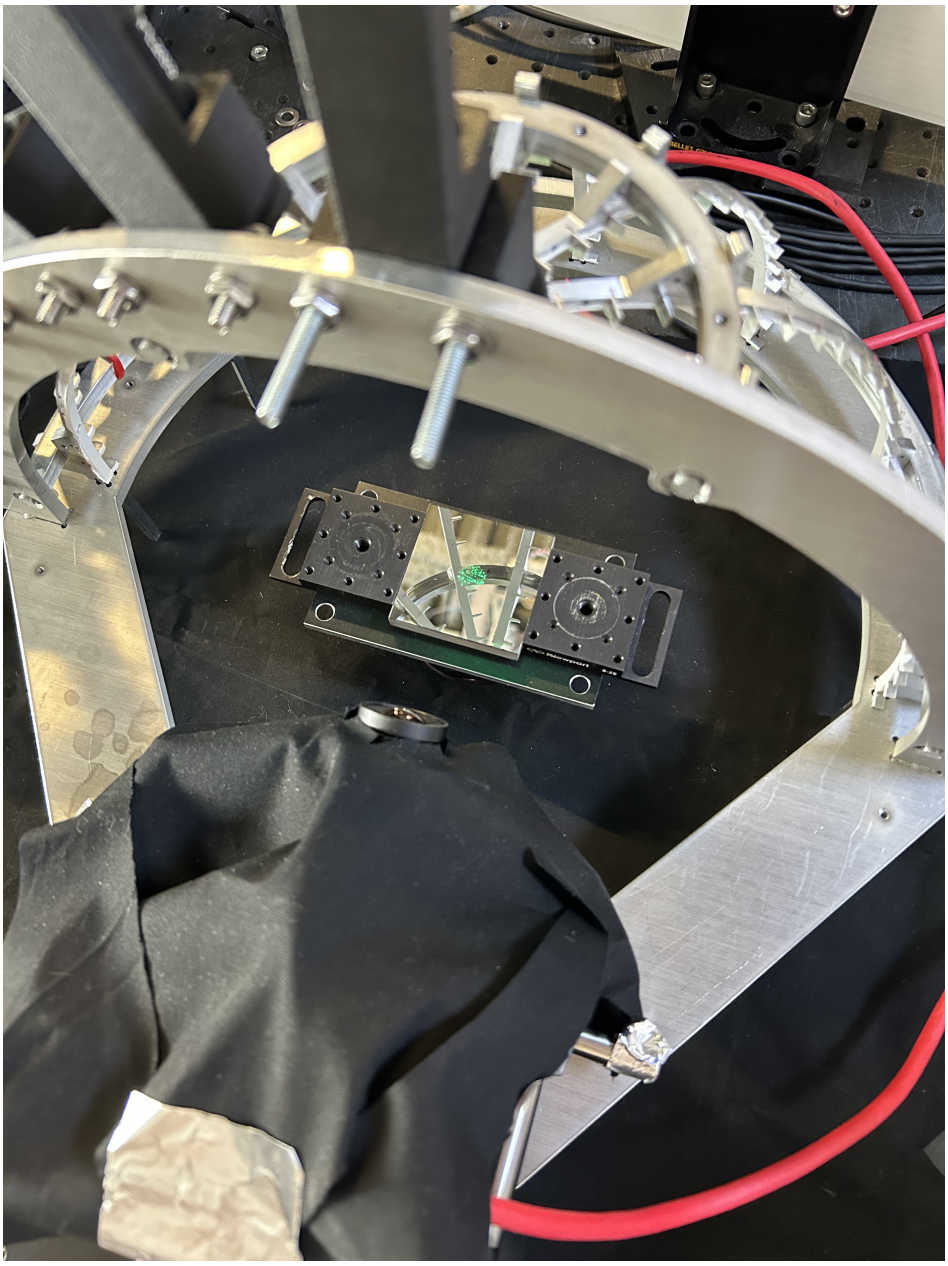

Figure 2.28: *The goniometer viewing the mirror used to test specular reflection performance. The mirror is being held in place and elevated to be level with the measurement plane of the device.*

Mirror testing was performed using a specific configuration to avoid pixel saturation due to the intensity of reflected radiation from the mirror. The configuration stacked 500 exposures at 0.01 seconds per exposure, maintaining pixel ADU counts below the 16-bit saturation cutoff value of 65535. In this test, the lasers had not been aligned with respect to the polarization planes of the laser diode; however, the polished metallic surface of the aluminum mirror minimizes the polarization-dependent effects arising from Fresnel interactions [4]. The raw ADU count results from the mirror test are shown in figure 2.29. Specular reflections are

observed at angles of emergence equivalent to the associated angles of incidence.

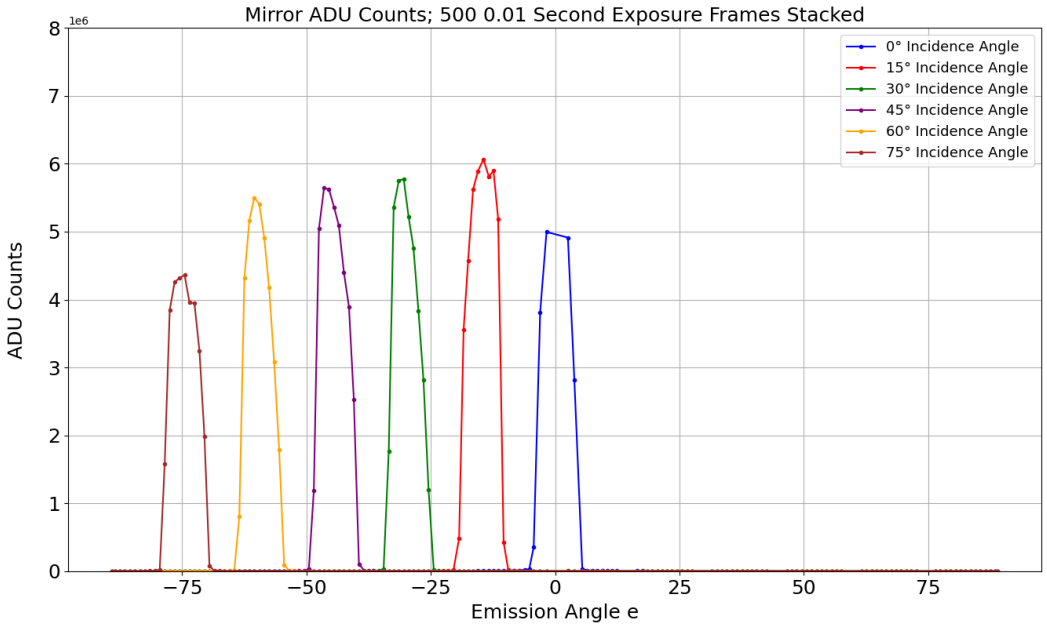

Figure 2.29: *ADU count results from examining a mirror with the goniometer. The specular reflections are observed at emission angles equivalent to the incidence angles of the light sources.*

To maintain consistency with the reflectance performance validation results presented in this chapter, the mirror reflectance measurements are reported as REFF, as shown in figure 2.30. The results exhibit the same intense specular peaks at emission angles corresponding to the angles of incidence. The measured REFF of the peaks increased with the incidence angle with the exception of the 75° incidence angle. This outlier in the results is due to the forward scattering lobe observed when Spectralon™ is illuminated at high incidence angles, causing the intensity of the 75° incidence peak to be divided by a high value that is uncharacteristic of a Lambertian scatterer [12, 4, 11, 10, 9, 8, 7]. The increasing REFF values in the rest of the peaks are due to the way that radiation emitted by an illuminated Lambertian scatterer decreases with emission angle, as shown in figure 1.2 and described by equation 1.19 from section 1.1.3 [12, 4]. When a sample exhibiting specular reflecting behavior is divided by a Lambertian, the resulting ratio of the sample compared to the Lambertian causes the REFF to increase proportionally [4].

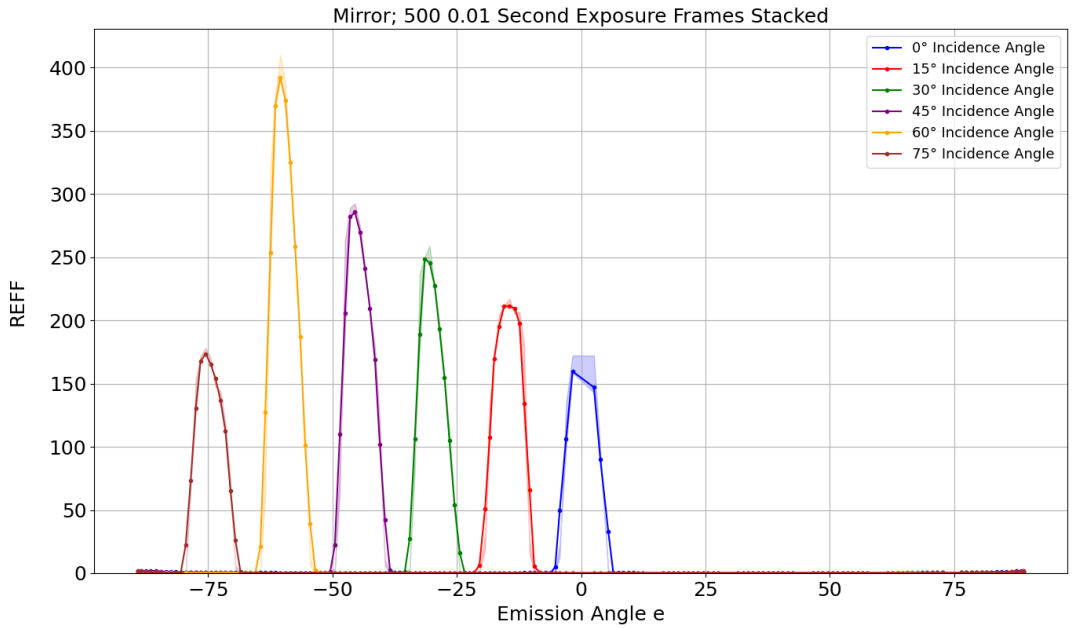

Figure 2.30: *REFF results from the mirror test; intense peaks are observed at emission angles equivalent to the incidence angles. The REFF values increase as the incidence angle increases, with the exception of the 75° incidence angle. These REFF values are a direct result of comparing a sample with strong specular behavior to Spectralon™, a known near-Lambertian scatterer [12, 4, 11, 10, 9, 8, 7].*

The results of testing the ability of the goniometer to measure specular reflections showed the expected behavior across all experiments, with both ADU and REFF results exhibiting peaks at emission angles corresponding to the incident light sources. REFF results attributable to the intrinsic scattering properties of Spectralon™ [11, 10, 9, 8, 7] are also evident and are consistent with expectations given the systematic characteristics of the experimental configuration.

Chapter 3

Evolving CO_2 Ice Experiments Using The MARVIN Chamber

Experimental goniometry research on evolving Martian polar CO_2 ice analogs enables further understanding of the nature of light scattering from illuminated dynamic CO_2 ice on the Martian surface, building stronger interpretations of orbital and remote sensing reflectance observations of Mars. These measurements, particularly during active morphological evolution of the CO_2 ice sample, help constrain seasonal atmospheric transport and thermal evolution processes in the context of evolving Martian climates [2, 35, 22, 36, 34, 3, 26, 25, 30, 20, 31, 21, 23, 24]. Measurements of Mars analog CO_2 ice have previously been performed using the MARVIN chamber at York University [1] by Isen and Smith in their 2024 publication [2]. However, those measurements were limited in their ability to capture the reflective properties of actively evolving CO_2 ice. The experiments presented in this chapter aim to address this limitation through the examination of dynamically evolving Mars analog CO_2 ice samples.

With nominal device performance verified, two CO_2 ice samples mimicking the distinct morphologies discussed in Isen & Smith 2024 [2] were examined using the MARVIN chamber [1]. The first sample morphology discussed in section 3.2.1, is a frosty ice sample known to exhibit largely diffuse scattering properties [2]. This morphology is observed in the low temperature regions of the Martian south polar seasonal cap shown in figure 1.6, regions 1, 2, 3, and 4. The second sample morphology discussed in section 3.2.2, is a transparent slab ice known to exhibit strong specular reflections [2], believed to be observed in the 'cryptic' region 0 of figure 1.6 of the Martian south polar seasonal cap. In this region, local temperatures are

higher, and a region of transparent CO_2 ice is observed. In the transparent slab ice experiment, the sample is further evolved from a specularly reflecting transparent slab ice to a diffusely reflecting frosty ice [2], demonstrating a powerful use case of the rapid data collection capabilities of integrated goniometry.

3.1 Methods

At the beginning of each experiment, the chamber is pumped down from atmosphere to 1.5 mbar, purged with 80 mbar of CO_2 to remove water that can contaminate the sample, and pumped down again to 0.5 mbar. With the camber under 0.5 mbar of pressure, the cold plate is cooled and held at the desired temperature using pulses of pressurized liquid nitrogen. With the cold plate at the desired temperature, gaseous CO_2 is introduced into the chamber and held at a desired CO_2 ice deposition pressure. Upon initiation of these conditions, CO_2 ice deposition onto the cold plate takes place until a 0.5 cm sample is formed. Thickness of the ice is monitored using a d4 die placed on the cold plate, as seen in figure 3.1. The top of the bottom number, the number 4, on the d4 is equivalent to 0.5 cm from the plane of the cold plate, providing an ice thickness reference during deposition. Data describing the conditions inside the chamber is output to a .log file and is saved to the local computer.

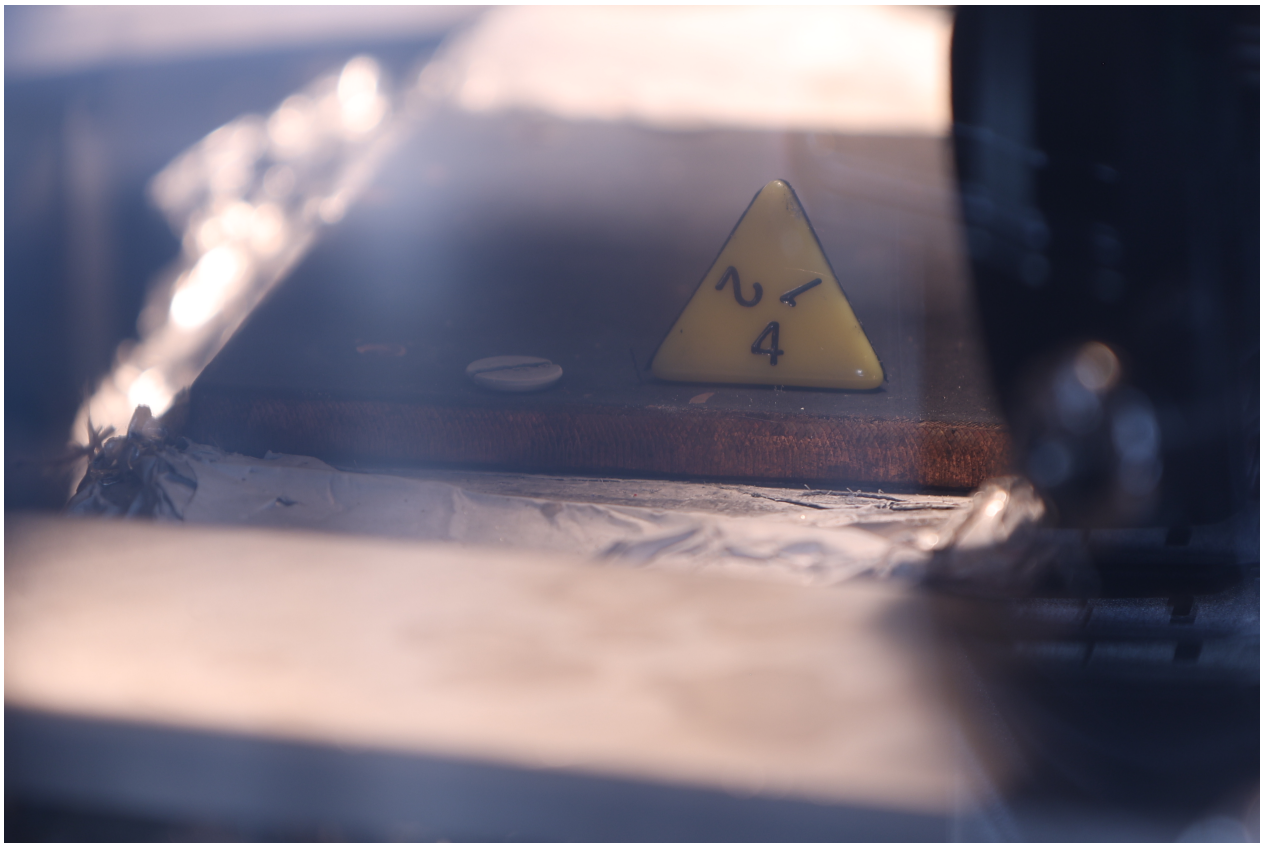

Figure 3.1: *The d4 die on the cold plate is used to monitor the thickness of the ice as it grows. When the ice covered the bottom number of the d4, the sample is approximately 0.5 cm thick.*

Immediately after the sample reaches the desired thickness of 0.5 cm, an initial measurement with the goniometer is taken. Measurements are performed using the 10 0.5 second exposure frame stacking configuration, discussed in chapter 2, for its ability to capture a wide range of brightness levels, and potential BRDF values. The goniometer examines the sample at six angles of incidence, starting at 0° from the zenith, increasing in 15° increments from the zenith until reaching a final incidence angle of 75°, taking approximately 45 seconds to cover all angles of incidence. The collected REFF data is converted to BRDF using equation 1.22 to facilitate comparison with the broader remote sensing literature. The data is plotted using the 2D scattering plane format and the interpolated heat map format for each angle of incidence. Following the initial measurement, the cold plate temperature is allowed to either increase or decrease steadily to initiate sample evolution. During sample evolution, additional measurements are taken with the goniometer to test the capability to examine evolving samples.

3.2 Results

3.2.1 Diffusely Scattering Frosty CO_2 Ice

In this experiment, a sample of CO_2 ice is grown with similar morphology to the frosty ice experiment discussed in figure 1.10 [2]. The sample shown in figure 3.2 is deposited onto the cold plate forming the desired morphology below 140 K in the range of Martian surface atmospheric pressures around 6-12 mbar, as suggested by the temperatures corresponding to ice morphologies in figure 1.6 [33, 32]. For the purpose of this experiment, a sample deposition temperature and pressure target of 120 K and 6.0 mbar of pure CO_2 were chosen, allowing for a fast deposition of diffusely scattering frosty CO_2 ice. Data from the chamber conditions is plotted in figures 3.3 and 3.4.



Figure 3.2: *Image of the frosty ice showing the rough crystalline surface structure, grown at 120 K and 6.0 mbar. The d4 die embedded in the ice acts as a reference size scale, where the ice covering the bottom number of the die corresponds to an approximate ice thickness of 0.5 cm. The blurry yellow flag in the image foreground is a marker flag on a thermocouple in the chamber that was within the narrow view of the sample, and is inconsequential to the discussed data as it is outside of the field of view of the goniometer camera.*

To begin the experiment, conditions shown in figure 3.3, the cold plate was cooled and held at 120 K.

When the cold plate reached the desired temperature, CO_2 was introduced into the chamber and held at a pressure of 6 mbar. Under these conditions CO_2 ice deposition onto the cold plate took place for 25 minutes until a 0.5 cm sample was formed.

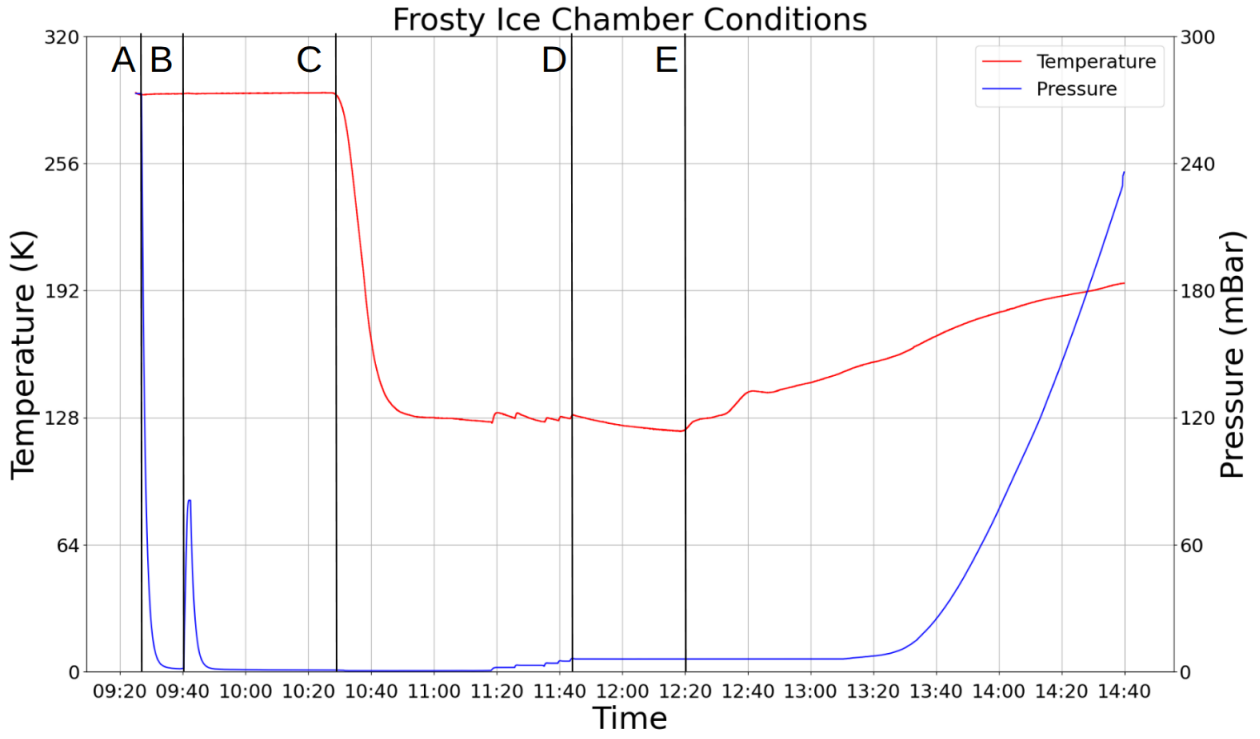

Figure 3.3: *MARVIN chamber [1] conditions throughout the duration of the full frosty ice experiment. A) onset of pump-down to remove atmosphere from the chamber. B) onset of 80 mbar CO_2 chamber purge and pump-down to below 0.5 mbar. C) onset of cold plate cooling to 128 K. D) onset of temperature adjustment to 120 K and introduction of 6 mbar of gaseous CO_2, initiating sample deposition. E) onset of gradual cold plate warming, initiating sample evolution.*

The first goniometer measurement F1 in figure 3.4 was taken at 12:12, at a temperature and pressure of 122.0 K and 6.0 mbar. Following the initial measurement, the cold plate temperature was allowed to steadily rise to 162 K where five more measurements with the goniometer were performed, marked as F2 through F6 in figure 3.4. When the sample plate temperature passed 150 K, CO_2 ice deposited on the liquid nitrogen inlet lines began to sublimate, increasing the chamber pressure to a pressure of 12.0 mbar when the final goniometer measurement was taken. Taking the final measurement at 13:30, with a temperature and pressures of 161.7 K and 12.0 mbar.

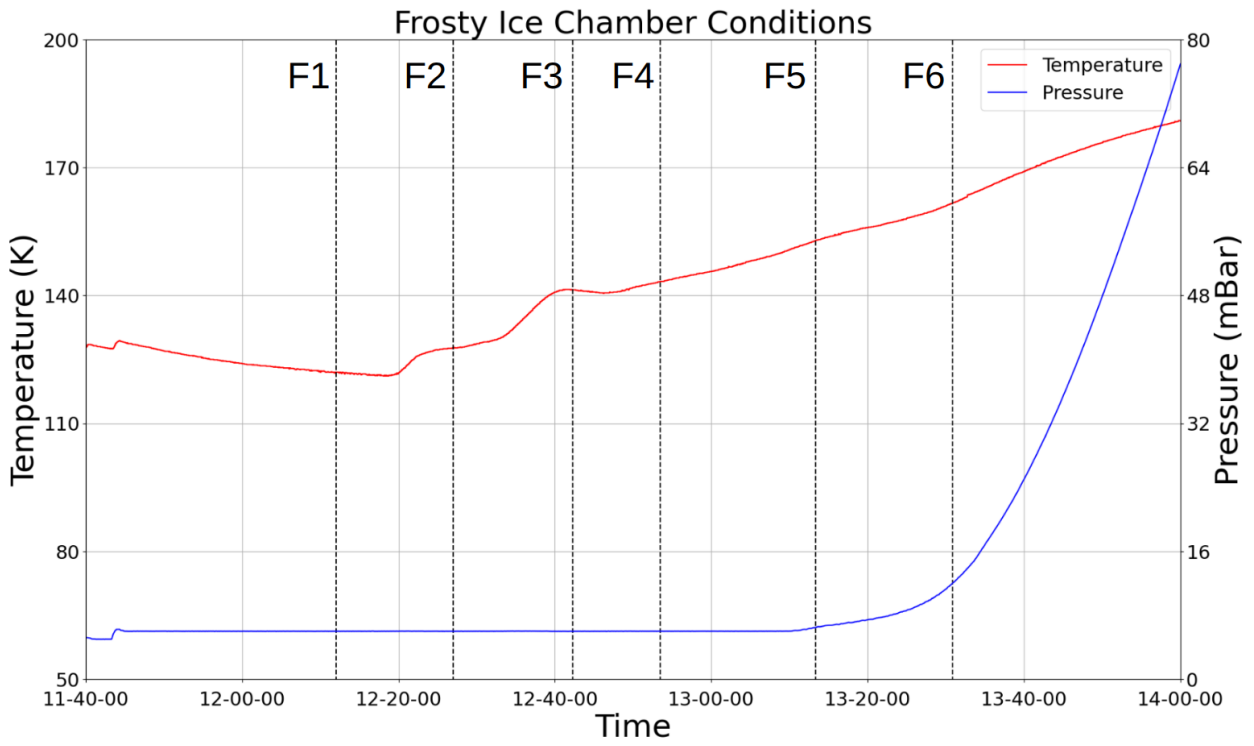

Figure 3.4: *MARVIN chamber [1] conditions during frosty ice data collection using the goniometer. F1) initial measurement of frosty ice at 122 K and 6.0 mbar. F2) measurement immediately following warming onset at 127.7 K and 6.0 mbar. F3) measurement taken at 141.3 K and 6.0 mbar. F4) measurement taken at 143.3 K and 6.0 mbar. F5) measurement taken at 152.8 K and 6.5 mbar at the onset of ice sublimation. F6) measurement taken at 161.7 K and 12.0 mbar after chamber pressure increase due to sublimation.*

The results of the frosty CO_2 ice scattering plane displayed in figure 3.5 mimic those shown in figure 1.10 [2], exhibiting predominantly diffuse scattering behavior with the slow emergence of a back scattering lobe as angle of incidence increases. Scattered peaks in the BRDF, or speckles [2], are observed in the ice at high emission angles above 40° opposite the plane of incidence, visible at incidence angles between 0° and 45°. Smaller speckles are also observed at various emission angles across all angles of incidence.

At the 75° incidence angle, a strong dip in the BRDF is observed between 50° and 80°. This is an effect due to the imperfect Lambertian scattering properties of Spectralon™ [15] at the 75° incidence angle where a strong forward scattering lobe emerges as shown in the raw ADU count data in figure 2.26. After frame division, this creates an artifact in the form of a dip in observed BRDF. This effect is also visible in figure 2.24, mirroring the effect seen in figure 3.5.

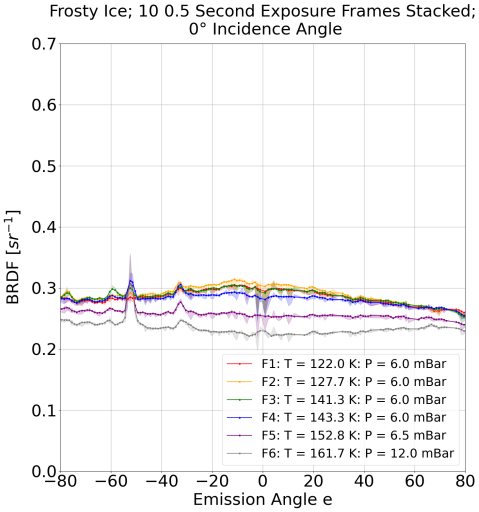
Frosty Ice; 10 0.5 Second Exposure Frames Stacked;
0° Incidence Angle
BRDF [sr^{-1}]
Emission Angle e
F1: T = 122.0 K: P = 6.0 mBar
F2: T = 127.7 K: P = 6.0 mBar
F3: T = 141.3 K: P = 6.0 mBar
F4: T = 143.3 K: P = 6.0 mBar
F5: T = 152.8 K: P = 6.5 mBar
F6: T = 161.7 K: P = 12.0 mBar

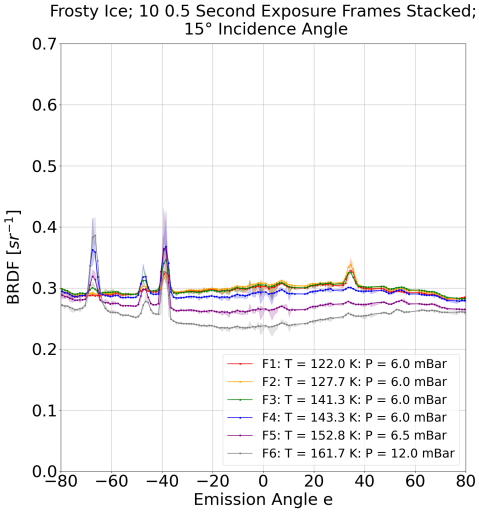
Frosty Ice; 10 0.5 Second Exposure Frames Stacked;
15° Incidence Angle
BRDF [sr^{-1}]
Emission Angle e
F1: T = 122.0 K: P = 6.0 mBar
F2: T = 127.7 K: P = 6.0 mBar
F3: T = 141.3 K: P = 6.0 mBar
F4: T = 143.3 K: P = 6.0 mBar
F5: T = 152.8 K: P = 6.5 mBar
F6: T = 161.7 K: P = 12.0 mBar

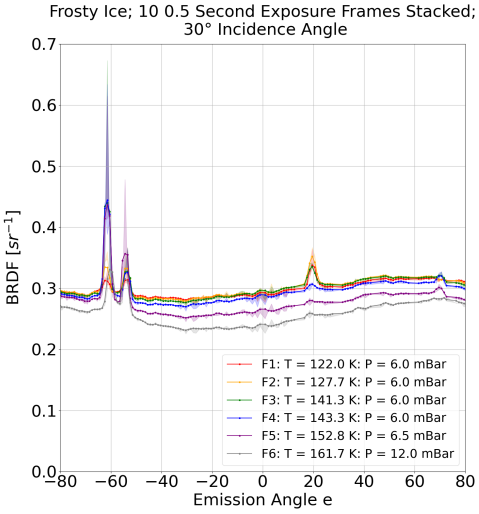
Frosty Ice; 10 0.5 Second Exposure Frames Stacked;
30° Incidence Angle
BRDF [sr^{-1}]
Emission Angle e
F1: T = 122.0 K: P = 6.0 mBar
F2: T = 127.7 K: P = 6.0 mBar
F3: T = 141.3 K: P = 6.0 mBar
F4: T = 143.3 K: P = 6.0 mBar
F5: T = 152.8 K: P = 6.5 mBar
F6: T = 161.7 K: P = 12.0 mBar

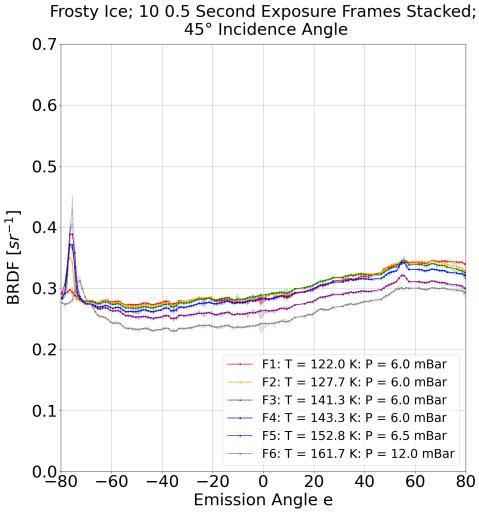
Frosty Ice; 10 0.5 Second Exposure Frames Stacked;
45° Incidence Angle
BRDF [sr^{-1}]
Emission Angle e
F1: T = 122.0 K: P = 6.0 mBar
F2: T = 127.7 K: P = 6.0 mBar
F3: T = 141.3 K: P = 6.0 mBar
F4: T = 143.3 K: P = 6.0 mBar
F5: T = 152.8 K: P = 6.5 mBar
F6: T = 161.7 K: P = 12.0 mBar

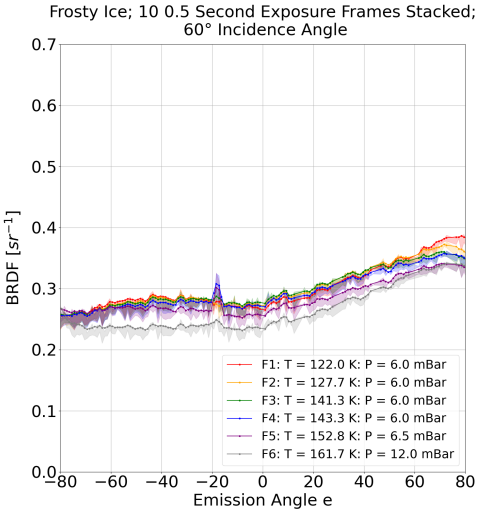
Frosty Ice; 10 0.5 Second Exposure Frames Stacked;
60° Incidence Angle
BRDF [sr^{-1}]
Emission Angle e
F1: T = 122.0 K: P = 6.0 mBar
F2: T = 127.7 K: P = 6.0 mBar
F3: T = 141.3 K: P = 6.0 mBar
F4: T = 143.3 K: P = 6.0 mBar
F5: T = 152.8 K: P = 6.5 mBar
F6: T = 161.7 K: P = 12.0 mBar

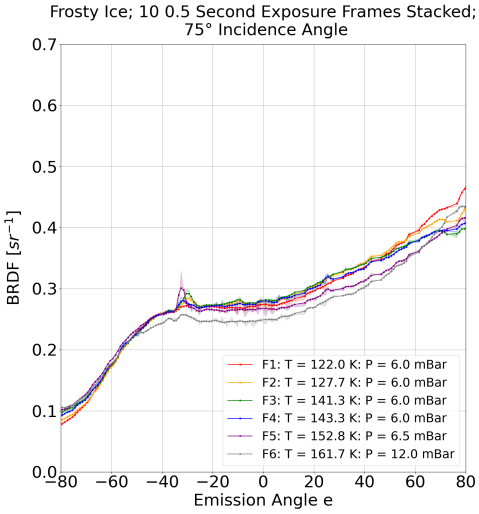
Frosty Ice; 10 0.5 Second Exposure Frames Stacked;
75° Incidence Angle
BRDF [sr^{-1}]
Emission Angle e
F1: T = 122.0 K: P = 6.0 mBar
F2: T = 127.7 K: P = 6.0 mBar
F3: T = 141.3 K: P = 6.0 mBar
F4: T = 143.3 K: P = 6.0 mBar
F5: T = 152.8 K: P = 6.5 mBar
F6: T = 161.7 K: P = 12.0 mBar

Figure 3.5: *Scattering plane data of the F1-F6 goniometer measurements. Each plot represents the laser angles of incidence. F1-F4 show similar results, with F5 and F6 showing continuous drops in overall reflectance. Results are largely diffuse, with peaks in reflectance from 0° to 45° incidence angles, observable at high emission angles opposite the direction of incidence. With small randomly distributed peaks due to light scattering off of crystal facets causing speckles [2]. A large dip in reflectance is observed at emission angles above 50° opposite the incident beam at 75°. This is from forward scattering off the Spectralon™ reference measurement due to imperfect Lambertian scattering properties of the reference sample at high incidence angles.*

Figure 3.6 displays the interpolated half-hemisphere plots of the ice imaged in figure 3.7 during the F4 measurement for each angle of incidence at 143.3 K and 6.0 mbar, before crossing the 150 K temperature boundary. Diffuse scattering properties with the emergence of a back scattering lobe are consistent with the results shown in figure 3.5 with additional speckles shown at azimuths outside the scattering plane. Some halo effects around the speckles are visible due to an artifact of the combined natural neighbor and minimum curvature interpolation techniques implemented [68].

At the 60° and 75° incidence angles, the interpolated plots show a ring of elevated BRDF values at high emission angles across all azimuths, with the exception of the 180° azimuth at emission angles above 50°. These effects are believed to be due to the documented imperfect Lambertian scattering properties of Spectralon™ used for normalization [15, 11, 10, 9, 8, 7].

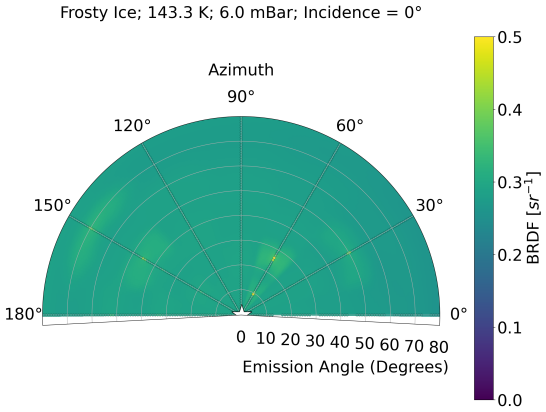
Frosty Ice; 143.3 K; 6.0 mBar; Incidence = 0°
Azimuth
90°
120°
60°
150°
30°
180°
0°
0 10 20 30 40 50 60 70 80
Emission Angle (Degrees)
BRDF [sr^{-1}]
0.0
0.1
0.2
0.3
0.4
0.5

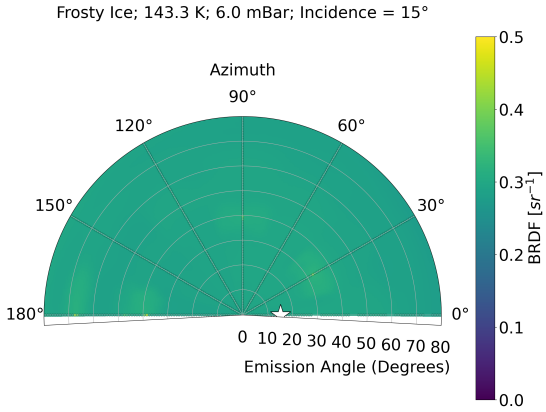
Frosty Ice; 143.3 K; 6.0 mBar; Incidence = 15°
Azimuth
90°
120°
60°
150°
30°
180°
0°
0 10 20 30 40 50 60 70 80
Emission Angle (Degrees)
BRDF [sr^{-1}]
0.0
0.1
0.2
0.3
0.4
0.5

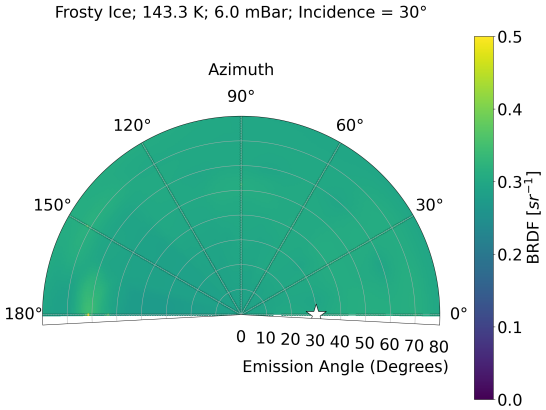
Frosty Ice; 143.3 K; 6.0 mBar; Incidence = 30°
Azimuth
90°
120°
60°
150°
30°
180°
0°
0 10 20 30 40 50 60 70 80
Emission Angle (Degrees)
BRDF [sr^{-1}]
0.0
0.1
0.2
0.3
0.4
0.5

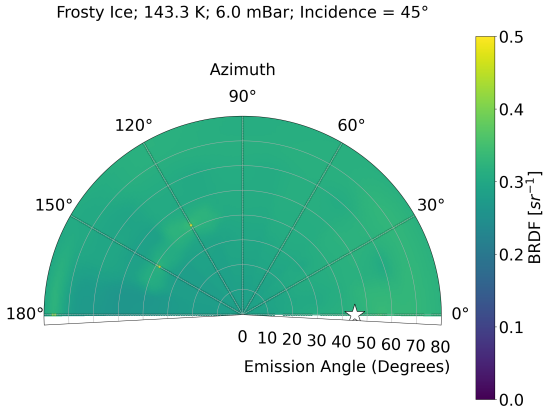
Frosty Ice; 143.3 K; 6.0 mBar; Incidence = 45°
Azimuth
90°
120°
60°
150°
30°
180°
0°
0 10 20 30 40 50 60 70 80
Emission Angle (Degrees)
BRDF [sr^{-1}]
0.0
0.1
0.2
0.3
0.4
0.5

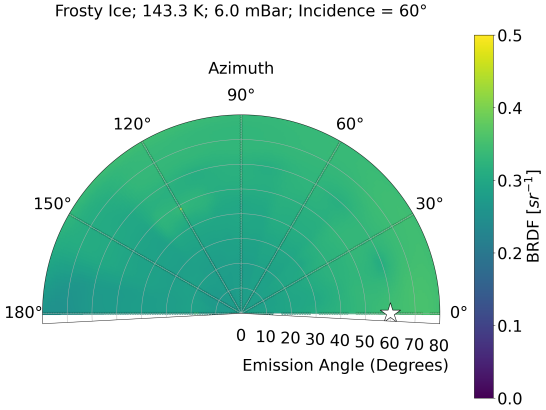
Frosty Ice; 143.3 K; 6.0 mBar; Incidence = 60°
Azimuth
90°
120°
60°
150°
30°
180°
0°
0 10 20 30 40 50 60 70 80
Emission Angle (Degrees)
BRDF [sr^{-1}]
0.0
0.1
0.2
0.3
0.4
0.5

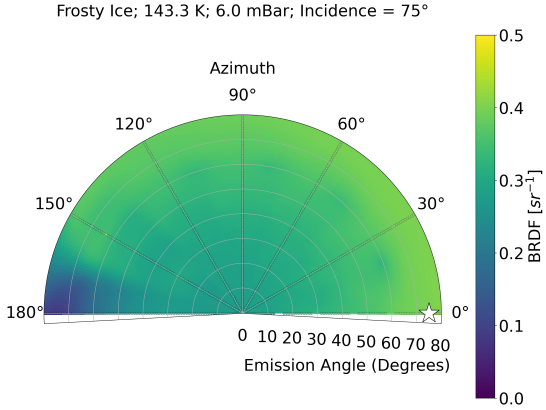
Frosty Ice; 143.3 K; 6.0 mBar; Incidence = 75°
Azimuth
90°
120°
60°
150°
30°
180°
0°
0 10 20 30 40 50 60 70 80
Emission Angle (Degrees)
BRDF [sr^{-1}]
0.0
0.1
0.2
0.3
0.4
0.5

Figure 3.6: *F4 measurement interpolated plot at 143.3 K and 6.0 mbar. Each plot is an interpolated half-hemisphere of reflectance for each angle of incidence. Speckles due to light scattering off crystal facets are observable with some blurring as an artifact of the combined natural neighbor and minimum curvature interpolation implemented [68]. At the 75° incidence angle, the dip in reflectance at emission angles above 50° directly opposite the 75° incident beam, as well as the ring of reflectance at high emission angles, is due to the imperfect Lambertian scattering properties of the Spectralon™ reference. Largely diffuse scattering behavior is observed across all angles of incidence with a ring of reflectance observed at high emission angles when illuminated at 75° incidence.*



Figure 3.7: *Image of the F4 frosty ice morphology taken immediately before goniometer data collection at 143.3 K and 6.0 mbar. The d4 size scale reference suggests the ice is approximately 0.5 cm thick.*

Figure 3.8 displays the interpolated half-hemisphere plots of the ice imaged in figure 3.9 during the F6 measurement at 161.7 K and 12.0 mbar, after crossing the 150 K temperature boundary. The intense ring of BRDF, and the dip in BRDF at 75° directly opposite the incident light source, due to Spectralon™ scattering properties at high incidence angles are still observable here. The ice exhibits diffuse scattering similar to the F4 measurement, but at a reduced overall BRDF value about 0.03 to 0.1 below the F4 measurement at most emission angles and azimuths, with reduced speckle intensity.

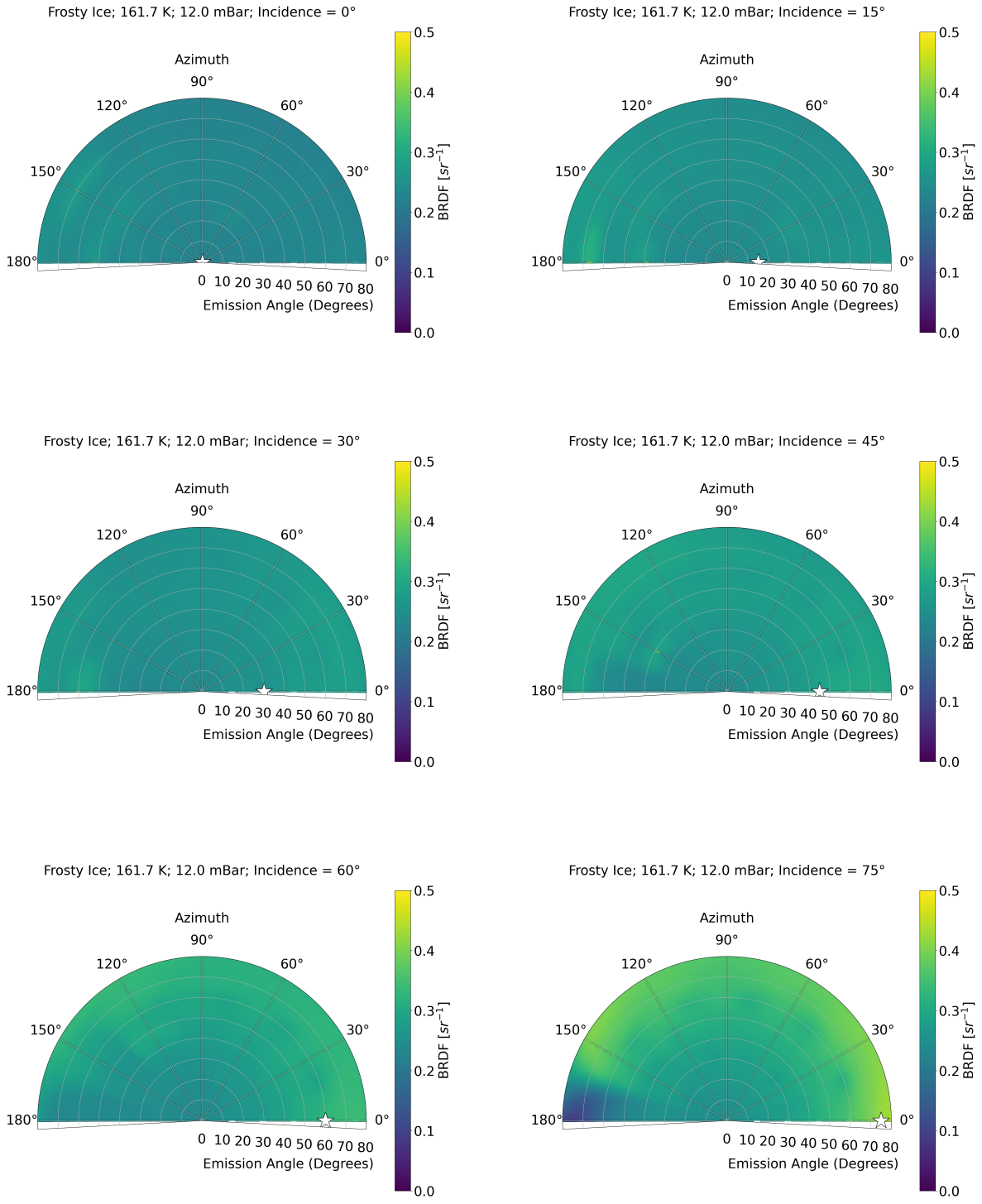

Figure 3.8: *F6 measurement interpolated plot at 161.7 K and 12.0 mbar. The speckles seen in figure 3.6 have faded considerably, suggesting softening in the geometry of crystal facets due to warming and sublimation. At the 75° incidence angle, the dip in reflectance at emission angles above 50° directly opposite the 75° incident beam, as well as the ring of reflectance at high emission angles, is due to the imperfect Lambertian scattering properties of the Spectralon™ reference. Overall diffuse scattering behavior is preserved in the warmed sample, but at lower overall reflectance values.*



Figure 3.9: *Image of the F6 frosty ice morphology taken immediately before goniometer data collection at 167.1 K and 12.0 mbar. The d4 size scale reference suggests the ice is approximately 0.5 cm thick.*

3.2.2 Specular Transparent CO_2 Slab Ice Evolving Into Diffusely Scattering Frosty CO_2 Ice

In this experiment, a slightly modified replication of the experiment outlined in figure 1.9 [2] is presented. The sample of CO_2 slab ice shown in figure 3.10 is grown, examined with the goniometer, and then morphed into a frosty ice sample by dropping the cold plate temperature target and adjusting the atmospheric pressure to that of the experiment in section 3.2.1. The sample is examined during and after this transformation from a translucent slab to a frosty ice sample, demonstrating the rapid data collection capabilities of integrated goniometry.

Typically, this morphology is formed under Martian atmospheric pressure and temperature conditions involving cooling the shroud in the MARVIN chamber to 180 K to recreate a similar radiation environment to that of the Martian surface [2, 1]. When attempting to cool the shroud, the cold radiative environment caused the goniometer lasers to fall outside of their operating temperature range causing the lasers to fail [47]. However, it was found that the same translucent slab ice formed without cooling the shroud at a CO_2

pressure of 100 mbar and a cold plate temperature target of 160 K. This methodology was implemented to grow the initial 0.5 cm sample of translucent slab ice, performing initial goniometry measurements under these conditions.

Following translucent slab ice formation, the ice was morphed into frosty ice by shifting the chamber conditions to those implemented in section 3.2.1, dropping the pressure to 6.0 mbar, and the cold plate temperature to 120 K. During sample evolution, goniometry measurements were performed to monitor sample evolution, performing a first of its kind measurement of multiangular goniometry of an actively evolving sample of Mars-analog CO_2 ice. These measurements leverage the rapid data collection capabilities of integrated goniometry.

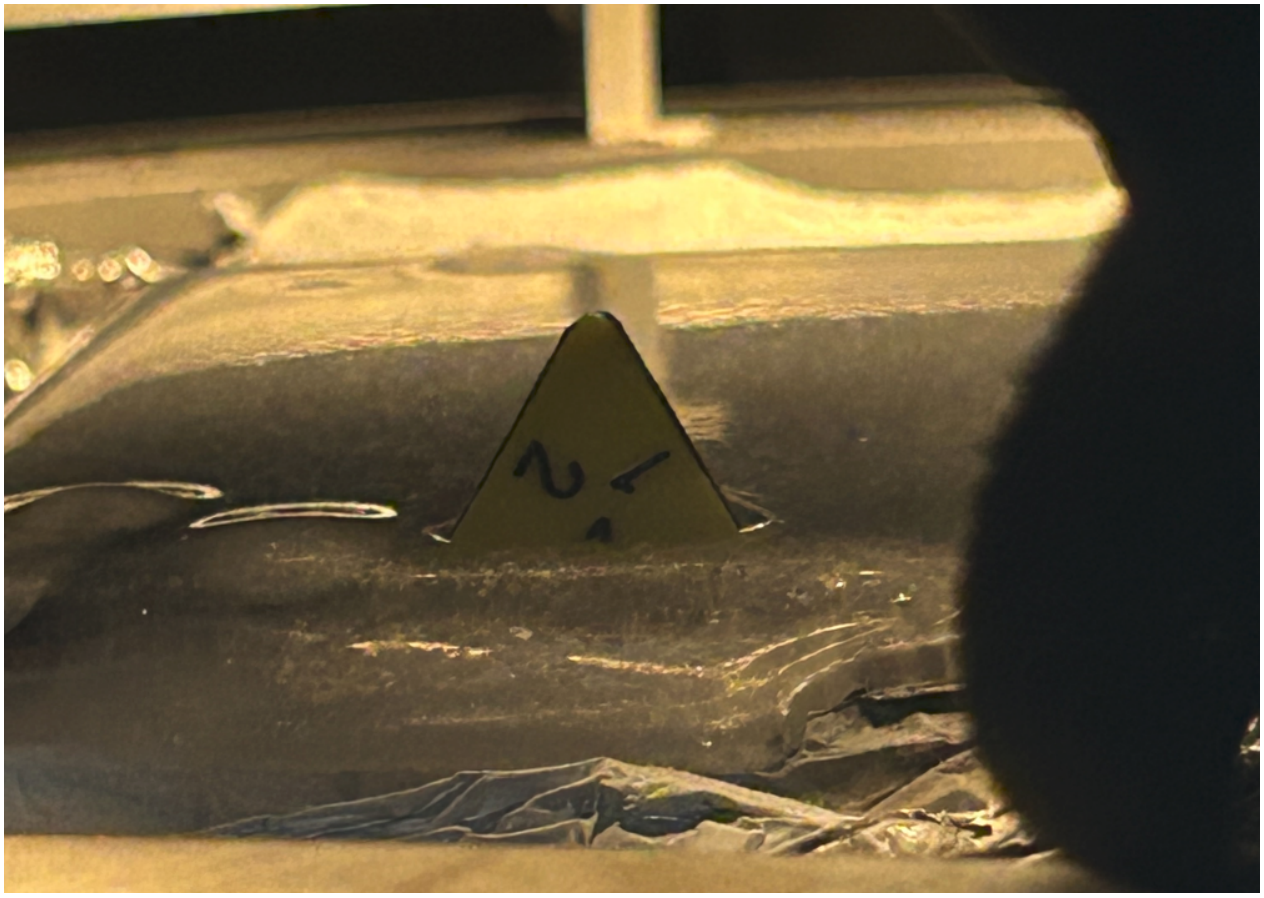

Figure 3.10: *Image of the slab ice showing the smooth, shiny surface structure, grown at 160 K and 100.0 mbar. The d4 die embedded in the ice acts as a reference size scale, where the ice covering the bottom number of the die corresponds to an approximate ice thickness of 0.5 cm.*

The full experimental chamber conditions of the experiment transforming CO_2 slab ice into frosty ice are shown in figure 3.11; the cold plate was cooled to 160 K, followed by introduction of 100 mbar of

CO_2. These conditions initiated translucent slab ice deposition, reaching the desired thickness of 0.5 cm in approximately 35 minutes. Following sample formation, two measurements with the goniometer were performed on the 0.5 cm slab ice under these conditions, shown as S1 and S2 in figure 3.12.

With the S1 and S2 measurements (figure 3.12) performed, the chamber pressure was reduced to 6.0 mbar, and the cold plate temperature was reduced to a target temperature of 120 K. Initiating frost deposition onto the existing translucent slab ice sample. During sample evolution, four more goniometer measurements were performed to examine the evolution of the sample under the new chamber conditions.

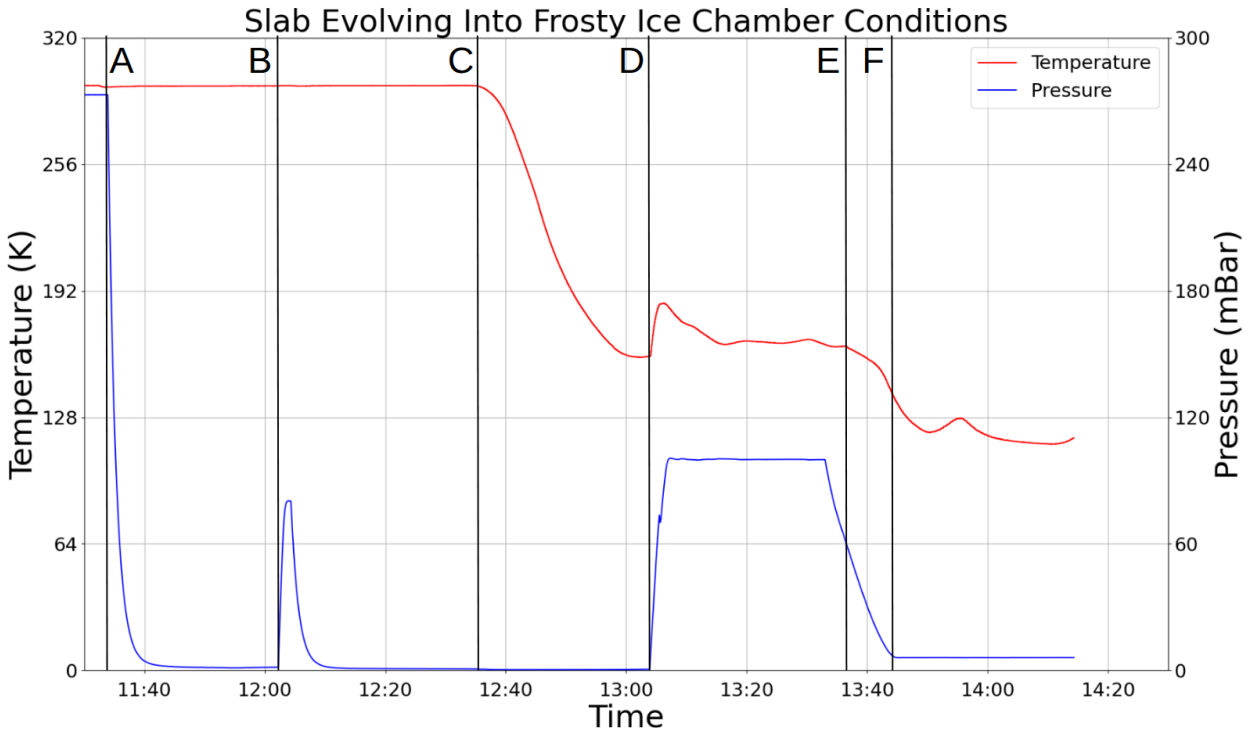

Figure 3.11: *MARVIN chamber [1] conditions throughout the duration of the full slab to frosty ice experiment. A) onset of chamber pump-down from atmosphere. B) onset of chamber purge with 80.0 mbar of CO_2 and pump-down to below 0.5 mbar. C) onset of cold plate cooling to 160 K. D) introduction of 100.0 mbar of CO_2 and the beginning of slab ice deposition. E) onset of cold plate temperature reduction to 120 K. F) pressure reduction to 6.0 mbar for CO_2 frost deposition onto the existing CO_2 slab ice.*

Measurements from the goniometer are shown in figure 3.12; S1 and S2 were performed under nearly identical temperature and pressure conditions. S1 was performed at 167.1 K and 100.0 mbar, while S2 was 167.3 K and 99.9 mbar. To capture the transitional morphology, S3 was taken as the ice cooled down to its target temperature, with a measurement temperature and pressure of 134.9 K and 6.0 mbar. S4, S5, and S6 were taken as frost deposition was ongoing after reaching the target temperature of 120 K, while maintaining the 6 mbar pressure, taken at 120.4 K, 121.6 K, and 127.5 K, respectively, as the cold plate

temperature fluctuated slightly.

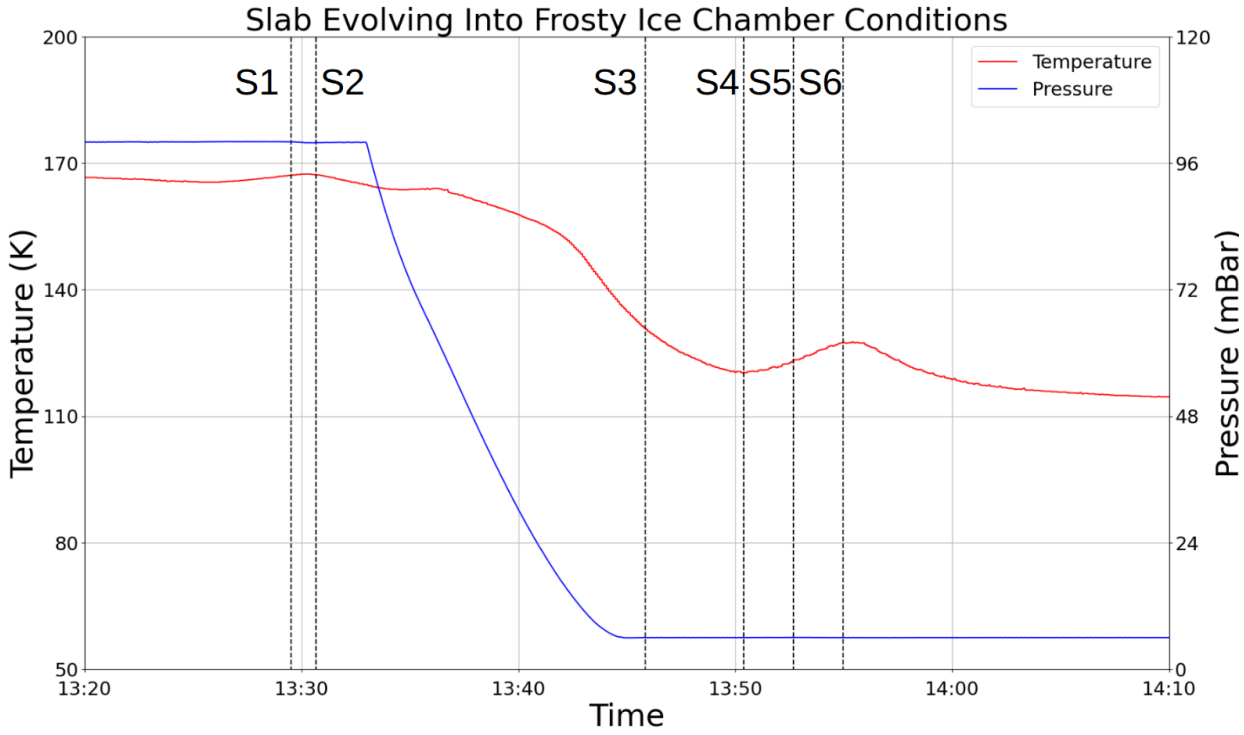

Figure 3.12: *MARVIN chamber [1] conditions during goniometer data collection of the CO_2 slab ice sample evolving into frosty ice. S1) and S2) are measurements of the slab ice under stable conditions of 167.1 K at 100 mbar, and 167.3 K at 99.9 mbar respectively. S3) measurement taken at 134.9 K and 6.0 mbar during active sample cooling to 120 K after pressure reduction. S4) measurement taken at 120.4 K and 6.0 mbar, after frost had deposited onto the sample. S5) and S6) were taken to further observe the slab/frosty composite CO_2 ice, with measurements taken at 121.6 K at 6.0 mbar, and 127.5 K at 6.0 mbar respectively.*

The scattering plane results of the S1-S6 measurements are displayed in figure 3.13. Compared to figure 1.9 from Isen and Smith 2024, the translucent slab ice formed in this experiment exhibited the same clear specular reflections in the S1 and S2 measurements, but at lower peak BRDF values, with peaks becoming more intense at high angles of incidence in agreement with figure 1.9 [2]. These results deviate from the results found in Isen and Smith 2024 [2], the specular reflection from a 45° illumination angle was the weakest of the specular reflections observed. Additionally, the specular peaks deviate from figure 1.9, showing one strong spike in reflected radiation, rather than a triple peak form [2], while maintaining an equivalently broad single peak.

The S3 measurement shows the transitional morphology of the translucent slab ice evolving into the frosty ice. The majority of the specular peaks have either weakened or dissipated completely, while the overall reflectance increased as diffuse scattering emerged. However, the overall reflectance of this more diffuse

form is lower than the frosty ice formed later in the experiment. In the S4, S5, and S6 morphologies, the ice exhibited the same diffuse scattering behavior, with overall reflectance increasing slightly as frost continued to deposit. The overall reflectance values in S4, S5 and S6, are generally lower than in figure 1.9, and lower than in section 3.2.1, suggesting that some radiation is penetrating the frost layer, and dissipating in the slab ice below.

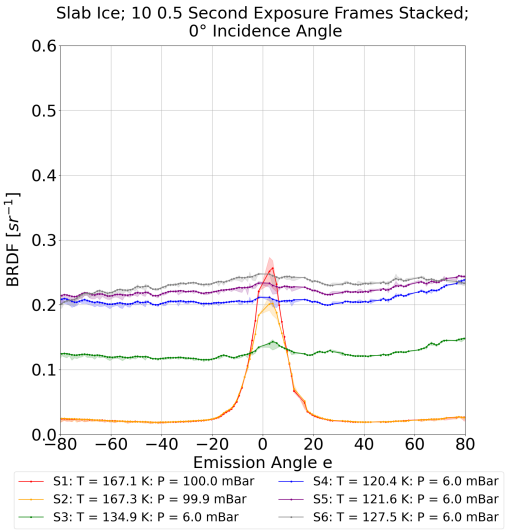
Slab Ice; 10 0.5 Second Exposure Frames Stacked;
0° Incidence Angle
BRDF [sr^{-1}]
Emission Angle e
S1: T = 167.1 K: P = 100.0 mBar
S2: T = 167.3 K: P = 99.9 mBar
S3: T = 134.9 K: P = 6.0 mBar
S4: T = 120.4 K: P = 6.0 mBar
S5: T = 121.6 K: P = 6.0 mBar
S6: T = 127.5 K: P = 6.0 mBar

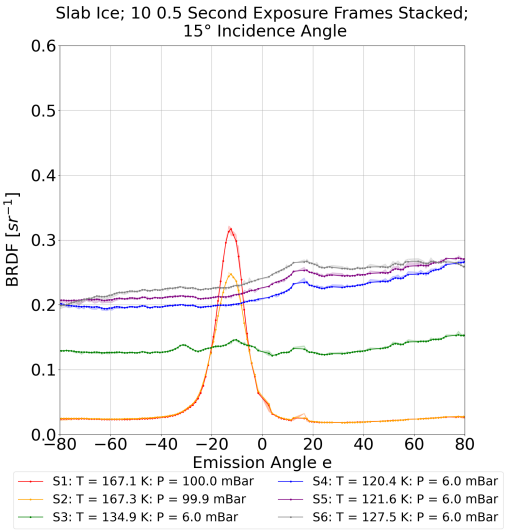
Slab Ice; 10 0.5 Second Exposure Frames Stacked;
15° Incidence Angle
BRDF [sr^{-1}]
Emission Angle e
S1: T = 167.1 K: P = 100.0 mBar
S2: T = 167.3 K: P = 99.9 mBar
S3: T = 134.9 K: P = 6.0 mBar
S4: T = 120.4 K: P = 6.0 mBar
S5: T = 121.6 K: P = 6.0 mBar
S6: T = 127.5 K: P = 6.0 mBar

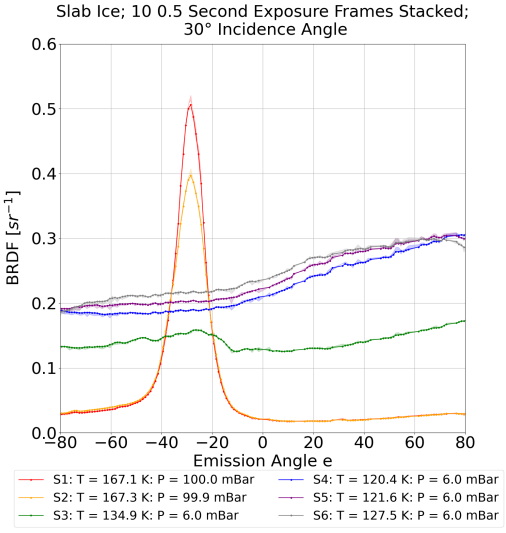
Slab Ice; 10 0.5 Second Exposure Frames Stacked;
30° Incidence Angle
BRDF [sr^{-1}]
Emission Angle e
S1: T = 167.1 K: P = 100.0 mBar
S2: T = 167.3 K: P = 99.9 mBar
S3: T = 134.9 K: P = 6.0 mBar
S4: T = 120.4 K: P = 6.0 mBar
S5: T = 121.6 K: P = 6.0 mBar
S6: T = 127.5 K: P = 6.0 mBar

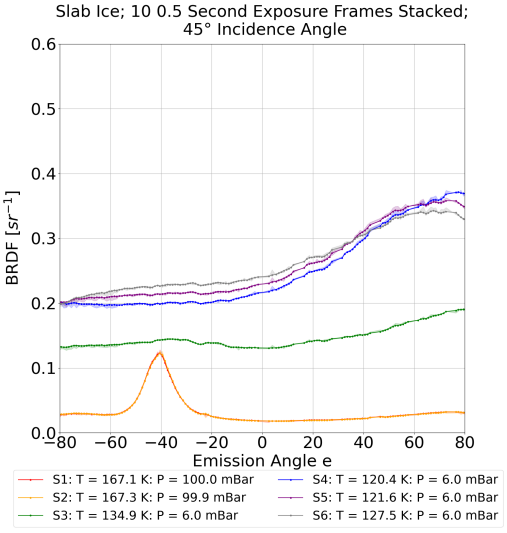
Slab Ice; 10 0.5 Second Exposure Frames Stacked;
45° Incidence Angle
BRDF [sr^{-1}]
Emission Angle e
S1: T = 167.1 K: P = 100.0 mBar
S2: T = 167.3 K: P = 99.9 mBar
S3: T = 134.9 K: P = 6.0 mBar
S4: T = 120.4 K: P = 6.0 mBar
S5: T = 121.6 K: P = 6.0 mBar
S6: T = 127.5 K: P = 6.0 mBar

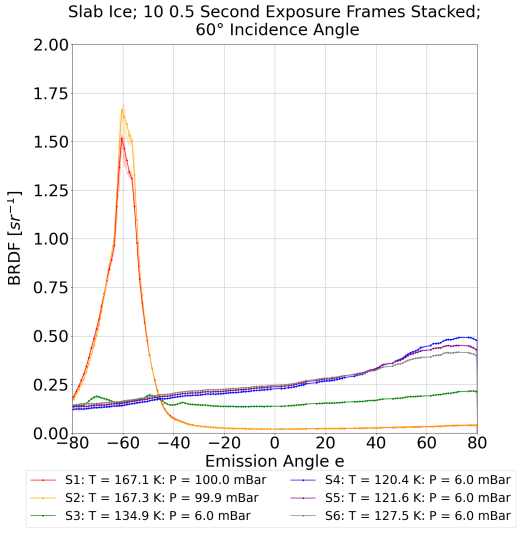
Slab Ice; 10 0.5 Second Exposure Frames Stacked;
60° Incidence Angle
BRDF [sr^{-1}]
Emission Angle e
S1: T = 167.1 K: P = 100.0 mBar
S2: T = 167.3 K: P = 99.9 mBar
S3: T = 134.9 K: P = 6.0 mBar
S4: T = 120.4 K: P = 6.0 mBar
S5: T = 121.6 K: P = 6.0 mBar
S6: T = 127.5 K: P = 6.0 mBar

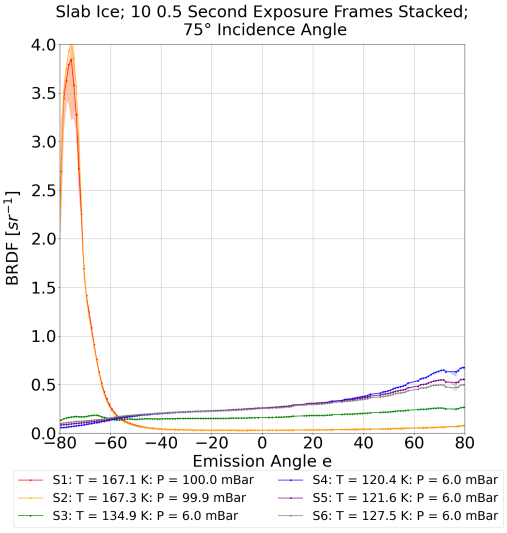
Slab Ice; 10 0.5 Second Exposure Frames Stacked;
75° Incidence Angle
BRDF [sr^{-1}]
Emission Angle e
S1: T = 167.1 K: P = 100.0 mBar
S2: T = 167.3 K: P = 99.9 mBar
S3: T = 134.9 K: P = 6.0 mBar
S4: T = 120.4 K: P = 6.0 mBar
S5: T = 121.6 K: P = 6.0 mBar
S6: T = 127.5 K: P = 6.0 mBar

Figure 3.13: *Scattering plane data of the S1-S6 goniometer measurements. Each plot represents the laser angles of incidence. S1 and S2 show similar results, exhibiting strong, single-peak, specular reflections opposite the incident beam. S3 is the transitional morphology during evolution from CO_2 slab ice to frosty ice. Forward scattering of various BRDF intensities in the S3 morphology are observable at the angles of incidence greater than 0°, with clear emergence of diffuse scattering behavior with BRDF values below the S4 to S6 measurements. S4, S5, and S6 exhibit largely the same results, with diffuse scattering results similar to the section 3.2.1 results, with an overall reduction in BRDF of approximately 0.1.*

Figure 3.14 displays the interpolated half-hemisphere plots of the translucent slab ice imaged in figure 3.15 during the S2 measurement at 167.3 K and 99.9 mbar. In these results, a wide specular lobe is observed at emission angles opposite the incident source in agreement with figure 3.13. Diffuse scattering at azimuths outside the scattering plane are not observed, reinforcing the smooth, specular scattering behavior of the translucent slab ice, in agreement with figure 1.9 from Isen and Smith 2024 [2].

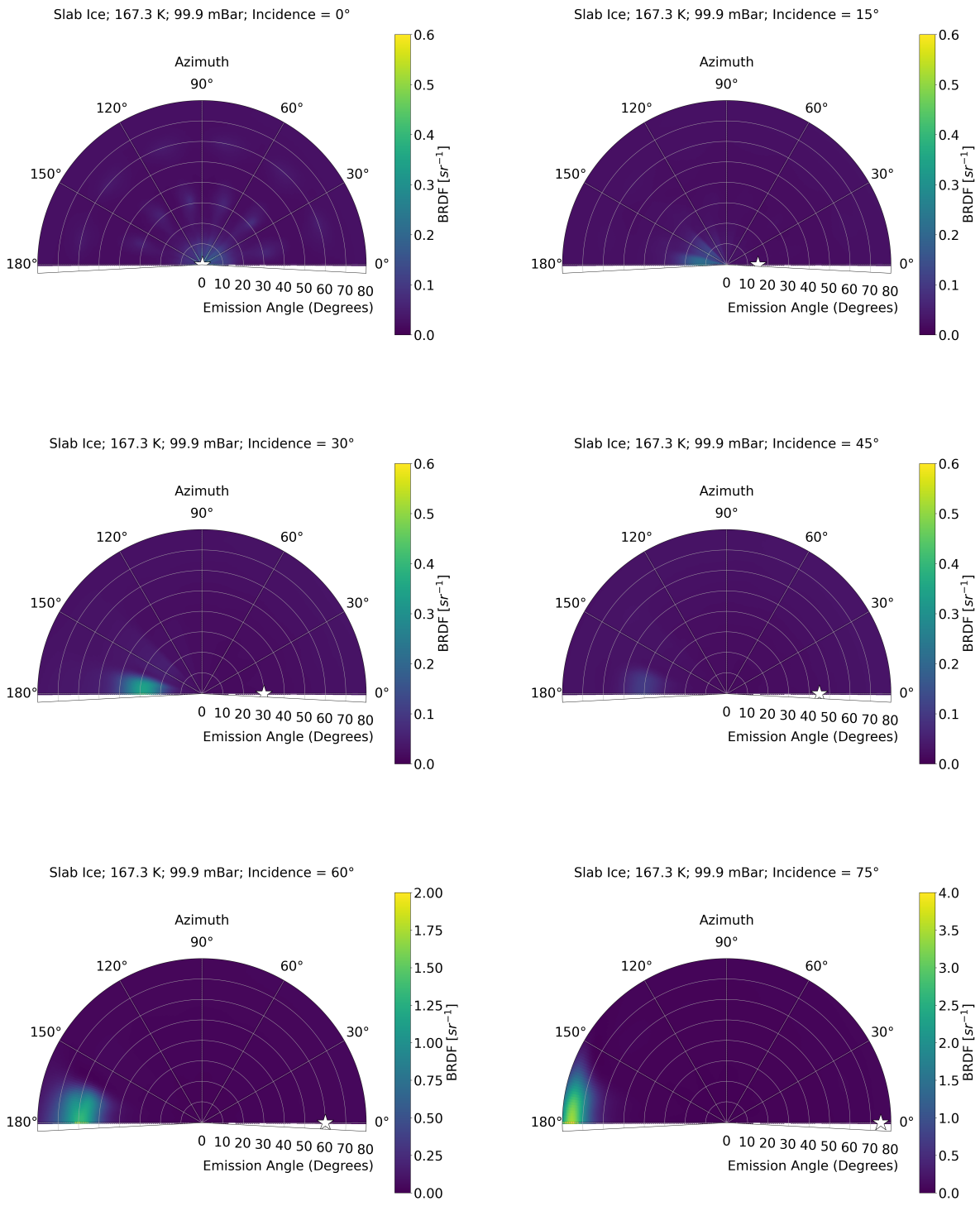

Figure 3.14: *Interpolated plot of the S2 experiment at 167.3 K and 99.9 mbar. Specular reflections are clearly visible with no speckling or diffuse scattering visible outside the scattering plane.*

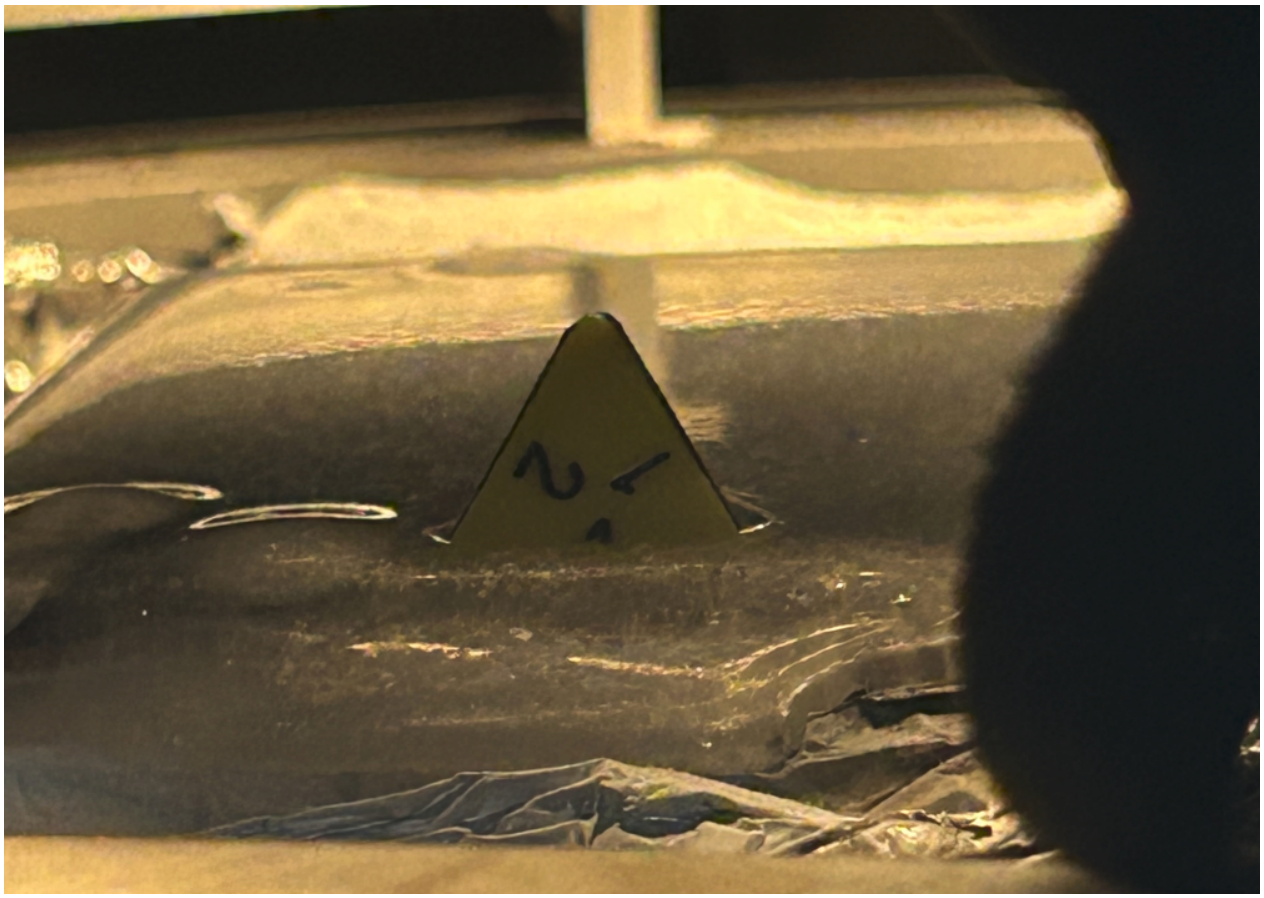

Figure 3.15: *Image of the S2 frosty ice morphology taken immediately before goniometer data collection at 167.3 K and 99.9 mbar. The d4 size scale reference suggests the ice is approximately 0.4 to 0.5 cm thick.*

Figure 3.16 displays the interpolated half-hemisphere plots of the transitional ice morphology imaged in figure 3.15 during the S4 measurement at 134.9 K and 6.0 mbar. Scattering is predominantly diffuse with BRDF in the range of 0.1 to 0.2, with some faint specular lobes at incidence angles between 45° and 75°, with observable widening of the specular lobes in both the emission angle and azimuth angle directions. These results suggest changes to the surface of the ice, implying amorphous crystal structures forming alongside thin depositions of frost on the surface of the ice.

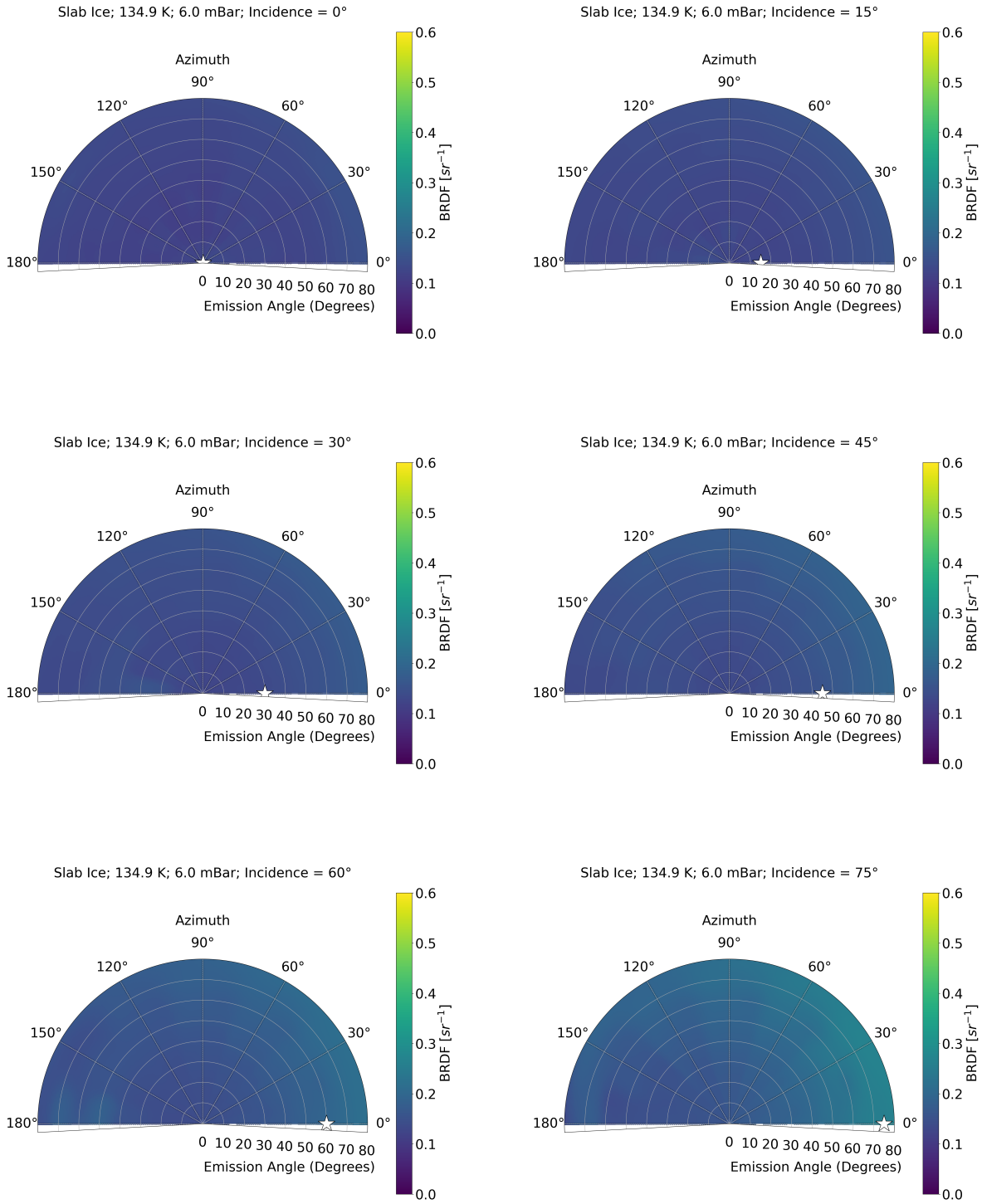

Figure 3.16: *Interpolated plot of the transitional S3 morphology at 134.9 K and 6.0 mbar. Diffuse scattering around 0.13 to 0.14 is observable at 0°, 15°, and 30° incidence angles, with no specular reflections at 0°, and very weak forward scattering observed at 15° and 30°. Diffuse scattering is slightly higher around 0.15 at incidence angles of 45°, 60°, and 75°, with faint, broad, forward scattering lobes reaching 150° azimuths.*



Figure 3.17: *Image of the S3 frosty ice morphology taken immediately before goniometer data collection at 134.9 K and 6.0 mbar. The d4 size scale reference suggests the ice is approximately 0.5 to 0.6 cm thick.*

Figure 3.18 displays the interpolated half-hemisphere plots of the frosty ice grown on top of the translucent slab ice imaged in figure 3.15 during the S5 measurement at 121.6 K and 6.0 mbar. Diffuse scattering behavior mirroring that of figure 1.9 from Isen and Smith 2024 [2], and the results from section 3.2.1 are observed, with a reduction in BRDF of approximately 0.1. Additionally, this frosty morphology lacks the speckles observed in figure 1.9 [2], and section 3.2.1, suggesting that the thin deposition layers of frost have a finer crystal structure that more evenly scatter light. This is supported by comparing the direct images of the ice in figure 3.19 to figures 3.7 and 3.9.

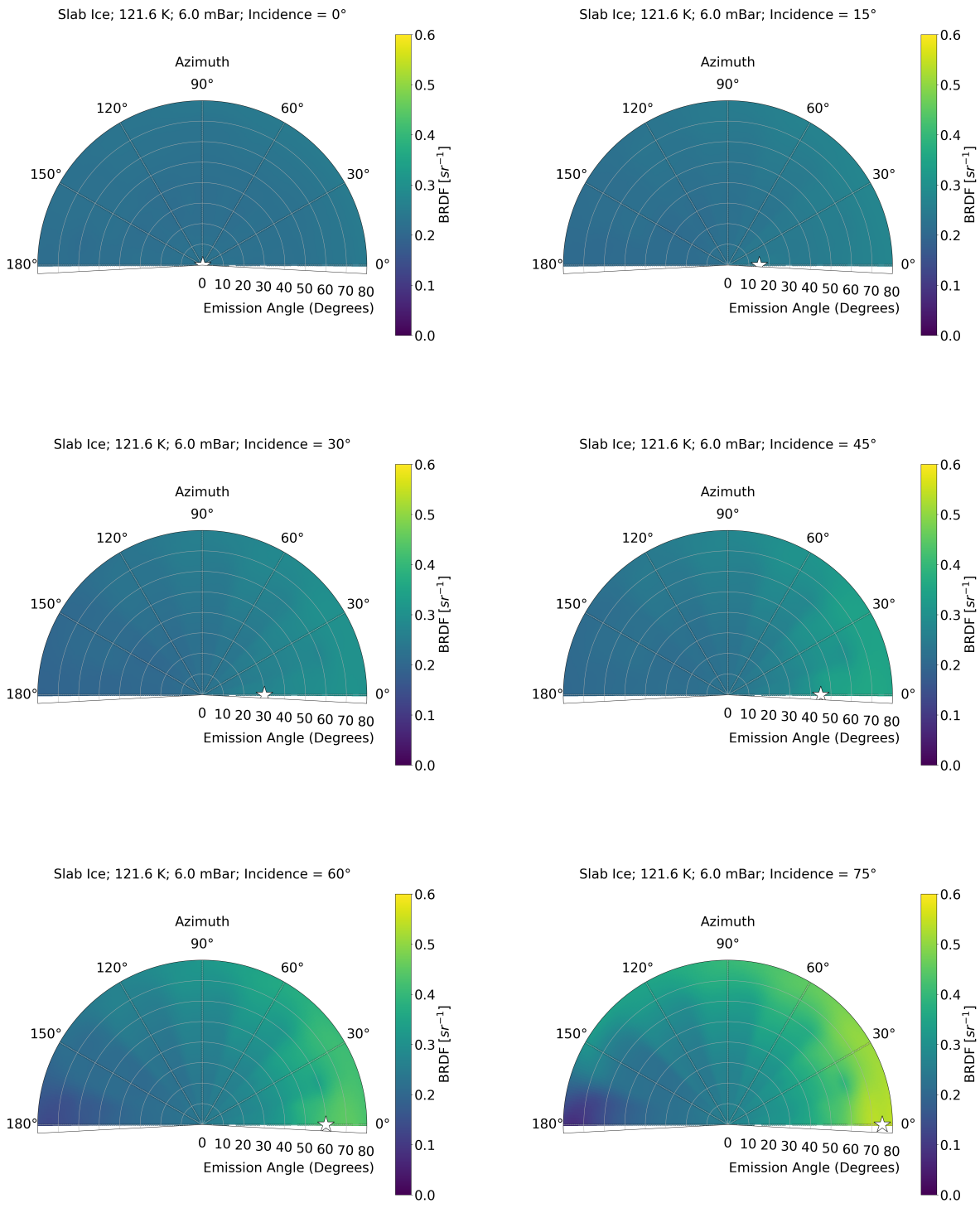

Figure 3.18: *Interpolated plot of the S5 morphology at 121.6 K and 6.0 mbar after CO_2 frost deposition onto the CO_2 slab ice sample. Diffuse scattering similar to the results in section 3.2.1 are observable, with a reduction in BRDF around 0.1, with speckling notably absent.*

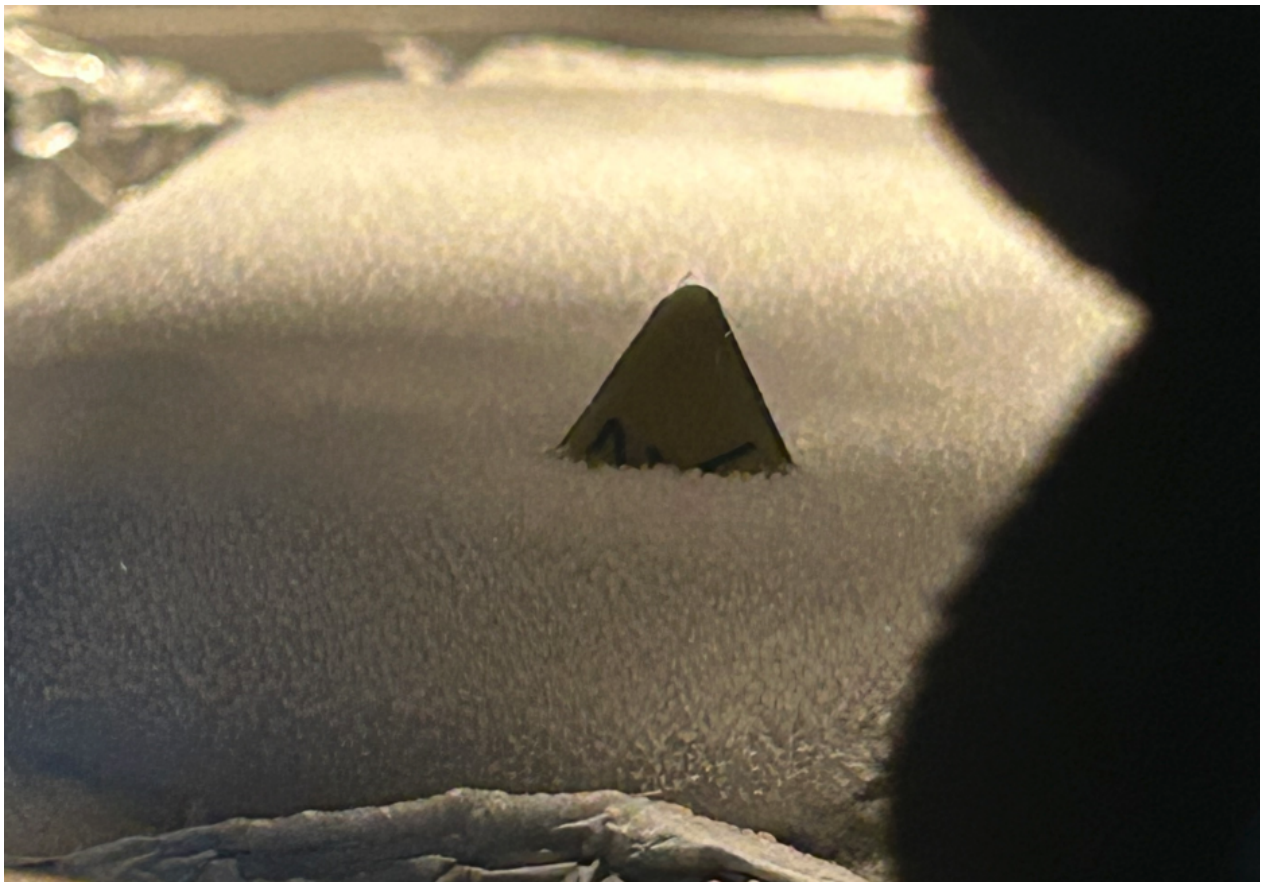

Figure 3.19: *Image of the S5 frosty ice morphology taken immediately before goniometer data collection at 121.6 K and 6.0 mbar. The d4 size scale reference suggests the ice is approximately 0.6 to 0.7 cm thick.*

3.3 Discussion

With the integrated goniometry system performance verified using known reflectance standards, additional performance testing was done by examining ice morphologies previously examined using the goniometer discussed in Isen and Smith 2024 [2]. The results of the diffusely scattering frosty CO_2 ice experiment in section 3.2.1 are consistent with the results presented in the frosty ice experiments outlined in figure 1.10 [2]. Comparing the specular results of the translucent slab CO_2 ice from section 3.2.2 figures 3.13 and 3.14 to figure 1.9, similar specular results are observed, with minor deviation in the specular reflection peak structures. This difference is likely a result of the changes in formation conditions required to accommodate the operating temperature range of the Thorlabs PL203 lasers [47]. This weakness points to potential future work on this integrated goniometry system, indicating the need for preserving laser performance by maintaining suitable operating temperatures for the lasers while cooling the chamber shroud [1]. This could

be done by adding a heater to new laser housings that are insulated from the rest of the device that prevent infrared radiation emitted by the heaters from being visible to the sample. This updated design would enable use of the cooled shroud in the MARVIN chamber [1], allowing for better recreation of Martian conditions.

Results from examining the translucent slab CO_2 ice evolving into frosty CO_2 ice yielded first-of-its-kind results, exhibiting evolution from the specular scattering behavior seen in the interpolated plots in figure 3.14, to the in-between morphology in figure 3.16, to the diffuse scattering seen in figure 3.18. The scattering plane results shown in figure 3.13 further support this by displaying the full ice evolution across the S1-S6 measurements. The data presented leverages the rapid data collection capabilities of integrated goniometry using a verified performance system, enabling the first ever multiangular, half-hemispherical, reflectance data of actively evolving Mars analog CO_2 ice.

Chapter 4

Conclusion

The *bidirectional reflectance distribution function* (BRDF) is a widely adopted model for quantifying the multiangular reflectance properties of illuminated planetary surface materials [2, 1, 3]. Data used to recover the BRDF can easily be obtained by calculating the *reflectance factor* (REFF), the ratio of the reflectance of a reflective surface to that of a diffuse surface under identical illumination conditions, defined by equation 1.20, where BRDF, REFF, and Hapke's *bidirectional reflectance* ($r(i,e,g)$) are closely related to each other through the relations outlined in section 1 [4]. When implementing calibrated reflectance standards like Spectralon™, reflectance quantities can be directly measured, REFF in the case of this thesis, and used to recover the BRDF [11, 9, 10, 8, 7, 15]. Traditional goniometry measurement techniques require the use of a positionable light source and detector to measure individual data points one at a time [4, 41, 42, 43, 44, 8, 10, 2]. Although reliable, this technique is time consuming and requires direct interaction with the source and detector to collect data points. This need for direct interaction makes data collection on samples that are actively evolving, or on samples closed inside controlled environmental systems, extremely challenging. Conditions analogous to these are commonly found inside planetary environment chambers used to simulate the conditions found on the surface of solar system bodies. One such chamber is the MARs Volatile and Ice evolutioN (MARVIN) chamber at York University [1, 2], where evolving CO_2 ice samples are commonly examined under Mars-analog conditions. In Isen and Smith's 2024 publication, goniometry on Mars-analog CO_2 ice was successfully performed using a robotic goniometer built on a traditional goniometer design, in an attempt to address the challenges of traditional goniometry. While the measurements were successfully performed, the device struggled with data collection time and a limited range of data points confined to the principal plane. Here, we discussed, tested, and proved the viability of a novel goniometry technique

dubbed *integrated goniometry*, using a series of strategically placed reflective surfaces imaged by a camera, in conjunction with fixed illumination sources, to collect half-hemispherical REFF data in less than a minute.

Integrated goniometry gets its name from a combination of its ability to collect data over a smooth, continuous surface, its scalability, and its ability to be integrated into experimental systems. Using strategically placed continuous reflectance surfaces imaged by a camera that intercept the hemisphere of reflectance coming off an illuminated surface. The device collects data frames constructed using images from the device camera containing radiative intensity data from the illuminated sample. When frames from a sample of interest are divided by frames from a reference sample of known, near-Lambertian reflective properties, a frame with REFF data embedded in it is produced. When analyzed using a calibrated algorithm, the dedicated python library extracts ready-to-process REFF data from the data frames that is exported to .xls and .csv files. To prove the efficacy of the constructed goniometer when examining diffusely reflecting samples, a Labsphere® Certified Reflectance Standards RSS-08-020 gray scale Spectralon™ kit was used to successfully verify that the goniometer could produce expected REFF data according to the known reflective properties of the samples in the kit [11, 9, 10, 8, 7, 15]. In addition, a mirror was used to verify the specular performance of the device, verifying its ability to measure samples with overwhelmingly specular reflecting properties.

With the goniometer performance verified, the device was installed into the MARVIN chamber [1] and used to examine Mars-analog CO_2 ice. The experiments discussed in section 3, mirroring the experiments in the discussed Isen & Smith 2024 publication [2], further verify the performance of the constructed goniometer, and expand upon the previously published work. In the first experiment, the goniometer was used to examine a sample of CO_2 ice formed by depositing frost onto the MARVIN chamber cold [1] plate at 120 K and under a Mars-analog atmospheric pressure of pure CO_2 at 6 mbar [19, 22, 2]. The sample examined by the integrated goniometry system was observed to produce equivalent BRDF values to the data presented in Isen & Smith 2024, with the addition of examining subtle changes to sample morphology in response to an increase in sample temperature from 120 K to 160 K. In the second experiment, the sample examined was CO_2 ice formed at a temperature target of 160 K and CO_2 pressure of 100 mbar, forming a slab of translucent, shiny, specular reflecting CO_2 ice. This sample was transformed into a frost-dominant ice by dropping the sample temperature to 120 K. These results are largely in agreement with figure 1.9; the ice exhibited specular reflecting behavior in the slab ice morphology, at similar or slightly reduced peak BRDF values with a single specular peak rather than the multi-point peak seen in Isen & Smith 2024 [2]. This deviation

in results is likely the result of the different conditions used to grow the ice as required by the operating temperatures of the sample illumination lasers used in the chamber [47], revealing a limitation in the current design, one that is likely addressable by including a radiatively isolated heating system for the lasers. When the slab ice was formed and examined, the sample was cooled to 120 K and the CO_2 atmospheric pressure was reduced to 6 mbar, where a layer of frost was deposited onto the slab ice sample, and the rapid data collection capabilities of the goniometer were used to examine the evolving transitional morphology of the ice. In this experiment, the multiangular reflective properties of a CO_2 ice sample evolving from a sample with specular reflecting behavior, to a sample with diffuse scattering behavior was examined, expanding upon the BRDF data published in the discussed Isen & Smith 2024 publication [2]. The data presented in this thesis represents true, first-of-its-kind data of actively evolving CO_2 ice under Martian conditions using a performance-verified integrated goniometry system.

Bibliography

[1] I. Smith, J. Isen, R. Karimova, A. Van Brenen, E. McKernan, and D. Ahmadieh, "The mars volatile and ice evolution (marvin) chamber," *Icarus*, vol. 411, p. 115941, 2024.

[2] J. A. Isen and I. B. Smith, "Principal-plane brdf of co2 ice morphologies in controlled mars polar conditions," *Icarus*, vol. 426, p. 116347, 2025.

[3] I. B. Smith, C. Andres, S. Hibbard, S. Nerozzi, R. Aguilar, P. Buhler, B. Cornford, L. Tamppari, and T. N. Titus, "Mars as one system: Insights from the 8th international conference on mars polar science and exploration," *Icarus*, p. 116998, 2026.

[4] B. Hapke, *Theory of reflectance and emittance spectroscopy*. Cambridge university press, 2012.

[5] P. Helfenstein and J. Veverka, "Photometric properties of lunar terrains derived from hapke's equation," *Icarus*, vol. 72, no. 2, pp. 342–357, 1987.

[6] J. B. MARION, "15 - light," in *Physics in the Modern World (Second Edition)* (J. B. MARION, ed.), pp. 399–435, Academic Press, second edition ed., 1981.

[7] J. M. Sanz, C. Extremiana, and J. Saiz, "Comprehensive polarimetric analysis of spectralon white reflectance standard in a wide visible range," *Applied optics*, vol. 52, no. 24, pp. 6051–6062, 2013.

[8] A. Shaw, M. Daly, E. Cloutis, G. Basic, D. Hamilton, K. Tait, B. Hyde, E. Lymer, and K. Balachandran, "Reflectance properties of gray-scale spectralon® as a function of viewing angle, wavelength, and polarization," *International Journal of Remote Sensing*, vol. 37, no. 11, pp. 2510–2523, 2016.

[9] M. P. Levesque and M. Dissanska, "Correction of the calibration measurement by taking into account the spectralon spectro-polarimetric brdf model," in *Reflection, Scattering, and Diffraction from Surfaces VI*, vol. 10750, pp. 60–70, SPIE, 2018.

[10] G. T. Georgiev and J. J. Butler, "Brdf study of gray-scale spectralon," in *Earth Observing Systems XIII*, vol. 7081, pp. 46–54, SPIE, 2008.

[11] A. Bhandari, B. Hamre, O. Frette, L. Zhao, J. J. Stamnes, and M. Kildemo, "Bidirectional reflectance distribution function of spectralon white reflectance standard illuminated by incoherent unpolarized and plane-polarized light," *Applied Optics*, vol. 50, no. 16, pp. 2431–2442, 2011.

[12] S. J. Koppal, *Lambertian Reflectance*, pp. 441–443. Boston, MA: Springer US, 2014.

[13] M. Minnaert, "The reciprocity principle in lunar photometry," *Astrophysical Journal, vol. 93, p. 403-410 (1941).*, vol. 93, pp. 403–410, 1941.

[14] H. Von Helmholtz, *Handbuch der physiologischen Optik*, vol. 9. L. Voss, 1867.

[15] Labsphere, Inc., LABSPHERE, INC. 231 Shaker Street POB 70 North Sutton, NH 03260 US, *Spectralon Diffuse Reflectance Standards*, 2019.

[16] H. Zhang and K. J. Voss, "On hapke photometric model predictions on reflectance of closely packed particulate surfaces," *Icarus*, vol. 215, no. 1, pp. 27–33, 2011.

[17] H. Zheng, H. Zhang, Y. Shkuratov, and D. Britt, "Bi-directional reflectance and raman characterizations of spectralons with varying albedos," *Optics Express*, vol. 33, no. 4, pp. 7942–7961, 2025.

[18] S. Byrne, "The Polar Deposits of Mars," *Annual Review of Earth and Planetary Sciences*, vol. 37, pp. 535–560, May 2009.

[19] I. B. Smith, C. Andres, S. Hibbard, S. Nerozzi, R. Aguilar, P. Buhler, B. Cornford, L. Tamppari, and T. N. Titus, "Mars as one system: Insights from the 8th international conference on mars polar science and exploration," *Icarus*, p. 116998, 2026.

[20] I. B. Smith, A. Spiga, and J. W. Holt, "Aeolian processes as drivers of landform evolution at the south pole of mars," *Geomorphology*, vol. 240, pp. 54–69, 2015. Planetary Geomorphology: Proceedings of the 45th Annual Binghamton Geomorphology Symposium, held 12-14 September 2014 in Knoxville, Tennessee, USA.

[21] T. Appéré, B. Schmitt, Y. Langevin, S. Douté, A. Pommerol, F. Forget, A. Spiga, B. Gondet, and J.-P. Bibring, "Winter and spring evolution of northern seasonal deposits on mars from omega on mars express," *Journal of Geophysical Research: Planets*, vol. 116, no. E5, 2011.

[22] R. Karimova and I. B. Smith, "Deposition of co2 ice under martin polar conditions: Textures, nir reflectance and response to thermal stresses," *Icarus*, p. 116788, 2025.

[23] W. Calvin, P. James, B. Cantor, and E. Dixon, "Interannual and seasonal changes in the north polar ice deposits of mars: Observations from my 29–31 using marci," *Icarus*, vol. 251, pp. 181–190, 2015.

[24] W. Calvin, B. Cantor, and P. James, "Interannual and seasonal changes in the south seasonal polar cap of mars: Observations from my 28-31 using marci," *Icarus*, vol. 292, pp. 144–153, 2017.

[25] I. Smith, N.-J. Schlegel, E. Larour, I. Isola, P. Buhler, N. Putzig, and R. Greve, "Carbon dioxide ice glaciers at the south pole of mars," *Journal of Geophysical Research: Planets*, vol. 127, no. 4, p. e2022JE007193, 2022.

[26] I. B. Smith, J. W. Holt, A. Spiga, A. D. Howard, and G. Parker, "The spiral troughs of mars as cyclic steps," *Journal of Geophysical Research: Planets*, vol. 118, no. 9, pp. 1835–1857, 2013.

[27] I. B. Smith, N. E. Putzig, J. W. Holt, and R. J. Phillips, "An ice age recorded in the polar deposits of mars," *Science*, vol. 352, no. 6289, pp. 1075–1078, 2016.

[28] S. Hess, J. Ryan, J. Tillman, R. Henry, and C. Leovy, "The annual cycle of pressure on mars measured by viking landers 1 and 2," *Geophysical Research Letters*, vol. 7, no. 3, pp. 197–200, 1980.

[29] F. Forget, "The present and past climates of planet mars," in *EPJ web of conferences*, vol. 1, pp. 235–248, EDP Sciences, 2009.

[30] Y. Langevin, J.-P. Bibring, F. Montmessin, F. Forget, M. Vincendon, S. Douté, F. Poulet, and B. Gondet, "Observations of the south seasonal cap of mars during recession in 2004–2006 by the omega visible/near-infrared imaging spectrometer on board mars express," *Journal of Geophysical Research: Planets*, vol. 112, no. E8, 2007.

[31] C. J. Hansen, S. Byrne, W. M. Calvin, S. Diniega, C. M. Dundas, P. O. Hayne, A. S. McEwen, L. E. McKeown, S. Piqueux, G. Portyankina, *et al.*, "A comparison of co2 seasonal activity in mars' northern and southern hemispheres," *Icarus*, vol. 419, p. 115801, 2024.

[32] H. H. Kieffer, T. N. Titus, K. F. Mullins, and P. R. Christensen, "Mars south polar spring and summer behavior observed by tes: Seasonal cap evolution controlled by frost grain size," *Journal of Geophysical Research: Planets*, vol. 105, no. E4, pp. 9653–9699, 2000.

[33] M. C. Malin, J. F. Bell III, W. Calvin, R. T. Clancy, R. M. Haberle, P. B. James, S. W. Lee, P. C. Thomas, and M. A. Caplinger, "Mars color imager (marci) on the mars climate orbiter," *Journal of Geophysical Research: Planets*, vol. 106, no. E8, pp. 17651–17672, 2001.

[34] G. Portyankina, J. Merrison, J. Iversen, Z. Yoldi, C. Hansen, K.-M. Aye, A. Pommerol, and N. Thomas, "Laboratory investigations of the physical state of co2 ice in a simulated martian environment," *Icarus*, vol. 322, pp. 210–220, 2019.

[35] J. Eluszkiewicz, J.-L. Moncet, M. W. Shephard, K. Cady-Pereira, T. Connor, and G. Uymin, "Atmospheric and surface retrievals in the mars polar regions from the thermal emission spectrometer measurements," *Journal of Geophysical Research: Planets*, vol. 113, no. E10, 2008.

[36] A. Colaprete, J. R. Barnes, R. M. Haberle, J. L. Hollingsworth, H. H. Kieffer, and T. N. Titus, "Albedo of the south pole on mars determined by topographic forcing of atmosphere dynamics," *Nature*, vol. 435, no. 7039, pp. 184–188, 2005.

[37] R. Karimova, "Developing an environmental chamber to simulate conditions at the south pole of mars," 2021.

[38] M. S. Modest, Michael F., *Radiative Heat Transfer (4th Edition)*. Elsevier, 2022.

[39] J. Caniou, *Passive Infrared Detection: Theory and Applications*. Springer New York, NY, 1999.

[40] L. Simonot, "Bouguer and lambert's pioneering contributions to goniophotometric reflectance measurements and models: retrospective," *Journal of the Optical Society of America A*, vol. 42, no. 1, pp. 1–8, 2024.

[41] M. Rice, K. Lapo, K. Hoza, E. Cloutis, M. Kraft, S. Mulcahy, D. Applin, and S. Theuer, "Tanager: Design and validation of an automated spectrogoniometer for bidirectional reflectance studies of natural rock surfaces," *Earth and Space Science*, vol. 11, no. 10, p. e2024EA003686, 2024.

[42] E. Foote, D. Paige, M. Shepard, J. Johnson, W. Grundy, S. Biggar, B. Greenhagen, and C. Allen, "The bidirectional reflectance of apollo lunar soils," in *EPSC-DPS Joint Meeting 2011*, 2011.

[43] L. O. Magaña, D. T. Blewett, A. C. Martin, G. Basic, J. Wiker, A. Sniderman, J. Newhook, P. Prem, B. W. Denevi, and H. Sato, "A goniometric system for photometric and polarization measurements of planetary regolith analogs," *Earth and Space Science*, vol. 12, no. 9, p. e2024EA003979, 2025.

[44] C. H. Lee, C. M. Bachmann, P. Seitzer, and H. Cowardin, "Goniometric and polarized imaging spectroscopic lab measurements ofspacecraft materials," in *Advanced Maui Optical and Space Surveillance Technologies (AMOS) Conference*, 2022.

[45] Suzhou ZWO CO., LTD, Moon bay road 6, Suzhou Industrial Park, Jiangsu Province, China, *Planetary Camera ASI662MC/MMProduct Manual*, January 2026. Available at https://i.zwoastro.com/wp-content/uploads/2026/01/6b176cccbe31232e66dcbabb3a781240.pdf.

[46] Prusa Polymers a.s., Partyzanska 188/7A 170 00 Prague 7 Czech Republic, *Technical datasheet Prusament PC Space Grade Black by Prusa Polymers*, September 2025.

[47] Thorlabs Inc., 43 Sparta Ave Newton, New Jersey 07860 United States, *Compact Laser Module with Bare Wires, 520 nm*, March 2024. Available at blob:https://www.thorlabs.com/0b8afcdd-7c0b-4558-b331-66ce8ddd6f30PL203-Spec-Sheet.pdf.

[48] J. Lai, "The principle and design of cmos active pixel sensor," *Highlights in Science, Engineering and Technology*, vol. 32, pp. 143–149, 2023.

[49] N. Faramarzpour, M. J. Deen, and S. Shirani, "An approach to improve the signal-to-noise ratio of active pixel sensor for low-light-level applications," *IEEE Transactions on Electron Devices*, vol. 53, no. 9, pp. 2384–2391, 2006.

[50] A. El Gamal and H. Eltoukhy, "Cmos image sensors," *IEEE Circuits and Devices Magazine*, vol. 21, no. 3, pp. 6–20, 2005.

[51] J. Chen, N. Chen, Z. Wang, R. Dou, J. Liu, N. Wu, L. Liu, P. Feng, and G. Wang, "A review of recent advances in high-dynamic-range cmos image sensors," *Chips*, vol. 4, no. 1, p. 8, 2025.

[52] M. Aceves-Mijares, A. D´iaz-Méndez, J. Pedraza, J. M. Rocha-Pérez, A. Gallardo, E. Gómez, and C. Dom´inguez, "Silicon sensor with high sensibility from 200 to 1100 nm using embedded silicon nano-particles," in *2010 53rd IEEE International Midwest Symposium on Circuits and Systems*, pp. 276–279, IEEE, 2010.

[53] J. S. Lee, R. I. Hornsey, and D. Renshaw, "Analysis of cmos photodiodes. i. quantum efficiency," *IEEE Transactions on electron devices*, vol. 50, no. 5, pp. 1233–1238, 2003.

[54] O. E. Setälä, M. J. Prest, K. D. Stefanov, D. Jordan, M. R. Soman, V. Vähänissi, and H. Savin, "Cmos image sensor for broad spectral range with¿ 90% quantum efficiency," *Small*, vol. 19, no. 47, p. 2304001, 2023.

[55] M. Breier, C. Haas, W. Li, and D. Merhof, "Color filter arrays revisited—evaluation of bayer pattern interpolation for industrial applications," in *2016 IEEE 14th International Conference on Industrial Informatics (INDIN)*, pp. 52–57, IEEE, 2016.

[56] C. C. Koh and S. K. Mitra, "Compression of bayer color filter array data," in *Proceedings 2003 International Conference on Image Processing (Cat. No. 03CH37429)*, vol. 2, pp. II–255, IEEE, 2003.

[57] R. Palum, "Image sampling with the bayer color filter array," in *PICS*, pp. 239–245, 2001.

[58] S. Paris, P. Kornprobst, J. Tumblin, and F. Durand, "Bilateral filtering: Theory and applications," *Foundations and trends in computer graphics and vision*, vol. 4, no. 1, pp. 1–73, 2009.

[59] Z. Deng, L. Chen, X. Wei, and X. Zhang, "Evaluation of average quantum efficiency of industrial digital camera," *Sensors*, vol. 25, no. 3, p. 899, 2025.

[60] A. Tamang, R. Parsons, U. Palanchoke, H. Stiebig, V. Wagner, A. Salleo, and D. Knipp, "Color sensing by optical antennas: Approaching the quantum efficiency limit," *ACS photonics*, vol. 6, no. 8, pp. 2041–2048, 2019.

[61] Y. Rzhanov, "Accurate determination of camera quantum efficiency from a single image," *Journal of Imaging*, vol. 10, no. 7, p. 169, 2024.

[62] S. B. Howell, *Handbook of CCD astronomy*, vol. 2. Cambridge University Press, 2006.

[63] C. R. Harris, K. J. Millman, S. J. van der Walt, R. Gommers, P. Virtanen, D. Cournapeau, E. Wieser, J. Taylor, S. Berg, N. J. Smith, R. Kern, M. Picus, S. Hoyer, M. H. van Kerkwijk, M. Brett, A. Haldane, J. F. del R´io, M. Wiebe, P. Peterson, P. Gérard-Marchant, K. Sheppard, T. Reddy, W. Weckesser, H. Abbasi, C. Gohlke, and T. E. Oliphant, "Array programming with NumPy," *Nature*, vol. 585, pp. 357–362, Sept. 2020.

[64] J. E. Harvey, "Light-scattering characteristics of optical surfaces," in *Stray Light Problems in Optical Systems*, vol. 107, pp. 41–47, SPIE, 1977.

[65] Edmund Optics inc., 101 East Gloucester Pike, Barrington, NJ, 08007-1380 USA, *TECHSPEC 15.0mm Dia. x 45.0mm FL, Uncoated, Plano-Convex Lens*, Feburary 2026. Available at blob:https://www.edmundoptics.ca/p/150mm-dia-x-450mm-fl-uncoated-plano-convex-lens/10351/.

[66] Newport Corporation, *1830-C Optical Power Meter*, 1994.

[67] Newport Corporation, *818 Series Photodiode Datasheet*, July 2025.

[68] P. Virtanen, R. Gommers, T. E. Oliphant, M. Haberland, T. Reddy, D. Cournapeau, E. Burovski, P. Peterson, W. Weckesser, J. Bright, S. J. van der Walt, M. Brett, J. Wilson, K. J. Millman, N. Mayorov, A. R. J. Nelson, E. Jones, R. Kern, E. Larson, C. J. Carey, İ. Polat, Y. Feng, E. W. Moore, J. VanderPlas, D. Laxalde, J. Perktold, R. Cimrman, I. Henriksen, E. A. Quintero, C. R. Harris, A. M. Archibald, A. H. Ribeiro, F. Pedregosa, P. van Mulbregt, and SciPy 1.0 Contributors, "SciPy 1.0: Fundamental Algorithms for Scientific Computing in Python," *Nature Methods*, vol. 17, pp. 261–272, 2020.

[69] M. Alarcon, J. Licandro, M. Serra-Ricart, E. Joven, V. Gaitan, and R. Sousa, "Scientific cmos sensors in astronomy: Qhy600 and qhy411," *Monthly Notices of the Royal Astronomical Society (MNRAS)*, 02 2023.

[70] C. Layden, J. Juneau, G. Pettersson, N. Lourie, B. Schneider, B. LaMarr, F. Elio Angile, F. Farag, M. Luo, Z. Z. Ong, *et al.*, "Characterization of the teledyne cosmos camera: a large format cmos image sensor for astronomy," *Journal of Astronomical Telescopes, Instruments, and Systems*, vol. 11, no. 2, pp. 026003–026003, 2025.

[71] Marktech, 3 Northway Lane North, Latham, NY 12110, USA, *MTE5270N Datasheet*, September 2024.

[72] W. McKinney, "Data structures for statistical computing in python," in *Proceedings of the 9th Python in Science Conference* (S. van der Walt and J. Millman, eds.), pp. 51 – 56, 2010.